Molecular and Electronic Structures and Charge-Transport Properties of Triphenylamine-Related Materials for Organic Light-Emitting Diodes (OLEDs)

Tomonori Yamada

2011

Contents

Chapter 1

General Introduction

1.1. Backgrounds 1

1.2. Outline of This Thesis 5

References 8

Chapter 2

A Combined Experimental and Theoretical Study of the Amorphous Structure of *N,N'*-diphenyl-*N,N'*-di(*m*-tolyl)benzidine (TPD) Using Solid-State ^{15}N NMR and DFT Calculations

2.1. Introduction 13

2.2. Experimental and Computational Section 15

2.2.1. Samples 15

2.2.2. Solid-State ^{15}N NMR Experiments 16

2.2.3. Computations 17

2.3. Results and Discussion 19

2.3.1. DFT-Optimized Structures 19

2.3.2. Solid-State NMR Results for Amorphous TPD 20

2.3.3. Molecular Structure of TPD in Amorphous State 23

2.3.4. Comparison with XRD Data 27

2.3.5. Planarity Effects on HOMO 28

2.3.6. Planarity Effects on Intermolecular Distance 30

2.4. Conclusion 32

References 33

Chapter 3

Conformational Dependence of Diamagnetic and Paramagnetic ^{15}N NMR Shieldings and Charge-Transport Property of TPD

3.1. Introduction 37

3.2. Computational Section 40

3.3. Results and Discussion 42

3.3.1. Torsion Angle α Dependence of ^{15}N NMR Shielding 42

3.3.2. NCS Analysis for the Torsion Angle α Dependence of the Paramagnetic NMR Deshielding 44

3.3.3. Origins of the Torsion Angle α Dependence of the Paramagnetic NMR Deshielding 49

3.3.4. Torsion Angle β Dependence of ^{15}N NMR Shielding 54

3.3.5. NCS Analysis and Origins of the Torsion Angle β Dependence of the Paramagnetic NMR Deshielding 56

3.3.6. Conformational Dependence of HOMO and LUMO 62

3.4. Conclusion 68

References 68

Chapter 4

Solid-State ^{15}N NMR Study of TPD in the Neutral and Charged States

4.1. Introduction 71

4.2. Experimental and Computational Section 73

4.2.1. Samples 73

4.2.2. ESR Experiments 73

4.2.3. Solid-State ^{15}N NMR Experiments 74

4.2.4. Computations 75

4.3. Results and Discussion 75

4.3.1. ESR Results 75

4.3.2. Solid-State NMR and Computational Results 77

4.4. Conclusion 83

References 84

Chapter 5

Percolation Paths for Charge Transports in TPD Studied by Quantum Chemical Calculations

5.1. Introduction 87

5.2. Computational Section 91

5.3. Results and Discussion 92

5.3.1. Reorganization Energies 92

5.3.2. Frontier Orbitals 92

5.3.3. Molecular Pairs in TPD Crystals 94

5.3.4. *"Hole"* Transports in Orthorhombic TPD 98

5.3.5. *"Electron"* Transports in Orthorhombic TPD 106

5.3.6. *"Hole"* Transports in Monoclinic TPD 107

5.3.7. *"Electron"* Transports in Monoclinic TPD 115

5.4. Conclusion 117

References 117

Chapter 6

Revealing Bipolar Charge-Transport Property of 4,4'-*N,N'*-dicarbazolylbiphenyl (CBP) by Quantum Chemical Calculations

6.1. Introduction 121

6.2. Computational Section 123

6.3. Results and Discussion 124

6.3.1. Molecular Structures and Reorganization Energies 124

6.3.2. Frontier Orbitals 128

6.3.3. Molecular Pairs 130

6.3.4. Hole Transfer Integrals 133

6.3.5. Electron Transfer Integrals 137

6.3.6. Rate Constants and Paths for Charge Transfer 140

6.4. Conclusion 143

References 143

Summary 147

List of Publications 153

Acknowledgements 155

Chapter 1

General Introduction

1.1. Backgrounds

Organic light-emitting diodes (OLEDs) are recognized as potential technologies for flat and flexible displays and lighting sources [1-11] since the first fabrication by Tang et al. in 1987 [1]. In the study, organic amorphous thin films of a hole-transport amine compound, 1,1-bis[(di-4-tolylamino)phenyl]cyclohexane (TAPC), and a bifunctional electron-transport and light-emitting material, tris(8-hydoroxyquinoline) aluminuim(III) (Alq_3) (see Fig. 1.1), were layered, leading to the brightness over 1000 cd/m^2 with the drive voltage below 10 V [1]. This device configuration was followed by the three-layer structure, consisting of a hole-transport, a light-emitting, and an electron-transport layers, proposed by Adachi et al. in 1988 [2]. In these studies, the adoption of the multilayered amorphous thin films with the total thickness less than 100 nm was the essential factor for the low-voltage-driven and pinhole-free luminescence.

In OLEDs, holes and electrons are conveyed to the light-emitting layer via the amorphous charge-transport layers recombine to produce exitons, leading to photon emissions. Therefore, charge-transport phenomena are of importance to understand and to improve the device characteristics [12-19]. However, understandings of charge transports in amorphous organic materials are limited. One of the reasons is that amorphous structures were hardly clarified due to the difficulty of the analyses, although they were considered to closely relate to the charge-transport properties. Even the crystal structures of OLED materials were not clarified for a long time. For example, for the Alq_3 crystal, three polymorphs, α-, β-, and γ-Alq_3, were found by X-ray diffraction (XRD) analyses in 2000 by Brinkmann et al. [20]. There are two isomeric states for Alq_3, facial and meridional isomers. Brinkmann et al. reported that α- and

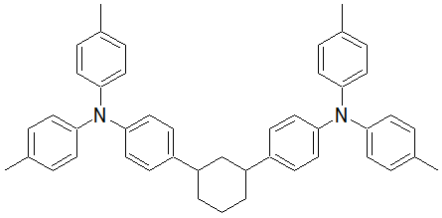

TAPC

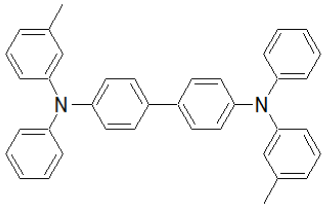

TPD

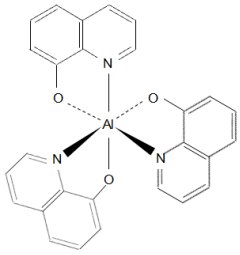

facial

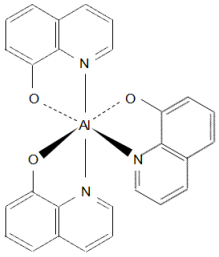

meridional

Alq_3

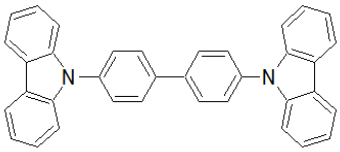

CBP

Fig. 1.1. Chemical structures of 1,1-bis[(di-4-tolylamino)phenyl]cyclohexane (TAPC), facial and meridional isomers of tris(8-hydoroxyquinoline) aluminuim(III) (Alq_3), *N*,*N*'-diphenyl-*N*,*N*'-di(*m*-tolyl)benzidine (TPD), and 4,4'-*N*,*N*'-dicarbazolylbiphenyl (CBP).

β-Alq_3 were composed of meridional isomers and γ-Alq_3 was composed of orientationally disordered meridional isomers. However, the isomeric state of γ-Alq_3 was found to be facial later [21-23], suggesting the difficulty of the analysis. The disorder in the aggregated structure is favorable for the OLED application because it prohibits the crystallization and stabilizes the amorphous states. However, the feature conversely makes the structural analyses difficult. In addition, nitrogen and oxygen atoms are sometimes difficult to be distinguished by XRD methods, although these atoms are important to recognize the facial and meridional isomers of Alq_3. This is because the atomic scattering factors for X-ray are similar to each other for nitrogen and oxygen atoms, due to the low and similar electron densities of the atoms [24]. Another example is for a well-known hole-transport material, *N,N'*-diphenyl-*N,N'*-di(*m*-tolyl) benzidine (TPD) [2,5,6,25-33]. Two kinds of crystalline polymorphs, orthorhombic and monoclinic, were reported for TPD from a comparable XRD profile obtained by several groups [30,32,33]. The reported polymorphs also have structural disorders and difficult to be analyzed in detail. These studies for Alq_3 and TPD show that the molecular structures of OLED materials are difficult to be analyzed even for the crystalline states, due to the structural disorders in the crystals and relatively low selectively of XRD methods for light elements. The XRD methods are hardly valid for disordered amorphous states. Recently, it was shown that solid-state NMR is a powerful tool to investigate disordered materials, because it can provide comparable resolutions for disordered and crystalline states [34-37]. For example, conformation of atactic poly(acrylonitrile) (PAN) was quantified by two-dimensional double-quantum solid-state NMR method [36], although the crystals are highly disordered. When the NMR spectra strongly depend on the conformation as in the case of PAN, it is possible to analyze the conformation precisely and quantitatively. The applications of solid-state NMR techniques for OLED materials are expected to clarify the amorphous

structures.

Another reason for the insufficient understanding of charge-transport phenomena in organic materials is that most studies focused only on intramolecular parameters as described below. However, in organic materials including amorphous materials, charges are transferred through the intermolecular orbital overlaps by hopping mechanism [38-41]. Therefore, the charge transports cannot be fully understood by only the intramolecular parameters. The rate constant, k_{CT}, for the intermolecular hopping charge-transfer processes in Eqs. 1.1 and 1.2 are given by Eq. 1.3, according to Marcus theory [38,39].

$$M_A + M_B^+ \rightarrow M_A^+ + M_B \quad (1.1)$$

$$M_A + M_B^- \rightarrow M_A^- + M_B \quad (1.2)$$

$$k_{CT} = \frac{4\pi^2}{h} H_{AB}^2 \frac{1}{\sqrt{4\pi\lambda k_B T}} \exp\left[-\frac{(\Delta G_{if} + \lambda)^2}{4\lambda k_B T} \right] \quad (1.3)$$

Here, H_{AB} is the charge transfer integral, which expresses the intermolecular orbital overlaps, λ is the reorganization energy, and ΔG_{if} is the free energy difference between the initial and final states. The T, h and k_B are the temperature, Planck and Boltzmann constants, respectively. When the molecules M_A and M_B in Eqs. 1.1 and 1.2 are the same, ΔG_{if} is equal to 0. Then, Eq. 1.3 reduces to Eq. 1.4.

$$k_{CT} = \frac{4\pi^2}{h} H_{AB}^2 \frac{1}{\sqrt{4\pi\lambda k_B T}} \exp\left(-\frac{\lambda}{4 k_B T} \right) \quad (1.4)$$

According to Eq. 1.4, the charge-transfer rate constant is a function of reorganization energy and charge transfer integral, under a certain temperature. Up until now, reorganization energies were eagerly investigated by quantum chemical calculations [14,15,18,19]. For example, small reorganization energies for hole transfer in triarylamine compounds, including TPD, are recognized as essential origins for good hole mobilities [18]. However, there are some cases that the charge-transport properties could not be explained only by the reorganization energies [19]. It should be noted that the charge transfer integral is also a key parameter to quantify the charge-transfer rate constant, although the investigations were hardly reported. This owes not only to the lack of intermolecular structural parameters, which is necessary for the calculations of charge transfer integrals, but also the uncertainty of the investigating method [19]. When a relevant two molecular system is geometrically symmetric, that is, the HOMO (or LUMO) energy of each molecule is comparable with each other, the hole (or electron) transfer integral simply corresponds to the stabilization energy of HOMO (or LUMO), i.e. the half of the energy difference between HOMO and HOMO-1 (or LUMO and LUMO+1) in the two molecular system [42-47]. However, this picture cannot be adopted when the two molecular system is geometrically asymmetric, and the HOMO (or LUMO) energy of each molecule is no longer comparable with each other. This is the most cases for pairs of two molecules in the condensed state. The robust approach is eagerly desired to quantify the charge-transfer rate constants and to understand the charge-transport properties in the condensed state.

1.2. Outline of This Thesis

The aim of this thesis is to show the molecular and electronic structures of organic charge-transport materials to comprehend the origins of charge-transport properties. The contents of this thesis are as follows:

In Chapter 2, the amorphous structure of TPD is investigated by solid-state ^{15}N NMR and density functional theory (DFT) calculations. From NMR experiments, we can observe the magnetic shielding around the nuclei under the applied magnetic field. Depending on the anisotropy of the shielding, broad spectra can be obtained by chemical shift anisotropy (CSA) measurements. In this Chapter, the ^{15}N CSA spectrum is experimentally obtained for amorphous TPD by the solid-state NMR measurement. DFT calculations are also performed to find that the ^{15}N CSA of TPD strongly depends on the molecular structure. By using the structural dependences of the ^{15}N CSA and the experimental CSA spectrum for amorphous TPD, the molecular structure of amorphous TPD is investigated. Especially, the conformation and planarity around the nitrogen atoms are analyzed in detail, which are crucial to determine the structure of TPD molecules. Representing the amorphous structure of TPD, it is shown that the combined use of solid-state NMR experiments and quantum chemical calculations is useful to analyze the amorphous structure.

In Chapter 3, the conformational dependence of the ^{15}N CSA of TPD, obtained in Chapter 2, is analyzed in detail to understand the origin of the conformational dependence and the relationship between the conformation and the charge-transport property. The origins of the conformational dependence of ^{15}N CSA are investigated, dividing the NMR shielding into the diamagnetic and paramagnetic terms. The former is described by the spherical electron density in the ground state. The latter is expressed by the electron circulations between the ground and excited states, and inversely proportional to the energy difference between the states. It is shown that the paramagnetic terms is drastically changed depending on the conformation, owing to the orbital interactions around the nitrogen, which have large contribution to HOMO. In the investigation, the conformational dependence of HOMO is also presented. Based on these results, the relationship between the conformation and charge-transport property is considered.

It is shown that the division of the diamagnetic and paramagnetic NMR shielding is effective to understand the electronic structure.

In Chapter 4, the charged states of TPD are investigated. According to the cyclic voltammetry (CV) and UV/Vis-NIR spectroelectrochemistry, the cationic and dicationc states exist for charged TPD [31]. All of the neutral, cationic, and dicationic states are investigated by solid-state ^{15}N NMR experiments. The observed ^{15}N isotropic chemical shifts differ substantially, depending on the charged states. The results indicate that the observation of charge-transport process in the devices would be possible by detecting the ^{15}N isotropic chemical shifts by solid-state NMR experiments. The experimental ^{15}N CSA spectra are also obtained for the neutral and charged samples, agreeing well with those obtained by DFT calculations. By analyzing the CSA spectra by DFT calculations, the direction from which electrons are extracted is obtained. The results mean that the solid-state NMR is powerful for the analysis of the electronic structure of organic molecules in charged states.

In Chapter 5, both the reorganization energies and charge transfer integrals are investigated for TPD to quantify the charge-transfer rate constants, in the basis of Marcus theory. The calculations are carried out for all the adjacent molecular pairs in the crystals, analyzing all of the Coulomb, resonance, and overlap integrals between the frontier orbitals by extended Hückel method. In addition, percolated charge-transport paths in the condensed state are considered to understand the charge transports in devices. The paths consist of consecutive molecular pairs with large values of charge-transfer rate constants. When the percolated paths do exist, charges can be effectively transported from one electrode to the counter electrode by hopping mechanism. From the analysis, the advantageous paths for hole transports are found for the condensed TPD, while those for electron transports are not. The results qualitatively explain the experimental results that hole mobility, 10^{-3} cm^2/Vs, is several orders of magnitudes larger

than electron mobility, < 10^{-7} cm^2/Vs [28]. It is suggested that this method can be valid to understand the charge transports by hopping mechanism.

In Chapter 6, the charge-transfer rate constants for 4,4'-*N*,*N'*-dicarbazolylbiphenyl (CBP) [48-55] are quantified as in the case of TPD in Chapter 5. Although the chemical structures of TPD and CBP are similar to each other, CBP has a bipolar charge-transport property, that is, the hole and electron mobilities are comparable, both in the order of 10^{-3} cm^2/Vs [52,53]. However, the origins of the bipolar charge-transport property are unclear. By considering both the reorganization energies and charge transfer integrals as in Chapter 5, the bipolar property of CBP is consistently explained. From the detailed analysis, information on which segments of the molecule are dominant for charge transfers is obtained. For CBP, both the HOMO and LUMO are spread over the molecule. Therefore, intermolecular overlaps are easily formed for both the HOMO and LUMO, resulting in the large and compatible values of hole and electron transfer integrals. In contrast, the LUMO of TPD is localized on the central biphenylene moiety, leading to the small values of electron transfer integrals. It is suggested that delocalizations of the MOs are one of the important factors for the intermolecular charge transfers, and thus for the charge-transport property of these triphenylamine-related materials. The findings are helpful for designs of molecules with better carrier mobilities.

References

[1] C. W. Tang, S.A. VanSlyke, Appl. Phys. Lett. 51 (1987) 913.

[2] C. Adachi, S. Tokito, T. Tsutsui, S. Saito, Jpn. J. Appl. Phys. 27 (1988) L269.

[3] C. Adachi, T. Tsutsui, S. Saito, Appl. Phys. Lett. 57 (1990) 531.

[4] J. Kido, K. Hongawa, K. Nagai, K. Okuyama, Appl. Phys. Lett. 65 (1994) 2124.

[5] J. Kido, M. Kimura, K. Nagai, Science 267 (1995) 1332.

[6] V. Bulović, G. Gu, P.E. Burrows, S.R. Forrest, M.E. Thompson, Nature 380 (1996) 29.

[7] D.F. O'Brien, M.A. Baldo, M.E. Thompson, S.R. Forrest, Appl. Phys. Lett. 74 (1999) 442.

[8] M.A. Baldo, S. Lamansky, P.E. Burrows, M.E. Thompson, S.R. Forrest, Appl. Phys. Lett. 75 (1999) 4.

[9] C. Adachi1, M.A. Baldo, S.R. Forrest, M.E. Thompson, Appl. Phys. Lett. 77 (2000) 904.

[10] P.T. Furuta, L. Deng, S. Garon, M.E. Thompson, J. M. J. Frechet, J. Am. Chem. Soc. 126 (2004) 15388.

[11] M. Suzuki, S. Tokito, F. Sato, T. Igarashi, K. Kondo, T. Koyama, T. Yamaguchi, Appl. Phys. Lett. 86 (2005) 103507.

[12] D.F. O'Brien, P.E. Burrows, S.R. Forrest, B.E. Koene, D.E. Loy, M.E. Thompson, Adv. Mater. 10 (1998) 1108.

[13] H. Sirringhaus, P.J. Brown, R.H. Friend, M.M. Nielsen, K. Bechgaard, B.M. Langeveld-Voss, A.J.H. Spiering, R.A.J. Janssen, E.W. Meijer, P. Herwig, D.M. de Leeuw, Nature 401 (1999) 685.

[14] K. Sakanoue, M. Motoda, M. Sugimoto, S. Sakaki, J. Phys. Chem. A 103 (1999) 5551.

[15] M. Malagoli, J.L. Brédas, Chem. Phys. Lett. 327 (2000) 13.

[16] J. Cornil, N.E. Gruhn, D.A. dos Santos, M. Malagoli, P.A. Lee, S. Barlow, S. Thayumanavan, S.R. Marder, N.R. Armstrong, J.L. Brédas, J. Phys. Chem. A 105 (2001) 5206.

[17] M. Malagoli, M. Manoharan, B. Kippelen, J.L. Brédas, Chem. Phys. Lett. 354 (2002) 283.

[18] B.C. Lin, C.P. Cheng, Z.P.M. Lao, J. Phys. Chem. A 107 (2003) 5241.

[19] B.C. Lin, C.P. Cheng, Z.Q. You, C.P. Hsu, J. Am. Chem. Soc. 127 (2005) 66.

[20] M. Brinkmann, G. Gadret, M. Muccini, C. Taliani, N. Masciocchi, A. Sironi, J. Am. Chem. Soc. 122 (2000) 5147.

[21] M. Muccini, M.A. Loi, K. Kenevey, R. Zamboni, N. Masciocchi, A. Sironi, Adv. Mater. 16 (2004) 861.

[22] H. Kaji, Y. Kusaka, G. Onoyama, F. Horii, Jpn. J. Appl. Phys. 44 (2005) 3706.

[23] H. Kaji, Y. Kusaka, G. Onoyama, F. Horii, J. Am. Chem. Soc. 128 (2006) 4292.

[24] A.R. West, Basic Solid State Chemistry, John Wiley & Sons Ltd., West Sussex, 1994.

[25] M. Stolka, J.F. Yanus, D.M. Pai, J. Phys. Chem. 88 (1984) 4707.

[26] H. Ishii, K. Seki, IEEE Trans. Electron Devices 44 (1997) 1295.

[27] H. Murata, C.D. Merritt, Z.H. Kafafi, IEEE J. Sel. Top. Quantum Electron. 4 (1998) 119.

[28] H. Mattoussi, H. Murata, C.D. Merritt, Y. Iizumi, J. Kido, Z.H. Kafafi, J. Appl. Phys. 86 (1999) 2642.

[29] K. Seki, N. Hayashi, H. Oji, E. Ito, Y. Ouchi, H. Ishii, Thin Solid Films 393 (2001) 298.

[30] A.R. Kennedy, W.E. Smith, D.R. Tackley, W.I.F. David, K. Shankland, B. Brown, S.J. Teat, J. Mater. Chem. 12 (2002) 168.

[31] P.J. Low, M.A.J. Paterson, H. Puschmann, A.E. Goeta, J.A.K. Howard, C. Lambert, J.C. Cherryman, D.R. Tackley, S. Leeming, B. Brown, Chem. Eur. J. 10 (2004) 83.

[32] Z. Zhang, E. Burkholder, J. Zubieta, Acta Cryst. C60 (2004) o452.

[33] K. Shankland, A.R. Kennedy, W.I.F. David, J. Mater. Chem. 15 (2005) 4838.

[34] K. Schmidt-Rohr, Macromolecules 29 (1996) 3975.

[35] K. Schmidt-Rohr, W. Hu, N. Zumbulyadis, Science 280 (1998) 714.

[36] H. Kaji, K. Schmidt-Rohr, Macromolecules 33 (2000) 5169.

[37] H. Kaji, K. Schmidt-Rohr, Macromolecules 34 (2001) 7368.

[38] R.A. Marcus, J. Chem. Phys. 24 (1956) 966.

[39] R.A. Marcus, N. Sutin, Biochim. Biophys. Acta 811 (1985) 265.

[40] H. Bässler, Phys. Stat. Sol. B 175 (1993) 15.

[41] P.F. Barbara, T.J. Meyer, M.A. Ratner, J. Phys. Chem. 100 (1996) 13148.

[42] L. Rodriguez-Monge, S. Larsson, J. Phys. Chem. 100 (1996) 6298.

[43] J. Cornil, D. Beljonne, J.P. Calbert, J.L. Brédas, Adv. Mater. 13 (2001) 1053.

[44] J.L. Brédas, J.P. Calbert, J. Cornil, Proc. Natl. Acad. Sci. USA 99 (2002) 5804.

[45] G.R. Hutchison, M.A. Ratner, T.J. Marks, J. Am. Chem. Soc. 127 (2005) 16866.

[46] J. Kirkpatrick, J. Nelson, J. Chem. Phys. 123 (2005) 084703.

[47] A. Datta, S. Mohakud, S.K. Pati, J. Chem. Phys. 126 (2007) 144710.

[48] H. Kanai, S. Ichinosawa, Y. Sato, Synt. Met. 91 (1997) 195.

[49] B.E. Koene, D.E. Loy, M.E. Thompson, Chem. Mater. 10 (1998) 2235.

[50] C. Adachi, M.A. Baldo, S.R. Forrest, J. Appl. Phys. 87 (2000) 8049.

[51] C. Adachi, R. Kwong, S.R. Forrest, Org. Electron. 2 (2001) 37.

[52] N. Matsusue, Y. Suzuki, H. Naito, Jpn. J. Appl. Phys. 44 (2005) 3691.

[53] H. Matsushima, S. Naka, H. Okada, H. Onnagawa, Curr. Appl. Phys. 5 (2005) 305.

[54] Y. Wang, Y. Hua, X. Wu, L. Zhang, Q. Hou, F. Guan, N. Zhang, S. Yin, X. Cheng, Org. Electron. 9 (2008) 692.

[55] Y. Tao, Q. Wang, L. Ao, C. Zhong, J. Qin, C. Yang, D. Ma, J. Mater. Chem. 20 (2010) 1759.

Chapter 2

A Combined Experimental and Theoretical Study of the Amorphous Structure of *N,N'*-diphenyl-*N,N'*-di(*m*-tolyl)benzidine (TPD) Using Solid-State ^{15}N NMR and DFT Calculations

2.1. Introduction

N,N'-diphenyl-*N,N'*-di(*m*-tolyl)benzidine (TPD) (see Fig. 2.1) is one of the widely-known hole-transport materials for organic light-emitting diodes (OLEDs) [1-12]. In order to investigate the relationships between the molecular structure and the hole-transport property, and to obtain guidelines for designing molecules with excellent performance, quantum chemical calculations were performed for TPD and related compounds [13-17]. The calculations for a single TPD molecule suggested that the small reorganization energy for hole transfer is an important factor for its hole-transporting effectiveness [13,17]. Recently, X-ray diffraction (XRD) analyses were carried out for TPD crystal to clarify the molecular structure in the condensed state [18-20]. Consisting with the results of quantum chemical calculations, the XRD analyses showed that the structure around the nitrogen atoms of TPD is planar, that is, the nitrogen atoms and the three carbon atoms directly bonded to the nitrogen atoms are in the same plane ($\theta_1 + \theta_2 + \theta_3 = 360^o$, see Fig. 2.1). This is sharp contrast with most amine compounds, in which the structures around the nitrogen atoms are pyramidal. However, the torsion angles of N-C bonds (α, β, and γ in Fig. 2.1) are not comparable between the results of the quantum chemical calculations and XRD analyses. It should be noted that the OLEDs' materials, including TPD, are neither in single molecule nor in crystalline state in the device. Rather, they are in amorphous states. Therefore, direct observations of the molecular structure of amorphous TPD are desired.

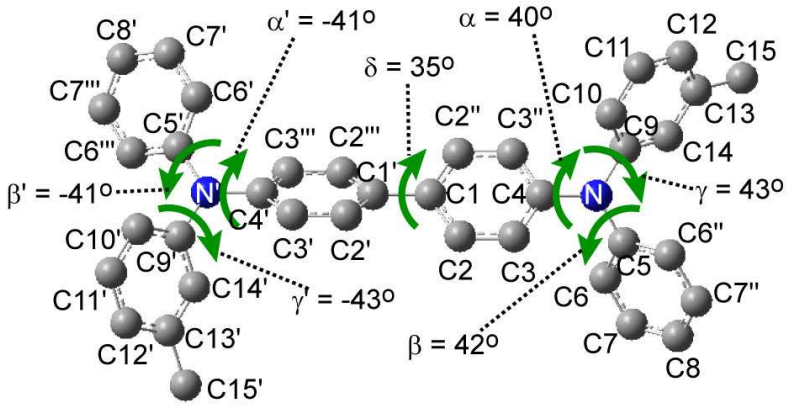

Fig. 2.1. DFT-optimized structure of *N*,*N'*-diphenyl-*N*,*N'*-di(*m*-tolyl)benzidine (TPD) for the conformer denoted v(-)-A(+)-h(+). The optimized bond angles around the nitrogen, namely θ_1, θ_2, and θ_3, are all 120°. The optimized torsion angles, α, β, γ, and δ, are also shown.

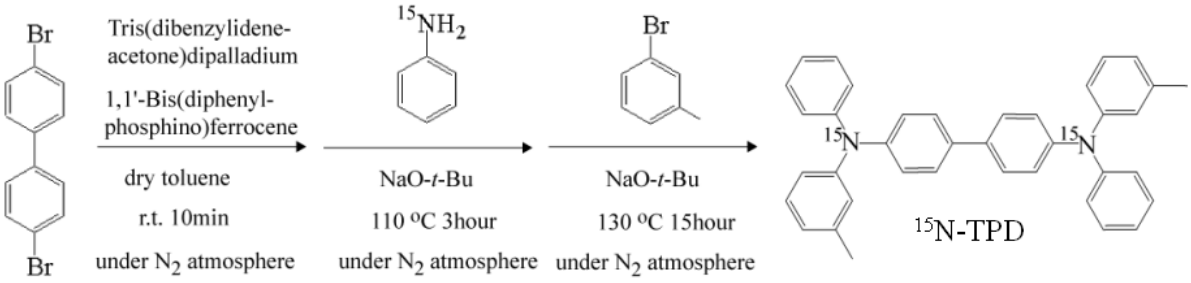

Scheme 2.1. The synthetic route of ^{15}N-labeled TPD (^{15}N-TPD) sample.

In this study, the planarity around the nitrogen atoms and the torsion angles of N-C bonds of amorphous TPD are investigated by the combined use of solid-state NMR experiments and density functional theory (DFT) calculations. Solid-state NMR is one of the most suitable tools for the investigation of disordered materials including amorphous solids [21-27]. From the solid-state NMR experiments the experimental ^{15}N CSA spectrum for ^{15}N-labeled TPD (^{15}N-TPD) in the amorphous state is obtained. In addition, the structural dependences of ^{15}N chemical shift anisotropy (CSA) are calculated by DFT method. Comparing these experimental and computed CSA data, the molecular structure of amorphous TPD is analyzed. It is also shown that the planarity around the nitrogen atoms affects the HOMO and intermolecular distance, both of which are important factors for hole transports by the hopping mechanism [28-31].

2.2 Experimental and Computational Section

2.2.1. Samples

^{15}N-TPD sample was obtained by the synthetic route shown in Scheme 2.1 [32]. To a 100 mL three-necked round-bottomed flask containing 4,4'-Dibromobiphenyl (1.73 g, 5.44 mmol), tris(dibenzylideneacetone) dipalladium(0) ($Pd_2(dba)_3$) (150 mg, 0.165 mmol), and 1,1'-bis(diphenylphosphino)ferrocene (DPPF) (121 mg, 0.219 mmol), dried toluene (20 mL) was added under nitrogen atmosphere. The mixture was stirred at room temperature for 10 minutes. Then, ^{15}N-labeled aniline (1.02 g, 11.0 mmol) and sodium *tert*-butoxide (2.00 g, 21.3 mmol) were added. After the reaction mixture was stirred at 110 ^{o}C for 3 hours, *m*-bromotoluene (1.88 g, 11.0 mmol) and sodium *tert*-butoxide (2.00 g, 21.3 mmol) were added. The reaction mixture was refluxed at 130 ^{o}C for 15 hours, and then quenched by pouring water.

The organic layer was purified by column chromatography on silica gel with toluene followed by 25% toluene in hexane to afford 1.80 g (64%) of ^{15}N-TPD as a white solid. ^{1}H NMR ($CDCl_3$, 300 MHz) δ 2.25 (s, 6H), 6.81-7.45 (m, 26H).

The obtained ^{15}N-TPD sample was quenched to 0 ^{o}C from the melt at 200 ^{o}C and dried at room temperature under vacuum for one day to obtain the amorphous ^{15}N-TPD (^{15}N-aTPD) sample.

2.2.2. Solid-State ^{15}N NMR Experiments

The solid-state ^{15}N NMR experiments were carried out for ^{15}N-aTPD, using a Chemagnetics CMX-400 spectrometer operating at a static magnetic field of 9.4 T and a ^{15}N frequency of 40.4 MHz. A 7.5-mm magic angle spinning (MAS) probehead was used. For the ^{1}H and ^{15}N channels, the 90^{o} pulse lengths were 4.0 and 6.0 μs, respectively. The CP/MAS and CSA measurements were performed. For the CP/MAS measurement, the MAS rate was 6 kHz to obtain the isotropic chemical shift, σ_{iso}. For the CSA measurement, the Hahn echo (τ-π-pulse-τ) with τ = 20 μs was applied before the detection of a free induction decay (FID). The spectrum was obtained without sample spinning. In the measurement, a resonant frequency, ω_0, in Eq. 2.1 is observed. It depends on the relative orientation of static magnetic filed, $\boldsymbol{B_0}$, in the principal axes system [21].

$$\omega_0 / 2\pi = \sigma_{11} \sin^2\theta \cos^2\phi + \sigma_{22} \sin^2\theta \sin^2\phi + \sigma_{33} \cos^2\theta \qquad (2.1)$$

Here, θ and ϕ express the polar coordinates of $\boldsymbol{B_0}$ in the principal axes system. The σ_{11}, σ_{22}, and σ_{33} are the chemical shift principal values, and they are denoted from the downfield side of the spectrum. The average of these principal values corresponds to the isotropic chemical shift.

All the NMR measurements were carried out at 23 ^{o}C. The ^{15}N chemical shifts were expressed as values relative to liquid ammonia (NH_3) using the resonance line of solid $^{15}NH_4Cl$ at 39.1 ppm as external [33,34].

2.2.3. Computations

The optimization of the molecular structure of a TPD molecule was carried out at the DFT level using the B3LYP functional, in which Beck's three-parameter hybrid exchange functional is combined with the Lee-Yang-Parr correlation functional [35-39]. The 6-31G(d) basis set [40-44] was used. The validity of this basis set for the structural optimization was already investigated [13-17].

The principal values of the ^{15}N shielding tensor, σ_{11}', σ_{22}', and σ_{33}', for the optimized TPD molecule were calculated using the B3LYP functional with the gauge-including atomic orbital (GIAO) method [40]. The relationship between the principal values of shielding tensor and chemical shift tensor is expressed as

$$\sigma_{ii} = \sigma_{ref}' - \sigma_{ii}' \quad (ii = 11, 22, \text{or } 33) \tag{2.2}$$

where, σ_{ref}' is the shielding constant for a reference material. In order to choose an appropriate basis set for the calculations, the principal values of ^{15}N shielding tensor were calculated using the several basis sets from STO-3G to 6-311+G(2d,p). Fig. 2.2a shows the calculated values of σ_{11}', σ_{22}', σ_{33}', and $\sigma_{11} - \sigma_{33}$ (= $\sigma_{33}' - \sigma_{11}'$). The value of $\sigma_{11} - \sigma_{33}$ is called "CSA span", hereafter. Only the values for the right nitrogen are shown in the figure, because the values for the right and left nitrogens are comparable. While the accuracy of the absolute values of σ_{11}', σ_{22}', and σ_{33}' is unclear, the CSA span is almost constant irrespective of the basis set; the values

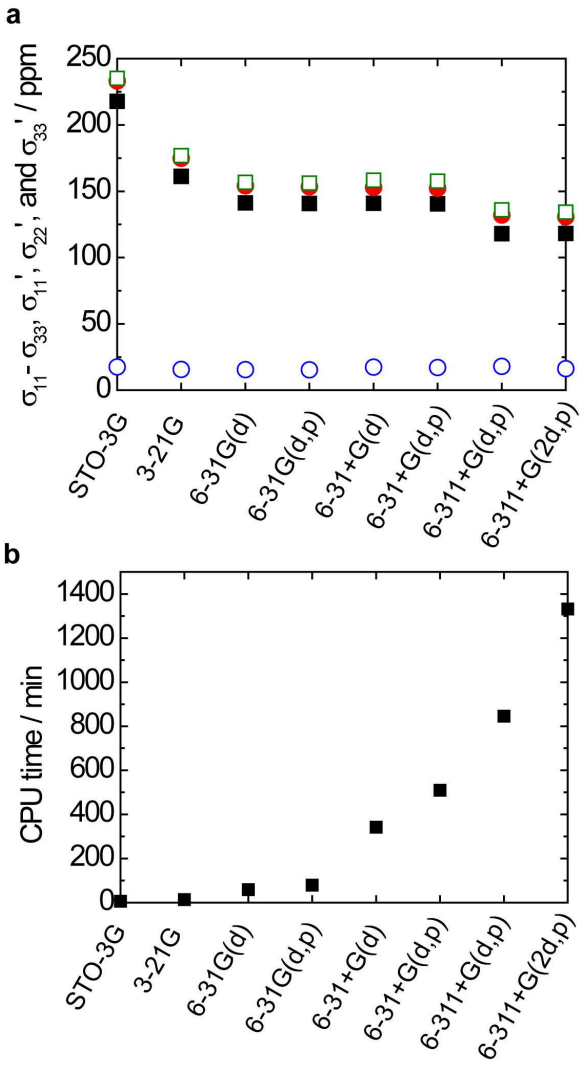

Fig. 2.2. (a) Basis set dependence of the principal values of the ^{15}N shielding tensor, σ_{11}' (■), σ_{22}' (●), and σ_{33}' (□) and the values of the CSA span, $\sigma_{11} - \sigma_{33}$, (○) for the DFT-optimized TPD single molecule. Since the values for the right and left nitrogen nuclei are almost the same, only those values corresponding to the right nitrogen nucleus are shown. (b) Basis set dependence of CPU time for the calculations.

are 16.6 ± 1.4 ppm for all the basis sets. Fig. 2.2b represents the CPU time for the calculations performed by SGI Origin3800, using 8 CPUs with the clock frequency of 500 MHz. For example, the calculation time for 6-31G(d) basis set is less than one fifth of that for 6-31+G(d) basis set. The basis set of 6-31G(d) was adopted for the investigations to obtain the value of ^{15}N CSA span in reasonable time. The NMR calculations were carried out changing the planarity around the nitrogen atoms and torsion angles of N-C bonds from the DFT-optimized geometry to obtain the molecular structural dependences of the ^{15}N CSA span. All the calculations were carried out for an isolated TPD molecule with the Gaussian 03 program [45].

2.3. Results and Discussion

2.3.1. DFT-Optimized Structures

Fig. 2.1 shows one of the stable conformers obtained by DFT-optimizations. The features are as follow; the nitrogen and three carbons atoms directly bonded to the nitrogen atom are in the same plane, and the three rings attached to the nitrogen adopt a propeller-shape conformation. Note that TPD has a specific conformational freedom, allowing the 40 different stable conformers. (1) A 180^o rotation of the C9'N'NC9 virtual bond makes two kinds of conformers, *anticlinal* (A) and *gauche* (G). Here, the denotations of A and G are the IUPAC designation for torsion angles; the torsion angles are defined in the range $-180^o < \psi < 180^o$ and conformation with torsion angles within ±30^o from ±180^o, ±120^o, ±60^o, and 0^o are designated as T, A, G, and C, respectively. Changing the sign (positive and negative) for the torsion angle, δ, also makes two different conformers. (2) A 180^o rotation of the tolyl ring (rotation of N-C9 bond, corresponding to torsion angle, γ) allows two additional kinds of conformers, in which the methyl group is either vertical (v) or horizontal (h) against the virtual N'-N bond. For the

triphenylamine (TPA) moieties, two different conformers exist depending on the propeller chirality, for which the torsion angle set is (α, β, γ) or ($-\alpha$, $-\beta$, $-\gamma$). Table 2.1 shows the 40 optimized stable conformers with the point groups and relative energies. The respective conformers are described such as v(-)-A(+)-h(+). The v or h on the left and right indicate the direction of methyl groups in the left and right tolyl groups, respectively. The (-) or (+) on the left and right correspond to the propeller chirallity of the left and right TPA moieties, respectively. The A(+) at the center means that the torsion angle of the C9'N'NC9 virtual bond is *anticlinal* and the sign of the torsion angle, δ, is positive. The 40 conformers in Table 2.1 are considered to exist in amorphous state, since the maximum energy difference among these conformers, 1.76 kJ mol^{-1}, is smaller than the thermal energy at room temperature, 2.5 kJ mol^{-1}. Note that the thermal energy during thermal deposition processes is much larger. In Table 2.1, 16 conformers which have the structures, v(+)-*-v(+),v(-)-*-v(-), h(+)-*-h(+), and h(-)-*-h(-), exhibit C_2 symmetry (the symbol of * indicates an arbitrary conformation). The remaining 24 conformers have C_1 symmetry. In contrast, TPA is more symmetrical (D_3). This lower symmetry of TPD and existence of various conformers would be one of the reasons why the structural analyses of TPD are difficult even for the crystalline state.

2.3.2. Solid-State NMR Results for Amorphous TPD

Fig. 2.3a shows the experimental ^{15}N CP/MAS spectrum of ^{15}N-aTPD. A relatively broad single resonance line is observed at 100.4 ppm. Fig. 2.3b shows the experimental ^{15}N CSA spectrum of ^{15}N-aTPD. Due to the narrowness of the CSA, distinct principal values of σ_{11}, σ_{22}, and σ_{33} cannot be precisely determined. Therefore, the CSA span, which corresponds to the value of $\sigma_{11} - \sigma_{33}$, is used for the analyses. The experimental CSA span is found to be about 15 ppm from Fig. 2.3b. The value is very small, compared with the ^{15}N CSA spans in most

Table 2.1. Point groups and relative energies (kJ mol^{-1})[a] for stable conformers of TPD. The optimizations were carried out without symmetry constraint.

	v(+)	v(-)	h(+)	h(-)
For *-A(+)-*				
v(+)	C_2, 0.62	C_1, -0.16	C_1, 0.59	C_1, -0.20
v(-)	-	C_2, -0.87	C_1, 0	C_1, -0.89
h(+)	-	-	C_2, 0.86	C_1, -0.01
h(-)	-	-	-	C_2, -0.90
For *-A(-)-*				
v(+)	C_2, -0.87	C_1, -0.02	C_1, -0.89	C_1, -0.01
v(-)	-	C_2, 0.57	C_1, -0.20	C_1, 0.59
h(+)	-	-	C_2, -0.90	C_1, -0.01
h(-)	-	-	-	C_2, 0.61
For *-G(+)-*				
v(+)	C_2, 0.63	C_1, -0.21	C_1, 0.81	C_1, -0.22
v(-)	-	C_2, -0.62	C_1, 0.01	C_1, -0.89
h(+)	-	-	C_2, 0.61	C_1, 0.16
h(-)	-	-	-	C_2, -0.63
For *-G(-)-*				
v(+)	C_2, -0.87	C_1, -0.21	C_1, -0.89	C_1, -0.09
v(-)	-	C_2, 0.63	C_1, -0.22	C_1, 0.58
h(+)	-	-	C_2, -0.43	C_1, 0.06
h(-)	-	-	-	C_2, 0.61

[a] The energies are shown by the difference from the energy of the conformer, v(-)-A(+)-h(+), -1.40×10^6 kJ mol^{-1}.

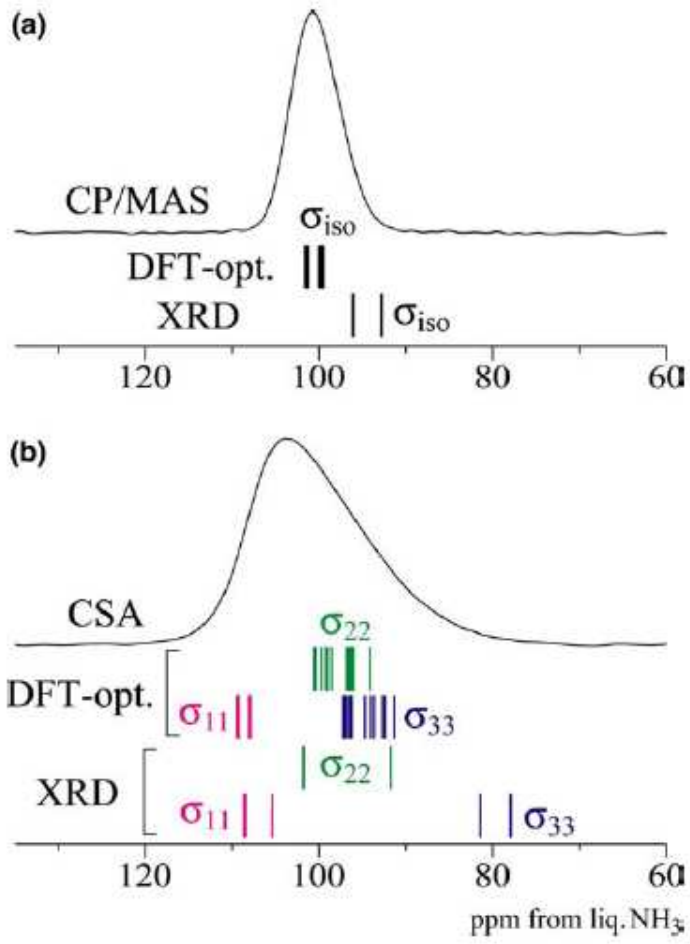

Fig. 2.3. (a) Experimental ^{15}N CP/MAS spectrum of ^{15}N-aTPD. (b) Experimental ^{15}N CSA spectrum of 15N-aTPD. The σ_{iso}, σ_{11}, σ_{22}, and σ_{33} for the DFT-optimized TPD and TPD obtained by XRD analysis [18] are also shown by the vertical bars.

cases [34,46]. The narrow CSA spectrum does not originate from the effect of dynamics. This was confirmed by ^{13}C CSA measurements of C1 carbon ^{13}C-labeled TPD and C5 carbon ^{13}C-labeled TPD. For both of the samples, the experimental values of σ_{11}, σ_{22}, and σ_{33} agreed well with the DFT-calculated values, in which the effect of dynamics was not taken into. It is impossible that the nitrogen atoms are mobile under the condition that these carbon atoms are rigid.

2.3.3. Molecular Structure of TPD in Amorphous State

Fig. 2.4 represents the DFT-calculated ^{15}N CSA spans as a function of structural planarity around the nitrogen, which is quantified by the summation of bond angles, $\theta_1 + \theta_2 + \theta_3$. All the other parameters are the DFT-optimized values. The values of θ_1, θ_2, and θ_3 are assumed to be equal in these calculations based on both the structural similarity and the results of DFT optimization. The calculations were carried out at 10^o intervals of $\theta_1 + \theta_2 + \theta_3$. The values for the both TPA moieties are changed equivalently. From Fig. 2.4, it is found that the CSA span increases almost linearly from 11.2–15.9 ppm to 96.8–97.1 ppm for the left and right nitrogens, respectively, as the $\theta_1 + \theta_2 + \theta_3$ value decreases from 360 to 310^o. The strong planarity dependence of the CSA span indicates that the $\theta_1 + \theta_2 + \theta_3$ value can be determined from the experimental ^{15}N CSA span. It is found from Fig. 2.4 that the experimental ^{15}N CSA span for amorphous TPD, 15 ppm, corresponds to the $\theta_1 + \theta_2 + \theta_3$ value of ~360^o. This indicates that the molecular structure around the nitrogen is planar in amorphous TPD.

The torsion angles, α, β, and γ, are also investigated from the ^{15}N CSA span. Fig. 2.5 shows the DFT-calculated ^{15}N CSA spans plotted as a function of the torsion angles, α and β, under the condition that the torsion angles of β and γ are equivalent with each other, based on the structural similarity. All the other parameters are the DFT-optimized values. In the

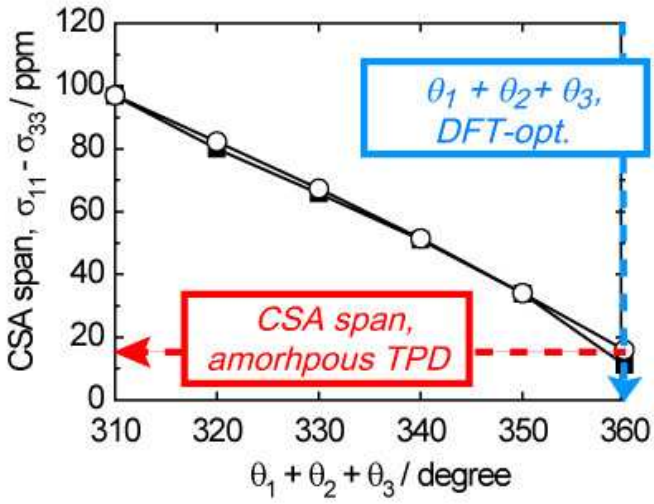

Fig. 2.4. DFT-calculated $\sigma_{11} - \sigma_{33}$ values of ^{15}N nuclei of TPD as a function of the planarity around the nitrogen, $\theta_1 + \theta_2 + \theta_3$. The open circles and filled squares represent the values for the right and left nitrogen nuclei, respectively. All the other parameters are fixed to the DFT-optimized values.

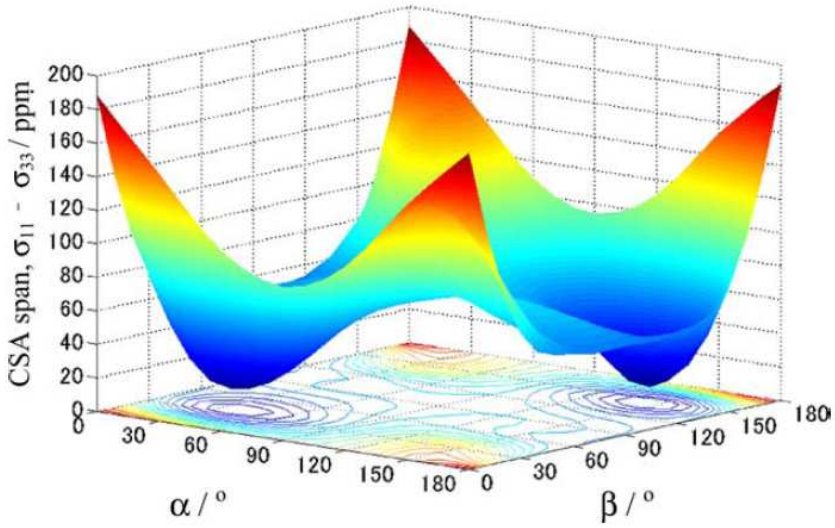

Fig. 2.5. DFT-calculated $\sigma_{11} - \sigma_{33}$ values of ^{15}N nuclei of TPD as a function of the torsion angles α and β under the assumption of $\beta = \gamma$. All the other parameters are fixed to the DFT-optimized values. The calculations were carried out with the interval of 30^{o} and a two-dimensional interpolation is applied for the graphical presentation. Only the values for the right nitrogen of TPD are shown.

calculations, the torsion angles are changed for both of the two TPA moieties of TPD, and the CSA spans for the right nitrogen in Fig. 2.1 are shown. The calculations were carried out with 30^o intervals and a two-dimensional interpolation was applied for the graphical presentation. From Fig. 2.5, the CSA spans are found to strongly depend on the torsion angles and thus can be used for the torsion angle determination. Two local minima are found within the angle region in Fig. 2.4. One of the minima is near the point of (α, β) = (40^o, 40^o), which is comparable with the conformer, v(-)-A(+)-h(+), and the other minimum is near the point of (α, β) = (140^o, 140^o), corresponding to the conformer, h(+)-A(+)-v(-). These conformers correspond to the DFT-optimized structures in Table 2.1. Because the values of CSA span for the above two minima are almost comparable with that the value obtained for ^{15}N-aTPD, ~15 ppm, the torsion angles in the amorphous state are suggested to be (α, β) = (40^o, 40^o) or (140^o, 140^o). Both of the angle sets can exist, due to the small energy difference as described in Table 2.1. Figs. 2.6a and 2.6b respectively show more detailed α and β dependences of the ^{15}N CSA spans under the condition that all the other parameters are the DFT-optimized values. Two lines in the respective figures are for two nitrogen nuclei in the TPD molecule. It is found that the DFT-optimized structure with the torsion angle, α or β (= γ), of ~40^o gives the almost narrowest CSA span, ~15 ppm, leading to the same conclusion in Fig. 2.5 that the torsion angles determined by the experimental CSA span agree well with those for the DFT-optimized structure.

It must be noted that the above investigations are independently carried out for the planarity and torsion angles. Here, the both parameters are analyzed concurrently for careful investigations. Fig. 2.7 represents the DFT-calculated ^{15}N CSA span as a function of the planarity, $\theta_1 + \theta_2 + \theta_3$, and torsion angle, α. The calculations were performed at 10^o intervals for both of the $\theta_1 + \theta_2 + \theta_3$ and α values under the condition that $\theta_1 = \theta_2 = \theta_3$ and $\alpha = \beta = \gamma$.

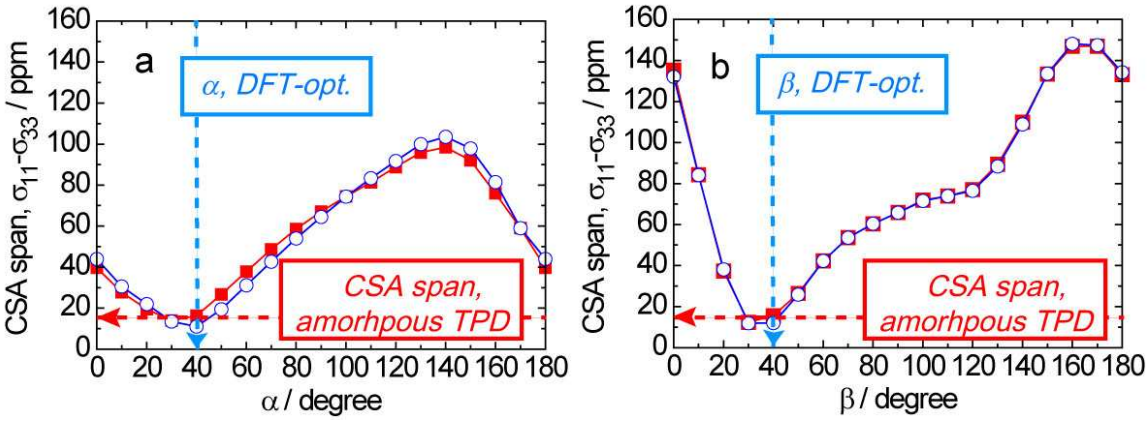

Fig. 2.6. DFT-calculated $\sigma_{11} - \sigma_{33}$ values of a ^{15}N nucleus of TPD as a function of torsion angles, (a) α and (b) β. The open circles and filled squares represent the values for the right and left nitrogen nuclei, respectively. All the other parameters are fixed to the DFT-optimized values.

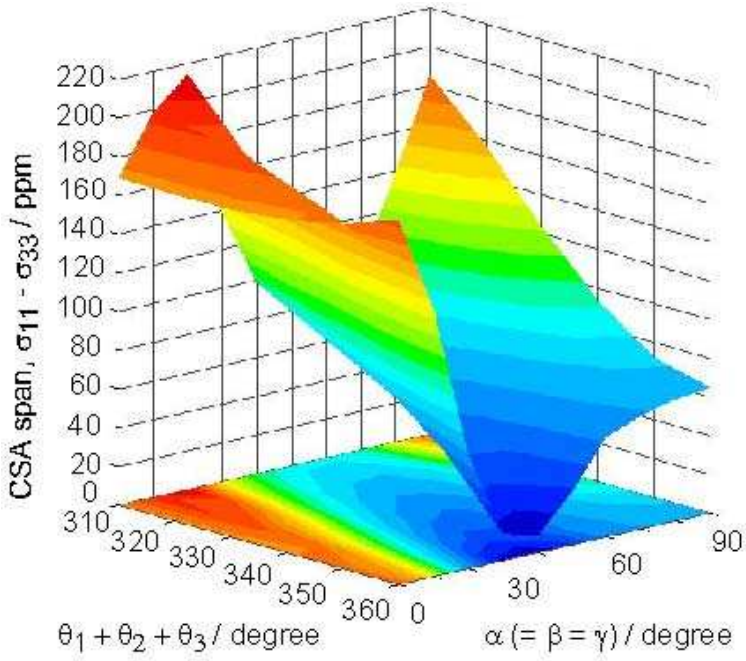

Fig. 2.7. DFT-calculated $\sigma_{11} - \sigma_{33}$ values of a ^{15}N nucleus of TPD as a function of the planarity around the nitrogen, $\theta_1 + \theta_2 + \theta_3$, and the torsion angles, α (= β = γ). All the other parameters are fixed to the DFT-optimized values. Only the values for the right nitrogen nucleus are shown.

All the other parameters were the DFT-optimized values. Fig. 2.7 reveals that the ^{15}N CSA span depends strongly on $\theta_1 + \theta_2 + \theta_3$ and α values. A minimum is found around ($\theta_1 + \theta_2 + \theta_3$, α) = (360^o, 40^o) which corresponds to the DFT-optimized molecular structure. The minimum value closely agrees with the experimental ^{15}N CSA span for amorphous TPD, 15 ppm. We cannot find any other parameter sets of ($\theta_1 + \theta_2 + \theta_3$, α) in Fig. 2.7 that agree with the experimental ^{15}N CSA span. The result certainly leads that the structure around the nitrogen of amorphous TPD is planar and the torsion angles are ~40^o for all of the N-C bonds, consisting with the DFT-optimized structure. This is in sharp contrast to most of the amine compounds, which have pyramidal structures [47].

2.3.4. Comparison with XRD Data

Recently, the XRD analysis was carried out for the single crystal of TPD [18]. The result is partly different from the DFT results. For the DFT-optimized TPD, the corresponding torsion angles on the left and right TPA moieties are the same within the experimental error; the torsion angles are 39-42^o for α ($\angle$C3C4NC5 ≈ $\angle$C3'C4'N'C5' ≈ $\angle$C3''C4NC9 ≈ $\angle$C3'''C4'N'C9') and 41-44^o for β and γ ($\angle$C4NC5C6 ≈ $\angle$C4NC9C10 ≈ $\angle$C3'N'C5'C6' ≈ $\angle$C4'N'C9'C10'), where the condition of $\beta = \gamma$ holds. However, this is not the case for the XRD results. From the XRD experiments, the conformer 1, v(-)-G(-)-h(-), and the conformer 2, v(-)-A(-)-h(-), were reported. The absolute torsion angles are compatible between the two conformers, while each conformer gives four different α values, $\angle$C3C4NC5 = 44.8^o (phenyl ring-side) and $\angle$C3C4NC9 = 33.6^o (tolyl ring-side) for the left TPA moiety, and $\angle$C3C4NC5 = 27.5^o (phenyl ring-side) and $\angle$C3C4NC9 = 18.9^o (tolyl ring-side) for the right TPA moiety. The different torsion angles for the left and right TPA moieties and for the phenyl ring- and tolyl ring-sides indicate the disorder of the geometry. For the other two angles, β and γ, two different angles

are obtained for the left and right TPA moieties; β = (33.3°, 43.8°) and γ = (51.8°, 56.3°), respectively. The most extreme differences are ∠C3C4NC9 (XRD: 18.9° vs. DFT: 42°) and ∠C10C9NC4 (XRD: 56.3° vs. DFT: 42 °). The DFT-calculated σ_{11}, σ_{22}, and σ_{33} values for molecular structure obtained by XRD analysis are shown in Fig. 2.3. A significant inconsistency is observed for the σ_{33} values, leading to the values of the CSA span of 23.9 and 30.5 ppm for the left and right nitrogen atoms of conformer 1. Similarly, the results of 24.0 and 30.7 ppm were obtained for conformer 2. If these conformers exist in amorphous state, the CSA spectrum in Fig. 2.3b should be as broad as 30.5–30.7 ppm. Therefore, existences of these conformers in the amorphous state are denied by the CSA spectrum. The inconsistency is considered to originate from the structure modification due to the crystalline packing effect. The consistency between the molecular structure in amorphous state and that obtained for a single molecule by DFT calculations suggests that the intermolecular interactions in amorphous state do not affect the molecular structure.

2.3.5. Planarity Effects on HOMO

It is clear from the above calculations that the ^{15}N CSA span is closely linked to planarity around the nitrogen. Amorphous TPD exhibits an exceedingly narrow CSA span. Therefore, the magnetic shielding by electron clouds around the nitrogen nucleus is almost spherical when the molecular structure around the nitrogen is planar. The anisotropy of the magnetic shielding increases as the value of $\theta_1 + \theta_2 + \theta_3$ decreases. The change in the anisotropy of the magnetic shielding indicates that the shape of the electron clouds around the nitrogen is strongly affected by the planarity. Here, the planarity dependence of the shape of HOMO is considered, because the MO is closely tied to hole-transport performance. Figs. 2.8a and 2.8b show the DFT-calculated HOMO for the planar ($\theta_1 + \theta_2 + \theta_3 = 360°$) and pyramidal ($\theta_1 + \theta_2 + \theta_3 = 310°$)

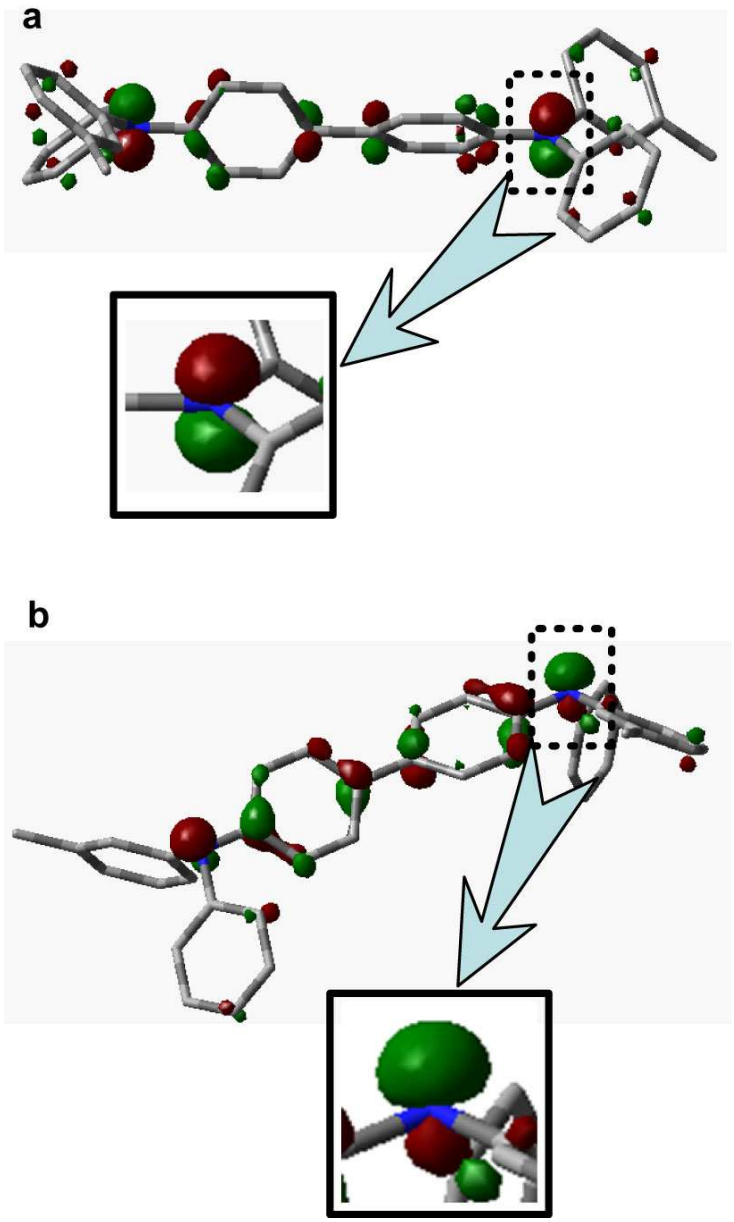

Fig. 2.8. HOMO of a TPD molecule in the case of (a) a planar structure with $\theta_1 + \theta_2 + \theta_3 = 360^o$ and (b) a pyramidal structure with $\theta_1 + \theta_2 + \theta_3 = 310^o$. Enlarged images show the area around the nitrogen atom. Isosurface values are 0.040 a.u.

structures, respectively. For the planar structure, HOMO around the nitrogen is distributed evenly on both sides of the plane. Natural bond orbital (NBO) analysis [48] shows us that the nitrogen atom is sp^2 hybridized. By contrast, in the case of the pyramidal structure, HOMO around the nitrogen extends mostly to one side of the pyramidal structure while the contribution from the other side is small. This pyramidal structure corresponds to the sp^3 (to be exact, $sp^{2.8}$) hybridized nitrogen. That is, the planarity has a large impact on the hybridization and the shape of HOMO. Since holes are transported through intermolecular overlaps of HOMOs, the planarity is considered to be a crucial factor for hole transports.

2.3.6. Planarity Effects on Intermolecular Distance

Intermolecular packing also affects the intermolecular overlaps of HOMO. To estimate the effect of planarity around the nitrogen on intermolecular packing, the intermolecular repulsion energies were calculated. For simplicity, the calculations were performed for TPA. Fig. 2.9 shows the repulsion energies between two TPA molecules for planar ($\theta_1 + \theta_2 + \theta_3 = 360^o$) and pyramidal ($\theta_1 + \theta_2 + \theta_3 = 310^o$) structures as a function of intermolecular distance along the C_3 axis. It is clear from the DFT-calculated results in Fig. 2.9a that the repulsion energy for the pyramidal structure is more than twice as large as that of the planar structure. A similar conclusion is arrived at if one uses Hatree-Fock calculations, although the repulsion energies in Fig. 2.9b are slightly larger than the DFT results. Therefore, the intermolecular distance for the planar structure can be shorter than that for the pyramidal structure. Accordingly, the planar structure should be advantageous for hole transports.

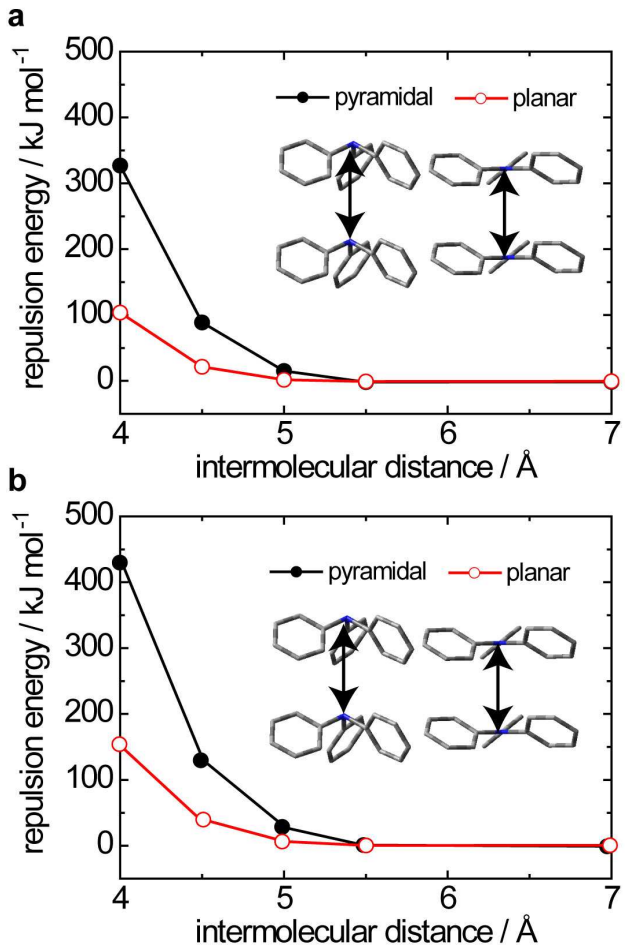

Fig. 2.9. Repulsion energies between the two triphenylamine molecules for the planar structures ($\theta_1 + \theta_2 + \theta_3 = 360^o$) (open circles) and pyramidal structures ($\theta_1 + \theta_2 + \theta_3 = 310^o$) (filled circles) as a function of intermolecular distance along the C_3 axis. (a) DFT and (b) Hartree-Fock results.

2.4. Conclusion

The conformation of amorphous TPD, a hole-transport material in OLEDs, was analyzed by solid-state ^{15}N NMR and DFT calculations. DFT calculations revealed that the ^{15}N CSA span significantly depends on the planarity and the torsion angles around the nitrogen atom, and that these structural parameters can be qualitatively determined from the CSA span. The experimental ^{15}N CSA span for amorphous TPD is in good agreement with the calculated CSA spans for the DFT-optimized TPD. This leads to the conclusion that the DFT-calculated structure of a single TPD molecule reflects the structure in the condensed amorphous state. The some differences were found between the previous XRD and DFT-optimized structures, which would originate from the crystalline packing effect. Additionally, from the solid-state NMR and DFT studies, many stable conformers are considered to exist in the amorphous state.

The significant structural dependence of the ^{15}N chemical shift parameters also indicates that the electron structure around the nitrogen nucleus differ by the geometry. Thus, the planarity and the torsion angles are crucial factors for the charge transport properties. Especially, it is found that the planarity around the nitrogen atom strongly affects the shape of HOMO and the intermolecular distance, suggesting that the plane structure is advantageous for large intermolecular overlaps of HOMO.

The molecular structure analyzed in this study would be the structure in average. Disorders will exist in the amorphous state. In order to determine the structure including the disorders, advanced solid-state NMR experiments, such as two-dimensional double-quantum (2D DOQSY) solid-state NMR experiments [22-24], are now in progress in our laboratory.

References

[1] C.W. Tang, S.A. Vanslyke, Appl. Phys. Lett. 51 (1987) 913.

[2] C. Adachi, S. Tokito, T. Tsutsui, S. Saito, Jpn. J. Appl. Phys. 27 (1988) L269.

[3] C. Adachi, K. Nagai, N. Tamoto, Appl. Phys. Lett. 66 (1995) 2679.

[4] N. Tamoto, C. Adachi, K. Nagai, Chem. Mater. 9 (1997) 1077.

[5] M. Stolka, J.F. Yanus, D.M. Pai, J. Phys. Chem. 88 (1984) 4707.

[6] S. Heun, P.M. Borsenberger, Chem. Phys. 200 (1995) 245.

[7] R.H. Young, J.J. Fitzgerald, J. Phys. Chem. 99 (1995) 4230.

[8] J. Kido, M. Kimura, K. Nagai, Science 267 (1995) 1332.

[9] V. Bulovic, G. Gu, P.E. Burrows, S.R. Forrest, M.E. Thompson, Nature 380 (1996) 29.

[10] D.F. O brien, P.E. Burrows, S.R. Forrest, B.E. Koene, D.E. Loy, M.E. Thompson, Adv. Mater. 10 (1998) 1108.

[11] K. Okumoto, K. Wayaku, T. Noda, H. Kageyama, Y. Shirota, Synth. Met. 111 (2000) 473.

[12] P. Strohriegl, J.V. Grazulevicius, Adv. Mater. 14 (2002) 1439.

[13] K. Sakanoue, M. Motoda, M. Sugimoto, S. Sakaki, J. Phys. Chem. A 103 (1999) 5551.

[14] M. Malagoli, J. Bredas, Chem. Phys. Lett. 327 (2000) 13.

[15] J. Cornil, N. Gruhn, D. Dos Santos, M. Malagoli, P. Lee, S. Barlow, S. Thayumanavan, S. Marder, N. Armstrong, J. Bredas, J. Phys. Chem. A 105 (2001) 5206.

[16] M. Malagoli, M. Manoharan, B. Kippelen, J.L. Bredas, Chem. Phys. Lett. 354 (2002) 283.

[17] B. Lin, C. Cheng, Z. Lao, J. Phys. Chem. A 107 (2003) 5241.

[18] A. Kennedy, W. Smith, D. Tackley, W. David, K. Shankland, B. Brown, S. Teat, J. Mater. Chem. 12 (2002) 168.

[19] Z. Zhang, E. Burkholder, J. Zubieta, Acta Cryst. C60 (2004) o452.

[20] K. Shankland, A.R. Kennedy, W.I.F. David, J. Mater. Chem. 15 (2005) 4838.

[21] K. Schmidt-Rohr, H.W. Spiess, Multidimensional Solid-State NMR and Polymers, Academic Press, London, 1994.

[22] K. Schmidt-Rohr, W. Hu, N. Zumbulyadis, Science 280 (1998) 714.

[23] H. Kaji, K. Schmidt-Rohr, Macromolecules 33 (2000) 5169.

[24] H. Kaji, K. Schmidt-Rohr, Macromolecules 34 (2001) 7368.

[25] H. Kaji, K. Schmidt-Rohr, Macromolecules 35 (2002) 7993.

[26] H. Kaji, T. Tai, F. Horii, Macromolecules 34 (2001) 6318.

[27] H. Kaji, K. Fuke, F. Horii, Macromolecules 36 (2003) 4414.

[28] R.A. Marcus, J. Chem. Phys. 24 (1956) 966.

[29] R.A. Marcus, N. Sutin, Biochim. Biophys. Acta 811 (1985) 265.

[30] H. Bässler, Phys. Stat. Sol. B 175 (1993) 15.

[31] J. Cornil, D. Beljonne, J.P. Calbert, J.L. Brédas, Adv. Mater. 13 (2001) 1053.

[32] S. Thayumanavan, S. Barlow, S.R. Marder, Chem. Mater. 9 (1997) 3231.

[33] G.C. Levy, R.L. Lichter, Nitrogen-15 Nuclear Magnetic Spectroscopy, Wiley, New York, 1979.

[34] E.Y. Chekmenev, Q.W. Zhang, K.W. Waddell, M.S. Mashuta, R.J. Wittebort, J. Am. Chem. Soc. 126 (2004) 379.

[35] A.D. Becke, Phys. Rev. A 38 (1988) 3098.

[36] A.D. Becke, J. Chem. Phys. 98 (1993) 1372.

[37] A.D. Becke, J. Chem. Phys. 98 (1993) 5648.

[38] C.T. Lee, W.T. Yang, R.G. Parr, Phys. Rev. B 37 (1988) 785.

[39] R. Ditchfield, W.J. Hehre, J.A. Pople, J. Chem. Phys. 54 (1971) 724.

[40] W.J. Hehre, R. Ditchfield, J.A. Pople, J. Chem. Phys. 56 (1972) 2257.

[41] P.C. Hariharan, J.A. Pople, Mol. Phys. 27 (1974) 209.

[42] M.S. Gordon, Chem. Phys. Lett. 76 (1980) 163.

[43] P.C. Hariharan, J.A. Pople, Theoret. Chim. Acta 28 (1973) 213.

[44] R. Ditchfield, Mol. Phys. 27 (1974) 789.

[45] M.J. Frisch et al., GAUSSIAN 98 (Revision A.11), Gaussian, Pittsburgh, PA, 2001.

[46] T.M. Dnucan, A Compilation of Chemical Shift Anisotropies, The Farragut Press, Chicago, 1990.

[47] T.W.G. Solomons, C.B. Fryhle, Organic Chemistry, 7th ed., Wiley, New York, 2000.

[48] A.E. Reed, L.A. Curtiss, F. Weinhold, Chem. Rev. 88 (1988) 899.

Chapter 3

Conformational Dependence of Diamagnetic and Paramagnetic ^{15}N NMR Shieldings and Charge-Transport Property of TPD

3.1. Introduction

In Chapter 2, the molecular structure of amorphous *N,N'*-diphenyl-*N,N'*-di(*m*-tolyl)benzidine (TPD) (see Fig. 3.1) was investigated, revealing that the planarity and conformation around the nitrogen atom strongly affect the ^{15}N chemical shift anisotropy (CSA). The planarity was expressed as the summation of the three bond angles around the nitrogen atom, θ_1 (= ∠C4NC5) + θ_2 (= ∠C4NC9) + θ_3 (= ∠C5NC9), and the conformation around the nitrogen was represented by the torsion angles, α (= ∠C3C4NC5), β (= ∠C6C5NC4), and γ (= ∠C10C9NC4). The difference between the principal values of ^{15}N chemical shift tensor, $\sigma_{11} - \sigma_{33}$, referred as CSA span was as narrow as 15 ppm for the DFT-optimized TPD. This calculated CSA span agreed well with the experimental CSA span for the amorphous state. The quantum chemical calculations revealed that the CSA span increases to more than 100 ppm, depending on the planarity and the conformation. Because NMR parameters, including the CSA span, reflect the electronic structure around the nucleus, the results indicates that the molecular structure of TPD strongly affects the electronic structure around the nitrogen, which has large contribution to HOMO and therefore closely relate to the hole-transport property [1,2]. In Chapter 2, it was shown that the nitrogen atom is $sp^{2.0}$ and $sp^{2.8}$ hybridized in the planar ($\theta_1 + \theta_2 + \theta_3 = 360^o$) and pyramidal ($\theta_1 + \theta_2 + \theta_3 = 310^o$) structures of TPD, respectively. It was suggested that the planar structure is more favorable for hole transports than the pyramidal structure, because the sp^2 hybridized nitrogen atom and the shorter intermolecular distance for the planar structure are

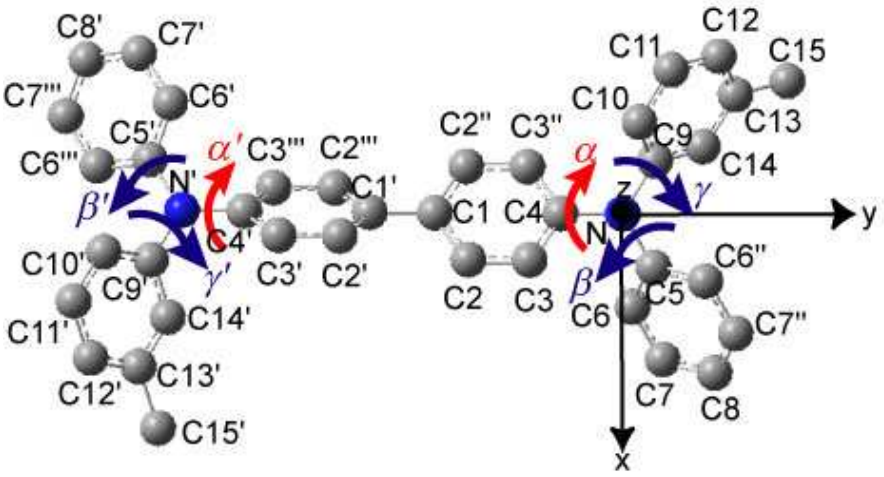

Fig. 3.1. The chemical structure of TPD. The α, β, and γ indicate the torsion angles, ∠C3C4NC5, ∠C6C5NC4, and ∠C10C9NC4, respectively. The xyz axes in the Cartesian coordinate system are also shown. The z-axis is vertical to the nitrogen-centered plane, the y-axis is parallel to the N-C4 bond, and the x-axis is perpendicular to the z- and y-axes.

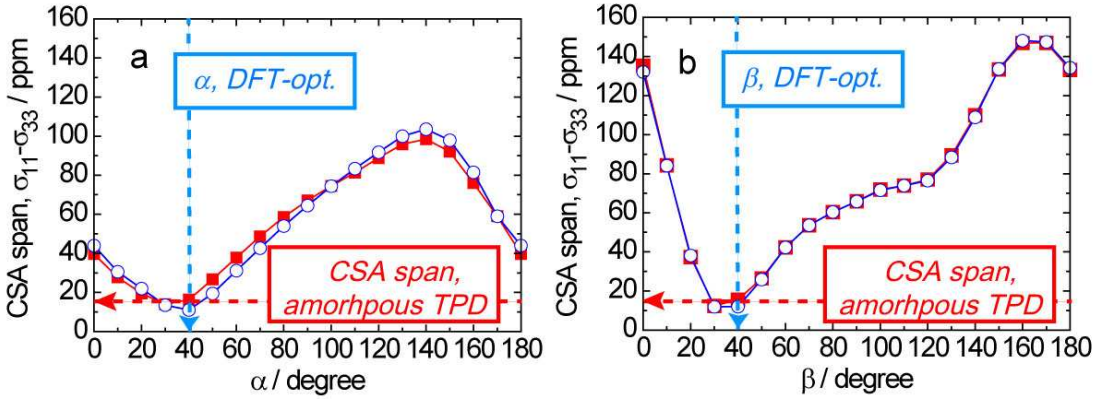

Fig. 3.2. The ^{15}N CSA span, $\sigma_{11} - \sigma_{33}$, of TPD as a function of torsion angles, (a) α and (b) β, under the assumption of β = γ. All the other parameters are fixed to the optimized values. The open circles and filled squares represent the values for the right and left nitrogen nuclei, respectively. The calculations were performed at the DFT B3LYP/6-31G(d) level.

advantageous for the intermolecular overlaps of HOMOs, which are crucial for intermolecular charge transports by hopping mechanism.

It can be considered that the torsion angles, α, β, and γ, also affect the electronic structure and the hole-transport property, based on the torsion angles dependences of the ^{15}N CSA span as described in Chapter 2 (the dependences are shown in Fig. 3.2). The aims in this chapter are to clarify the origins of the conformational dependence of the ^{15}N CSA span of TPD and to show the relationship between the conformation and charge-transport property. For the analyses of the CSA span, the NMR shielding constants are divided into the diamagnetic shielding and paramagnetic deshielding terms, according to Ramsey's theory [3]. The diamagnetic and paramagnetic terms, $\sigma_{tu}'^{dia}$ and $\sigma_{tu}'^{para}$, are expressed by Eqs. 3.1 and 3.2, respectively [3-9].

$$\sigma'^{dia}_{tu} = \frac{e^2\mu_0}{8\pi m^2} < 0 | \sum_j (\frac{1}{r_j} - \frac{r_{jt} r_{ju}}{r_j^3}) | 0 > \tag{3.1}$$

$$\sigma'^{para}_{tu} = \frac{e^2\mu_0}{8\pi m^2} \sum_n \frac{< 0 | \sum_j L_{jt} | n >< n | \sum_j \frac{L_{ju}}{r_j^3} | 0 >}{E_0 - E_n} \tag{3.2}$$

Here, t, u = (x, y, z), r_j is the distance of the jth electron from the nucleus, and |0> and |n> denote the ground and the nth excited states, respectively. L_{jt} is the t component of the angular momentum of the jth electron. The parameters of e, m, and μ_0 are the elementary charge, electron mass, and vacuum permeability, respectively. It can be seen from Eq. 3.1 that the diamagnetic term relates to the spherical electron density in the ground state, because it is described by the distance of the electrons from the nucleus. From Eq. 3.2, the paramagnetic term is shown to relate to the electron mixing between the ground and excited states, and inversely proportional to the energy difference between the states. The electron mixing can be

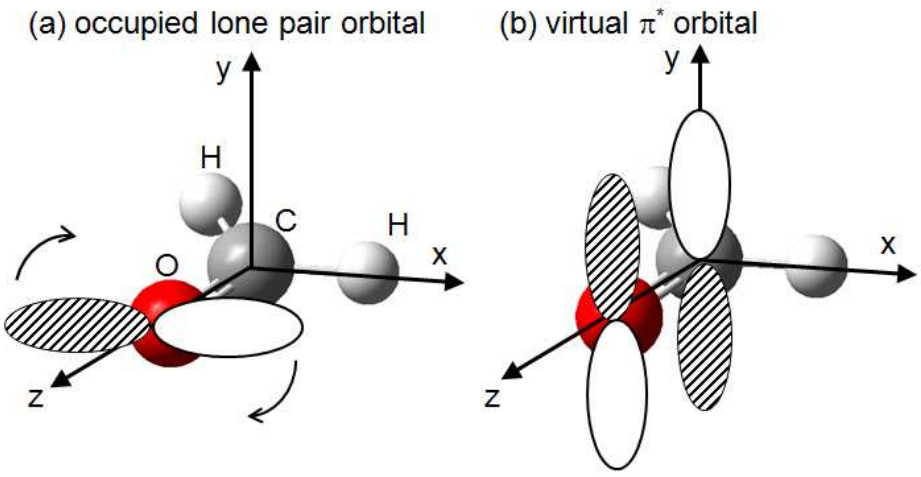

Fig. 3.3. The lone pair orbital (a) and π^* orbital (b) of a formaldehyde molecule [6]. The 90° rotated occupied lone pair orbital about the z-axis overlap well with the virtual π^* orbital.

visualized by the rotated occupied orbital about the *t*-axis, when the magnetic field is applied along the *t* direction [5-9]. If the rotated orbital has good overlap with the virtual orbital, a local paramagnetic field is produced. For example, in the case of formaldehyde shown in Fig. 3.3, the 90° rotation of the about the z-axis is considered for the lone pair orbital when the magnetic field is applied along the z direction. The rotated lone pair orbital overlaps with the virtual π^* orbital to produce significant paramagnetic deshielding for the oxygen nucleus [6]. Through the analyses of the diamagnetic and paramagnetic terms of the ^{15}N NMR shieldings of TPD in different conformation, the conformational dependence of the electronic structure of TPD is investigated, considering the relationship with the charge-transport property.

3.2. Computational Section

For the DFT-optimized geometry of a TPD molecule described in Chapter 2, the diamagnetic and paramagnetic ^{15}N NMR shielding tensor components, σ'_{xx}, σ'_{yy}, and σ'_{zz}, which respectively correspond to the magnetic shieldings along the x, y, and z directions, were

calculated. As shown in Fig. 3.1, the z-axis is vertical to the nitrogen-centered plane, the y-axis is parallel to the N-C4 bond, and the x-axis is perpendicular to the z- and y-axes. Similarly in Chapter 2, the calculations were carried out varying the torsion angle, α or β, from 0^o to 180^o with the interval of 10^o. The torsion angles of 0^o and 180^o correspond to the conformation, for which the nitrogen-centered plane and the rotated benzene ring are in the same plane. The calculations were performed assuming that the β and γ values are equivalent due to the structural similarity. The other parameters are fixed to the DFT-optimized values. In order to analyze the origins of the conformational dependences of the tensor components based on Eqs. 3.1 and 3.2, the occupied and virtual MOs were investigated for the conformers with different α and β values. The calculations were performed at HF/STO-3G level, comparing the results obtained by B3LYP/6-31G(d) calculations [10-13]. This is because the physical meaning of DFT-calculated MOs is uncertain [14-17], although it gave reasonable results for the NMR parameters in Chapter 2. The reason for the selection of STO-3G basis set is the constitutive understanding of the NMR parameters; although larger basis sets are suitable for the quantitative NMR analyses, diffused electrons in the large basis sets would make the essential understanding of the NMR phenomena complicated and obscure.

For the detailed investigations of NMR shiledings, natural chemical shielding (NCS) analyses [4,6] combined with the natural bond orbital (NBO) [18-21] calculations were also performed. The NBO is the orbital which is constructed to optimally describe the electron density between the two centers (Lewis bond orbital) or on single center (lone pair). All of the bonding σ and π orbitals and the non-bonding lone pair orbitals in a TPD molecule can be described by NBOs. The NCS analyses divide the NMR shieldings into the contributions from each natural localized MO (NLMO) [22], which consists of a parent NBO and slightly occupied anti-bonding orbitals to have full occupancy (2*e*). All the calculations were performed with the Gaussian 09

program [23].

3.3. Results and Discussion

3.3.1. Torsion Angle α Dependence of ^{15}N NMR Shielding

Fig. 3.4a show the torsion angle α dependence of the ^{15}N NMR shielding tensor components of TPD, calculated by B3LYP/6-31G(d) levels. The shielding tensor components, σ'_{xx}, σ'_{yy}, and σ'_{zz}, are shown. It is suggested from Fig. 3.4a that the σ'_{xx} and σ'_{zz} values strongly depend on the torsion angle α, while the σ'_{yy} values are almost plateau irrespective of α value. The difference between the maximum and minimum values for the σ'_{xx}, σ'_{yy}, and σ'_{zz} components are 78, 11, and 36 ppm, respectively. Fig. 3.4a indicates that the difference between the x and z components qualitatively correlate with the torsion angle α dependence of the ^{15}N CSA span in Fig. 3.2a. Note that the dependence of the σ'_{xx} value in Fig 3.4a is almost symmetrical with respect to $\alpha = 90^{o}$, while that of the σ'_{zz} value is not; the maximum and minimum values for the σ'_{zz} value occur at $\alpha = 140^{o}$ and 40^{o}, respectively. As a consequence, torsion angle α dependence of the ^{15}N CSA span is not symmetrical with respect to $\alpha = 90^{o}$.

For the detailed investigations, the diamagnetic and paramagnetic terms of the shielding tensor components are separately shown in Figs. 3.4b and 3.4c, respectively. It is clear that the paramagnetic terms governs the α dependence of the ^{15}N shielding tensor components; the difference between the maximum and minimum values of the diamagnetic components are less than 15 ppm for all the tensor components, while those of the paramagnetic xx, yy, and zz components are 68, 11, 35 ppm, respectively. It is found that the paramagnetic values of σ'_{xx} and σ'_{zz} are dominant for the torsion angle α dependence of ^{15}N CSA span.

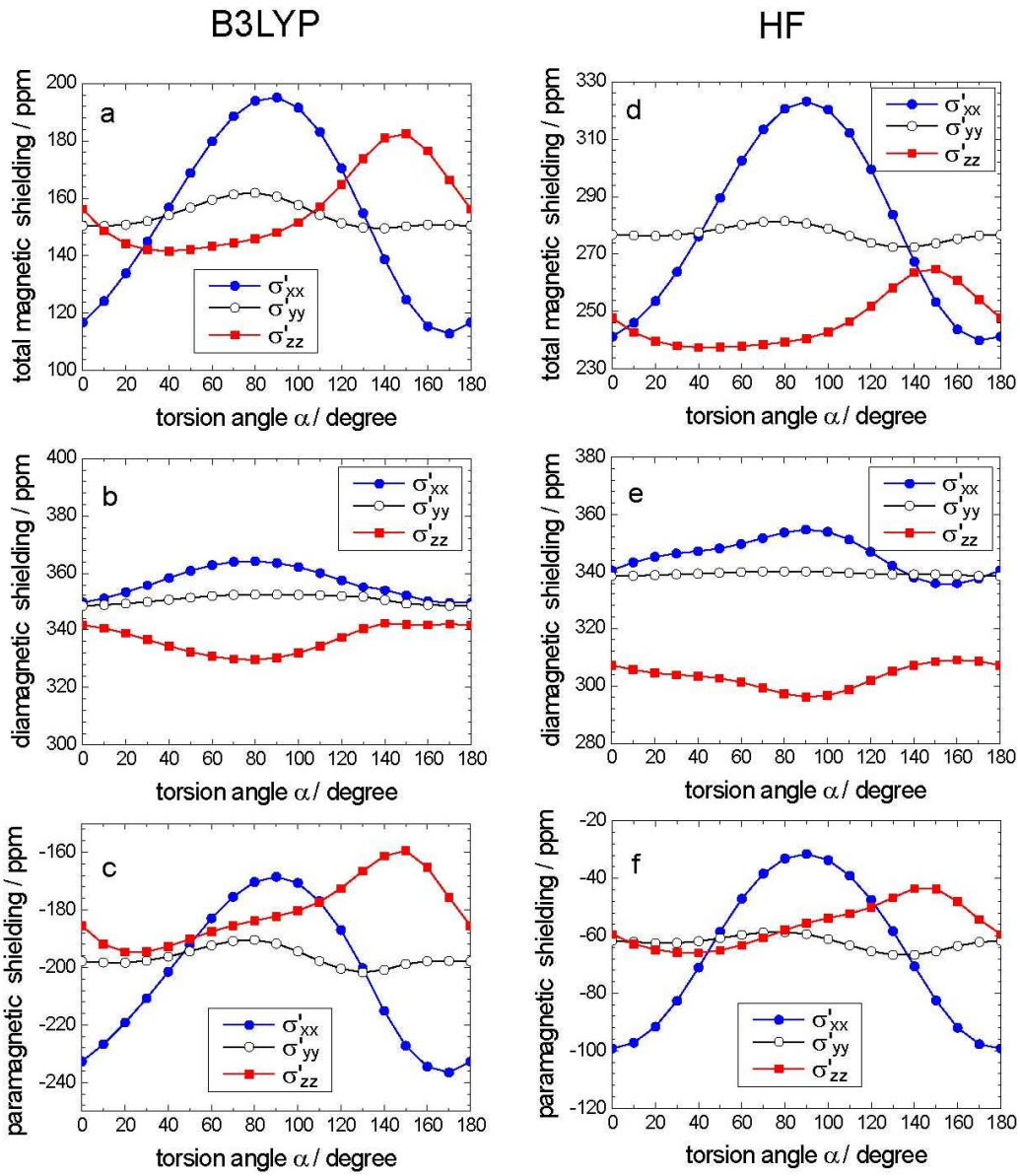

Fig. 3.4. Torsion angle α dependence of the ^{15}N NMR shielding tensor components, σ'_{xx} (•), σ'_{yy} (○), and σ'_{zz} (■), of TPD. The other structural parameters are fixed to the optimized values. The ^{15}N NMR total shieldings, diamagnetic shieldings, and paramagnetic shieldings calculated at B3LYP/6-31G(d) levels are respectively shown in (a), (b), and (c). And those calculated at HF/STO-3G level are shown in (d), (e), and (f), respectively.

The results obtained by HF/STO-3G calculations are shown in Figs. 3.4d-3.4f. It is suggested that the torsion angle α dependence of the total NMR shielding is also dominated by the paramagnetic term, similarly to the B3LYP/6-31G(d) calculations. The differences between the maximum and minimum values of the paramagnetic xx, yy, and zz components are 67, 8, 22 ppm, respectively. The most extreme paramagnetic values are obtained at $\alpha = 0^{o}$ (-99 ppm), 90^{o} (-32 ppm), and 180^{o} (-99 ppm) for σ'_{xx} and $\alpha = 30 - 40^{o}$ (-66 ppm) and $140 - 150^{o}$ (-44 ppm) for σ'_{zz}. Although the absolute values are different between the results of the B3LYP/6-31G(d) and HF/STO-3G calculations, the tendency of the torsion angle α dependence of each tensor components is qualitatively comparable with each other, especially for the paramagnetic components. Hereafter, HF/STO-3G level is used to analyze the torsion angle α dependence of the paramagnetic NMR shieldings to understand the constitutive origins of the torsion angle α dependence of the ^{15}N CSA span.

3.3.2. NCS Analysis for the Torsion Angle α Dependence of the Paramagnetic NMR Deshielding

In order to comprehend which orbitals yield the torsion angle α dependence of the paramagnetic σ'_{xx} and σ'_{zz} values, NCS analyses were performed for TPD with different α value. In the framework of NCS analysis, the shielding tensor components are divided into the contribution from each NLMO. Although information on virtual MOs cannot be obtained from the analysis, it is a powerful method to investigate the origins of the NMR shielding [4,6,24-26]. There are 137 NLMOs for TPD and the nitrogen-related NLMOs correspond to the σ orbitals of the N-C4, N-C5, and N-C9 bonds and the lone pair orbital of the nitrogen. In Fig. 3.5a, the paramagnetic σ'_{xx} value is divided into the contributions from the nitrogen-related NLMOs and the other 133 NLMOs. It is clear from this figure that the nitrogen-related

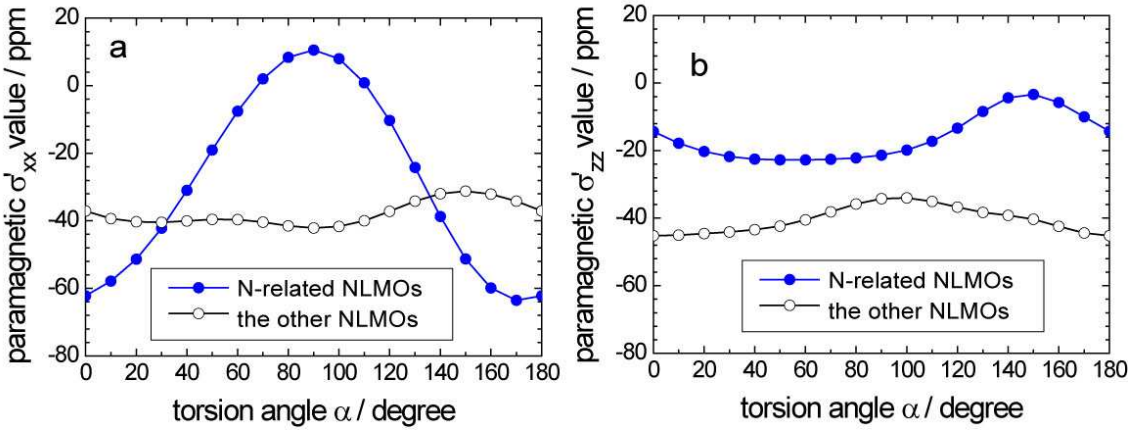

Fig. 3.5. Torsion angle α dependence of the ^{15}N paramagnetic shielding components, (a) σ'_{xx} and (b) σ'_{zz}, of TPD, divided into the contributions from the nitrogen-related NLMOs (•) and the other NLMOs (○). The nitrogen-related NLMOs correspond to the lone pair orbital and the σ orbitals of the three N-C bonds around the nitrogen. The other NLMOs indicate total contribution from the remaining 133 NLMOs. The calculations were performed at HF/STO-3G level.

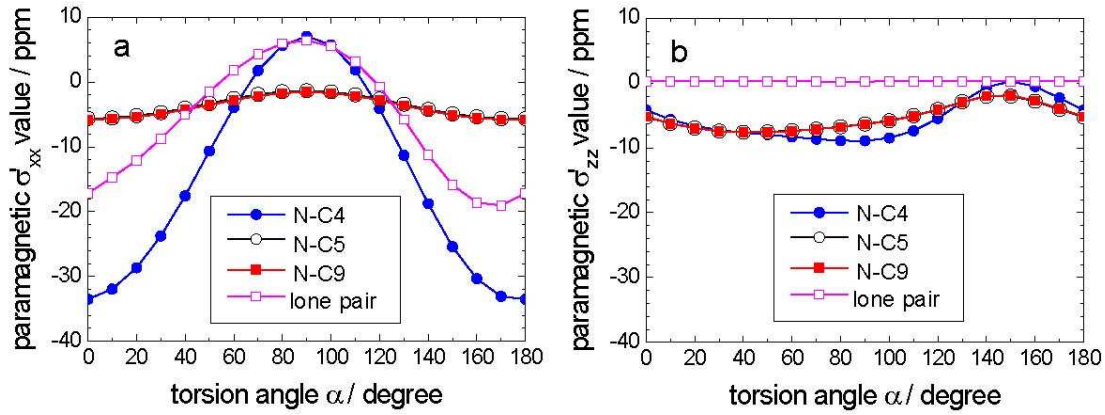

Fig. 3.6. Torsion angle α dependence of the ^{15}N paramagnetic shielding components, (a) σ'_{xx} and (b) σ'_{zz}, of TPD, divided into the contributions from the lone pair orbital (•) and the σ orbitals of the three N-C bonds around the nitrogen, N-C4 (○), N-C5 (■), and N-C9(□). The calculations were performed at HF/STO-3G level.

NLMOs are dominant for the torsion angle α dependence of the paramagnetic σ'_{xx} value. This indicates that the electronic structure around the nitrogen nucleus in the y-z plane is affected by the rotation of the N-C4 bond. The other 133 NLMOs hardly affect the torsion angle α dependence of the ^{15}N CSA; the contribution from each NLMO is small, in the range of -5–5 ppm. The shielding contributions from the nitrogen-related NLMOs are further divided into the contribution from each NLMO as shown in Fig. 3.6a. It is revealed that the torsion angle α dependence of the paramagnetic σ'_{xx} values are dominantly caused by the σ orbital of the N-C4 bond (-34 – 7 ppm) and the nitrogen lone pair orbital (-19 – 6 ppm), while the contributions from the other σ orbitals are small (-6 – -1 ppm). The contributions from these orbitals can be understood as follows. The paramagnetic NMR deshielding along the x direction is caused by the electronic mixing of the rotated occupied orbital around the x-axis and the virtual orbital, according to Eq. 3.2. Therefore, for the paramagnetic σ'_{xx} value, the relevant occupied and virtual orbitals should be in the y-z plane. The possible pairs of orbitals are (1) the σ and π^* orbitals of the N-C4 bond and (2) the nitrogen lone pair orbital and σ^* orbital of the N-C4 bond. For both of the pairs, the 90^o rotated occupied orbital around the x-axis can overlap with the virtual orbital as shown in Fig. 3.7 (the stereoscopic π^* orbital is not shown because the orbital is not directly recognized in the analysis as described later). The large contributions from these occupied orbitals are corroborated by the NCS result in Fig. 3.6a.

Fig. 3.5b shows the paramagnetic σ'_{zz} value divided into the contributions from the nitrogen-related NLMOs and the other NLMOs. It is found that the nitrogen-related NLMOs are dominant for the torsion angle α dependence of the paramagnetic σ'_{zz} value, indicating that the electronic structures around the nitrogen nucleus in the x-y planes are affected by the rotation of the N-C4 bond. The shielding contributions from the nitrogen-related NLMOs are further divided into the contribution from each NLMO as shown in Fig. 3.6b. It is revealed

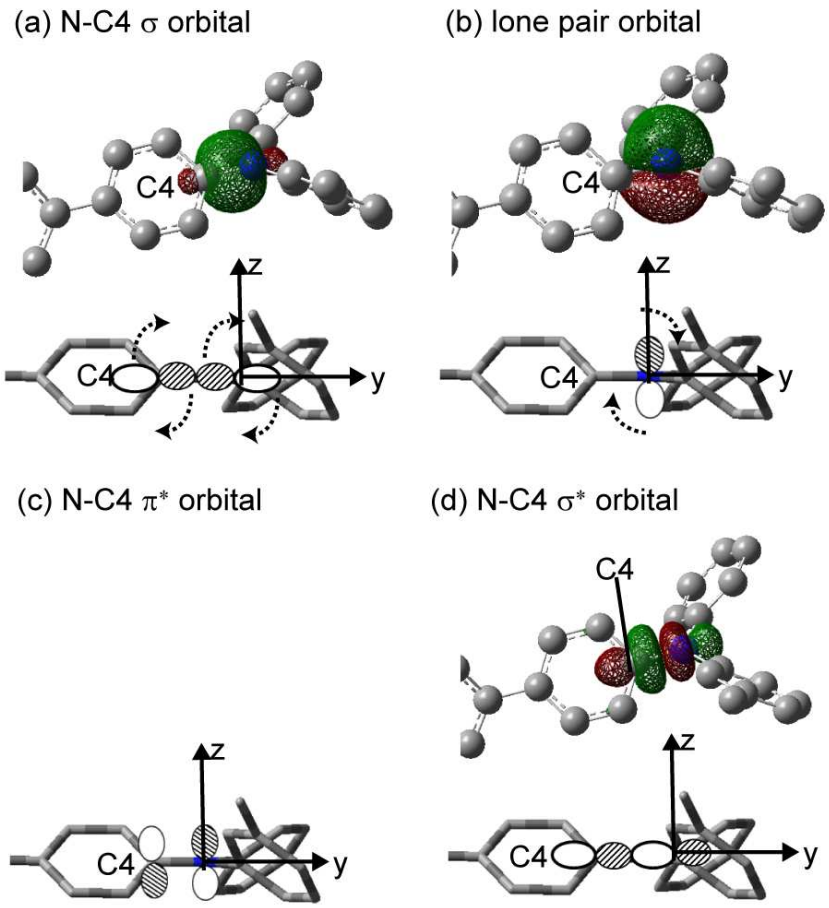

Fig. 3.7. NLMOs which contribute to the ^{15}N paramagnetic σ'_{xx} deshielding of TPD; the σ orbital of the N-C4 bond (a), lone pair orbital (b), π^* orbital of the N-C4 bond (c), and σ^* orbital of the N-C4 bond (d). Both the stereoscopic images obtained by HF/STO-3G calculations and schematic cross-sections in the y-z plane are shown. The isosurface value for the stereoscopic images is 0.05 a.u. The occupied orbitals rotate in the y-z plane as indicated by dotted arrowed lines when the magnetic field is applied along the x direction. The stereoscopic image of the π^* orbital of the N-C4 bond is not shown, because the orbital is not directly recognized in the analyses.

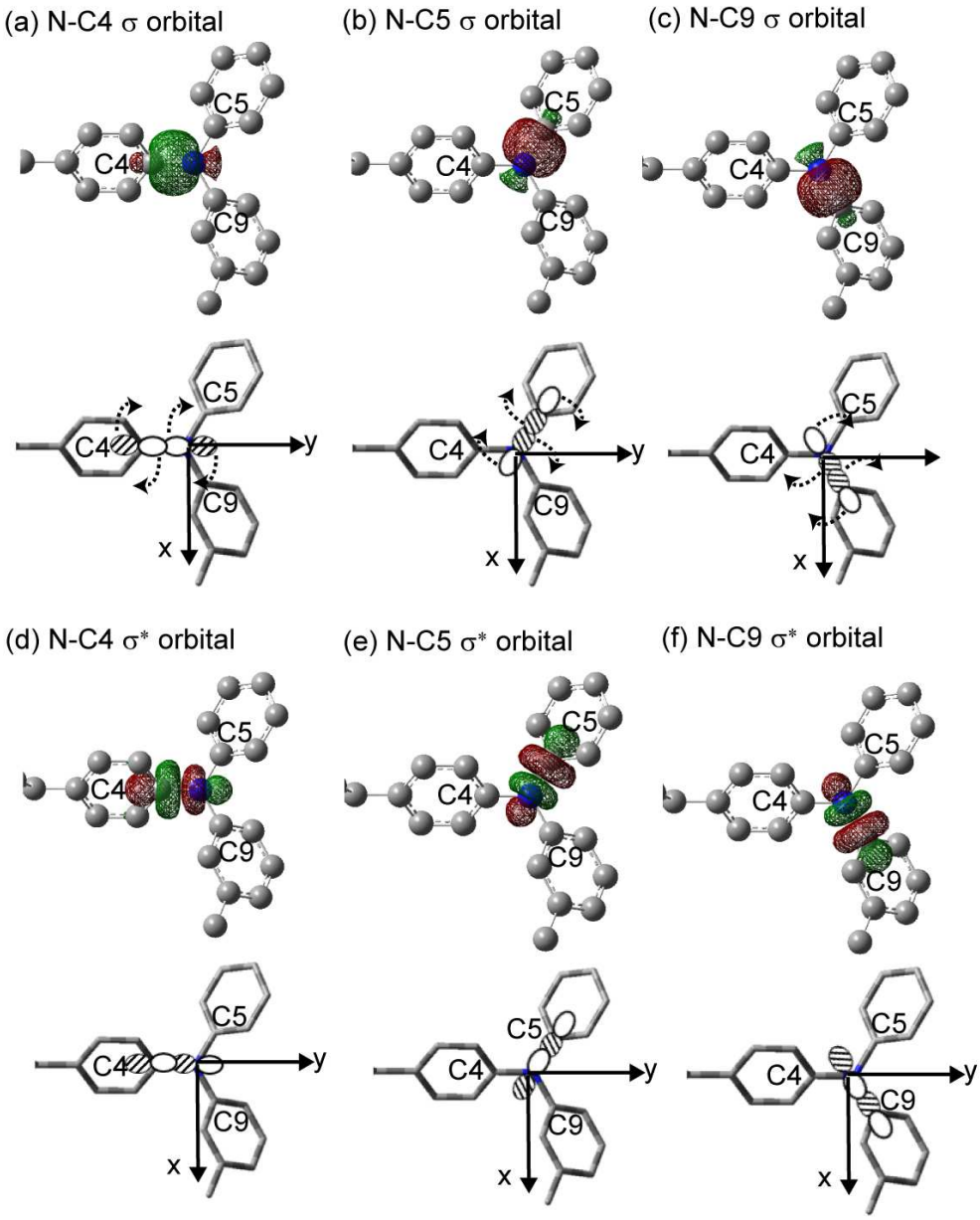

Fig. 3.8. NLMOs which contribute to the ^{15}N paramagnetic σ'_{zz} deshielding of TPD; the σ and σ^* orbitals of the N-C4, N-C5, N-C9 bonds. Both the stereoscopic images obtained by HF/STO-3G calculations and schematic cross-sections in the x-y plane are shown. The isosurface value for the stereoscopic images is 0.05 a.u. The occupied orbitals rotate in the x-y plane as indicated by dotted arrowed lines when the magnetic field is applied along the z direction.

that the σ'_{zz} value is subjected by the σ orbitals of the three N-C bonds, although the absolute value of each contribution is small (-9 – 0 ppm). The contribution of the lone pair orbital is negligible (0 ppm irrespective of α value). It can be considered that the paramagnetic σ'_{zz} value is produced by the electron mixing between the σ and σ^* orbitals of the N-C4, N-C5, and N-C9 bonds, which are in the x-y plane (see Fig. 3.8). For example, the rotated σ orbital of the N-C4 bond can overlap with the σ^* orbitals of the N-C5 and N-C9 bonds.

3.3.3. Origins of the Torsion Angle α Dependence of the Paramagnetic NMR Deshielding

Here, the origins of the torsion angle α dependence of the paramagnetic σ'_{xx} and σ'_{zz} values are investigated. To understand the origins of the torsion angle α dependence of the paramagnetic tensor components, three possibilities are considered based on Eq. 3.2. The first possibility is the energy difference between the occupied and virtual orbitals, because the paramagnetic deshielding value is inversely proportional to the energy difference. Fig. 3.9 shows the orbital energies of the nitrogen-related occupied and virtual NBOs. It is suggested from Fig. 3.9 that the energies are almost stable irrespective of the α value, and thus, the energy difference is not the cause of the torsion angle α dependence of the ^{15}N NMR shielding. However, it can be explained from Fig. 3.9 why the paramagnetic σ'_{zz} contributions from the σ orbitals of the N-C bonds are smaller than the paramagnetic σ'_{xx} contributions from the lone pari orbital. From Fig. 3.9, the energy difference between the σ and σ^* orbitals is as large as 42-43 eV. The smaller energy difference between the lone pair and σ^* orbitals, 27-28 eV, make it possible to produce larger paramagnetic σ'_{xx} contribution. A remaining question is that, in Fig. 3.9, the NBO analyses did not output orbitals corresponding to the π^* orbital between the N-C bonds, which would overlap with the 90^o rotated lone pair orbital to produce the σ'_{xx} deshielding. This is because the nitrogen p_z orbital is recognized as the nonbonding lone pair

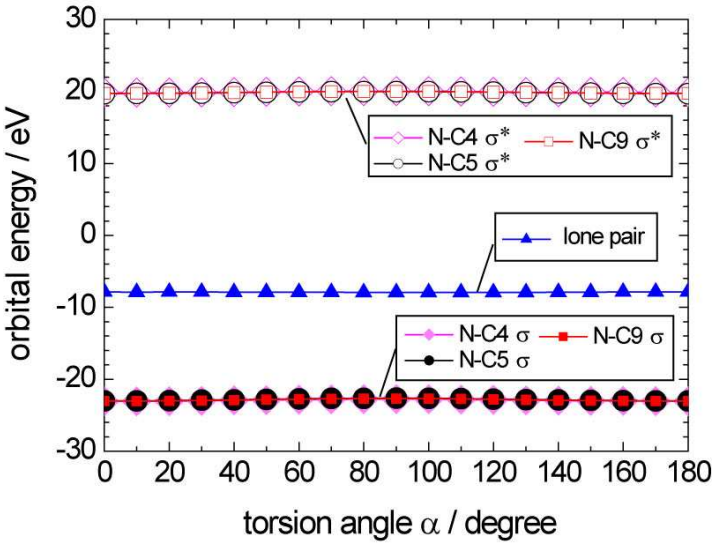

Fig. 3.9. Torsion angle α dependence of the orbital energyies of the nitrogen-related occupied NBOs (σ orbitals of the N-C4 (♦), N-C5 (●), N-C9 (■) bonds and lone pair orbital (▲)) and virtual NBOs (σ^* orbitals of the N-C4 (◊), N-C5 (○), and N-C9 (□) bonds). The calculations were performed at HF/STO-3G level.

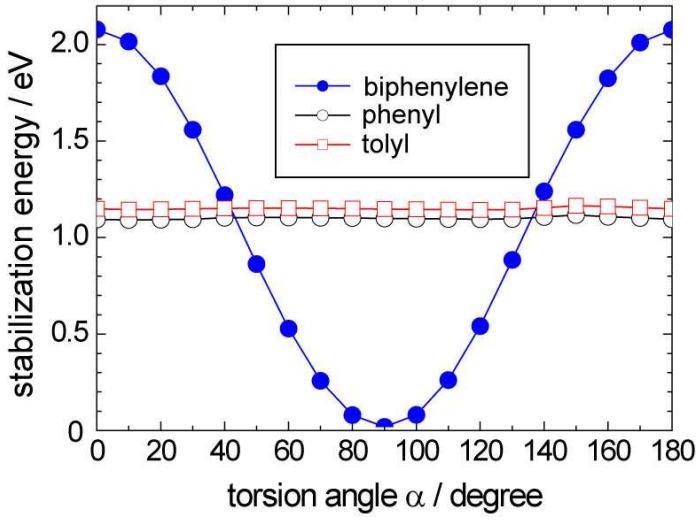

Fig. 3.10. Torsion angle α dependence of the stabilization energy of the lone pair orbital by the interaction with the π orbitals of the biphenylene (•), phenyl (○), and tolyl (□) rings, obtained by HF/STO-3G calculations.

orbital rather than the π-bonding orbital in the analyses. Instead, the π-bonding characteristic of the N-C bond is expressed by the stabilization energy of the lone pair orbital by the interaction with the π orbitals of the benzene rings. The larger the stabilization energy is, the stronger the π bonding and π^* anti-bonding characteristics are. Fig. 3.10 shows the stabilization energies of the lone pair orbital cause by the interaction with the π orbitals of the biphenylene, phenyl, and tolyl rings. It is clear that the interaction between the lone pair orbital and the biphenylene π orbital is the strongest for the conformers with $\alpha = 0^o$, 180^o and that the weakest interaction is found for the conformer with $\alpha = 90^o$. The result indicates that the π bonding and π^* anti-bonding characteristics of the N-C4 bond are the most significant when the α value is 0^o or 180^o and insignificant when $\alpha = 90^o$. The tendency is consistent with the torsion angle α dependence of the paramagnetic σ'_{xx} value. It can be considered that the σ and π^* orbitals and the π and σ^* orbitals of the N-C4 bond strongly interact with each other to produce the paramagnetic σ'_{xx} deshielding when the benzene ring of the biphenylene moiety and the nitrogen-centered plane are parallel to each other.

The second possibility of the torsion angle α dependences of the paramagnetic ^{15}N NMR deshieldings is the geometrical change of the NBOs, which is quantified by the orbital coefficients. If the orbital coefficients vary with the torsion angle α, the overlap between the occupied and virtual NBOs which produce the paramagnetic deshielding is also changed, based on Eq. 3.2. The orbital coefficients of the nitrogen-related occupied and virtual NBOs are represented in Table 3.1 for some conformers. In Table 3.1, only the coefficients for *p* orbitals are shown, because *s* orbitals do not contribute to the paramagnetic deshielding due to the angular momenta of 0 (see Eq. 3.2). From Table 3.1, it is clear that the coefficients are almost independent of the α value. Therefore, torsion angle α dependence of the paramagnetic ^{15}N NMR deshieldings cannot be explained by the orbital coefficients.

The last possible cause for the torsion angle dependence is the interaction between the occupied and the virtual NBOs. Fig. 3.11 shows the interaction energy between the σ and σ* orbitals of the N-C bonds. No other interactions were detected between the nitrogen-related orbitals. It is suggested from Fig. 3.11b that the summation of the interaction energies closely relate with the torsion angle α dependence of the paramagnetic σ'_{zz} value in Figs. 3.4f, 3.5b, and 3.6b. The strong interaction in the x-y plane is considered to produce the significant paramagnetic deshielding along the z-axis. This is further confirmed investigating the torsion angle β dependence of the paramagnetic σ'_{zz} value.

Table 3.1. Orbital coefficients of the nitrogen-related NBOs (σ and σ* orbital of the N-C4, N-C5, and N-C9 bonds and lone pair orbitals) for the conformer with α = 0, 40, 90, 140, and 180°. The other structural parameters are fixed to the optimized values. The calculations were carried out at HF/STO-3G level.

α / degree	N-C4 σ orbital			N-C5 σ orbital			N-C9 σ orbital			lone pair orbital		
	p_x	p_y	p_z	p_x	p_y	p_z	p_x	p_y	p_z	p_x	p_y	p_z
0	0.00	-0.62	0.00	0.54	0.31	0.00	-0.54	0.31	0.00	0.00	0.00	-1.00
40	0.00	-0.62	0.00	0.54	0.31	0.00	-0.54	0.31	0.00	0.00	0.00	-1.00
90	0.00	-0.62	0.00	0.54	0.31	0.00	-0.54	0.31	0.00	0.00	0.00	-1.00
140	0.00	-0.62	0.00	0.54	0.31	0.00	-0.54	0.31	0.00	-0.01	0.00	-1.00
180	0.00	-0.62	0.00	0.54	0.31	0.00	-0.54	0.31	0.00	0.00	0.00	-1.00

α / degree	N-C4 σ* orbital			N-C5 σ* orbital			N-C9 σ* orbital		
	p_x	p_y	p_z	p_x	p_y	p_z	p_x	p_y	p_z
0	0.00	0.52	0.00	-0.46	-0.26	0.00	0.46	-0.26	0.00
40	0.00	0.53	0.00	-0.46	-0.26	0.00	0.46	-0.26	0.00
90	0.00	0.53	0.00	-0.46	-0.26	0.00	0.46	-0.26	0.00
140	0.00	0.53	0.00	-0.46	-0.26	0.00	0.46	-0.26	0.00
180	0.00	0.52	0.00	-0.46	-0.26	0.00	0.46	-0.26	0.00

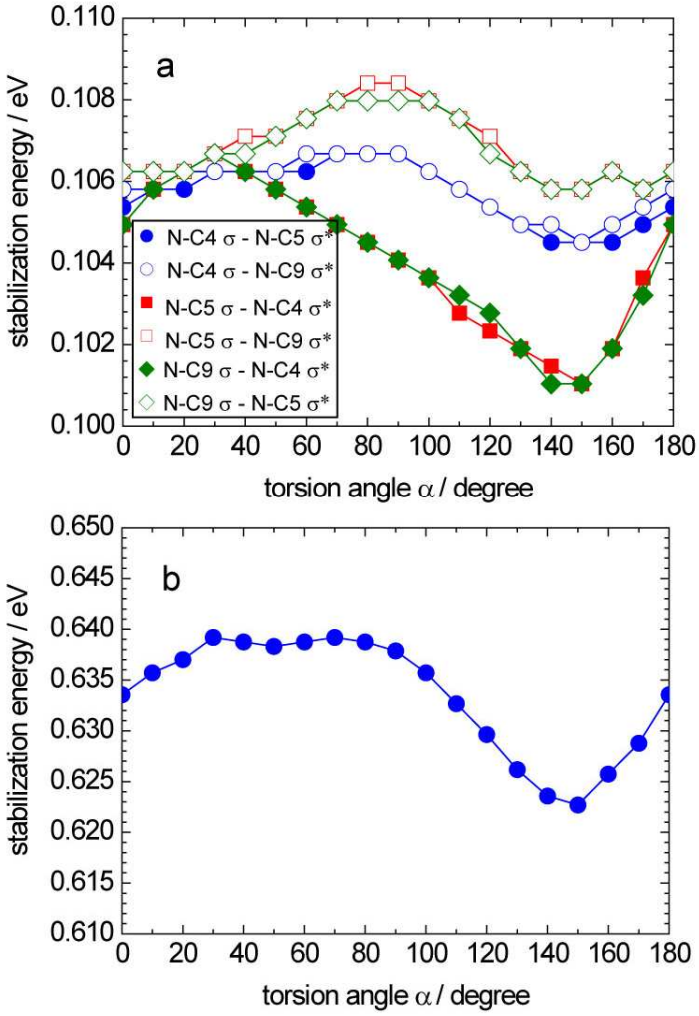

Fig. 3.11. Torsion angle α dependence of the stabilization energy for the σ orbitals of the N-C4 (●, ○), N-C5 (■, □), and N-C9 (♦, ◊) bonds by the interaction with the σ^* orbitals. The stabilization energy for each interaction is shown in (a) and the total stabilization energy is shown in (b). The calculations were performed at the level of HF/STO-3G.

3.3.4. Torsion Angle β Dependence of ^{15}N NMR Shielding

Fig. 3.12 show the torsion angle β dependence of the ^{15}N NMR shielding tensor components of TPD, calculated by B3LYP/6-31G(d) and HF/STO-3G levels. The total, diamagnetic, and paramagnetic shielding tensor components, σ'_{xx}, σ'_{yy}, and σ'_{zz}, are shown. As in the case of the torsion angle α dependences in Fig. 3.4, the torsion angle β dependences obtained by B3LYP/6-31G(d) and HF/STO-3G calculations are qualitatively comparable, although the absolute values are different from each other. It is indicated from Figs. 3.12a and 3.12d that the difference between the y and z components correlate with the torsion angle β dependence of the ^{15}N CSA span. Focusing on the result by HF/STO-3G calculations in Figs. 3.12d–3.12f, the torsion angle β dependences of the ^{15}N shielding tensor components are subjected by the paramagnetic terms; the difference between the maximum and minimum values for the paramagnetic σ'_{xx}, σ'_{yy}, and σ'_{zz} components are 41, 107, and 48 ppm, respectively, while the those for the diamagnetic components are less than 21 ppm. Considering these results, the torsion angle β dependences of the ^{15}N CSA span of TPD is dominated by the paramagnetic σ'_{yy} and σ'_{zz} components. Note that the torsion angle β dependence of the paramagnetic σ'_{yy} value is symmetrical with respect to $\beta = 90^{o}$, while that of the σ'_{zz} value is not; the extreme deshielding values for the paramagnetic σ'_{zz} component appear at $\beta = 30 - 40^{o}$ (-67 ppm) and $\beta = 0, 180^{o}$ (-19 ppm), respectively. This makes the torsion angle β dependence of the ^{15}N CSA span asymmetrical with respect to $\beta = 90^{o}$ as shown in Fig. 3.2b.

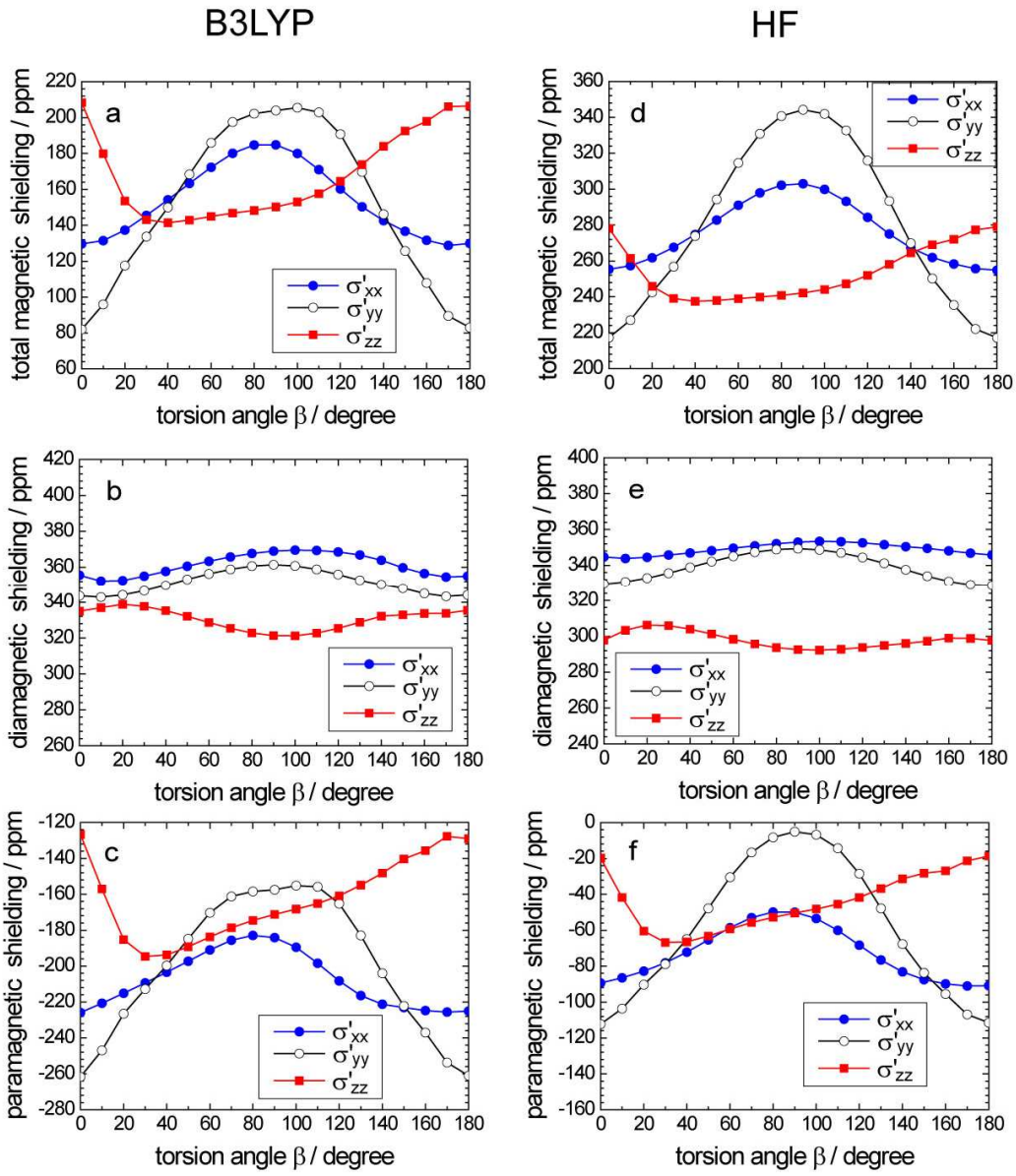

Fig. 3.12. Torsion angle β dependence of the ^{15}N NMR shielding tensor components, σ'_{xx} (•), σ'_{yy} (○), and σ'_{zz} (■), of TPD. The β and γ values are assumed to be equal and the other structural parameters are fixed to the optimized values. The ^{15}N NMR total shieldings, diamagnetic shieldings, and paramagnetic shieldings calculated at B3LYP/6-31G(d) levels are shown in (a), (b), and (c), respectively. Those calculated at HF/STO-3G level are shown in (d), (e), and (f), respectively.

3.3.5. NCS Analysis and Origins of the Torsion Angle β Dependence of the Paramagnetic NMR Deshielding

Here, orbitals contribute to the paramagnetic σ'_{yy} and σ'_{zz} values are investigated by NCS analyses. Fig. 3.13a shows the torsion angle β dependence of the paramagnetic σ'_{yy} value divided into the contributions from the nitrogen-related 4 NLMOs and the other 133 NLMOs. It is found that the contribution from the nitrogen-related NLMOs is dominant for the torsion angle β dependence. The difference between the maximum and minimum values is 113 ppm for the contribution from the nitrogen-related NLMOs, while that for the total contribution from the other 133 NLMOs is only 7 ppm. For more detailed investigations, Fig. 3.14a shows the torsion angle β dependence of the paramagnetic σ'_{yy} value produced by each nitrogen-related NLMO. It is clear that the σ orbitals of the N-C5 and N-C9 bonds and the lone pair orbital are dominant for the torsion angle β dependence. It can be considered that the deshielding is produced by the overlaps between (1) the 90^o rotated lone pair orbital around the y-axis and the σ^* orbitals of the N-C5 and N-C9 bonds and (2) the 90^o rotated σ orbitals of the N-C5 and N-C9 bonds around the y-axis and the π^* orbitals of the N-C5 and N-C9 bonds. The N-C4 bond does not contribute to the paramagnetic σ'_{yy} value, because it is parallel to the y-axis, and thus, the y component of the orbital angular momentum is equal to 0. Fig. 3.15 shows the torsion angle β dependence of the orbital energies of the nitrogen-related occupied and virtual NBOs. The corresponding orbital coefficients are shown in Table 3.2 for several conformers. As in the case of Fig. 3.9 and Table 3.1, the energy levels and orbital coefficients are almost stable irrespective of the β value, and thus, these are not the cause of the torsion angle β dependence of the ^{15}N NMR deshielding. Fig. 3.16 shows the stabilization energies of the lone pair orbital caused by the interaction with the π orbital of the biphenylene, phenyl, and tolyl rings. It is found that the stabilization energies between the lone pair orbital and the π orbitals of the

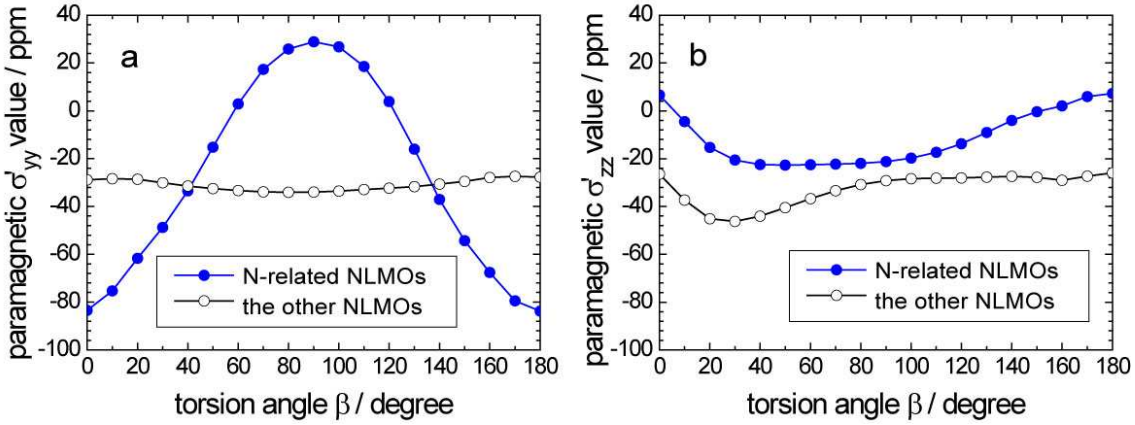

Fig. 3.13. Torsion angle β dependence of the ^{15}N paramagnetic shielding components, (a) σ'_{yy} and (b) σ'_{zz}, of TPD, divided into the contributions from the nitrogen-related NLMOs (•) and the other NLMOs (○). The nitrogen-related NLMOs correspond to the lone pair orbital and the σ orbitals of the three N-C bonds around the nitrogen. The other NLMOs indicate total contribution from the remaining 133 NLMOs. The calculations were performed at HF/STO-3G level.

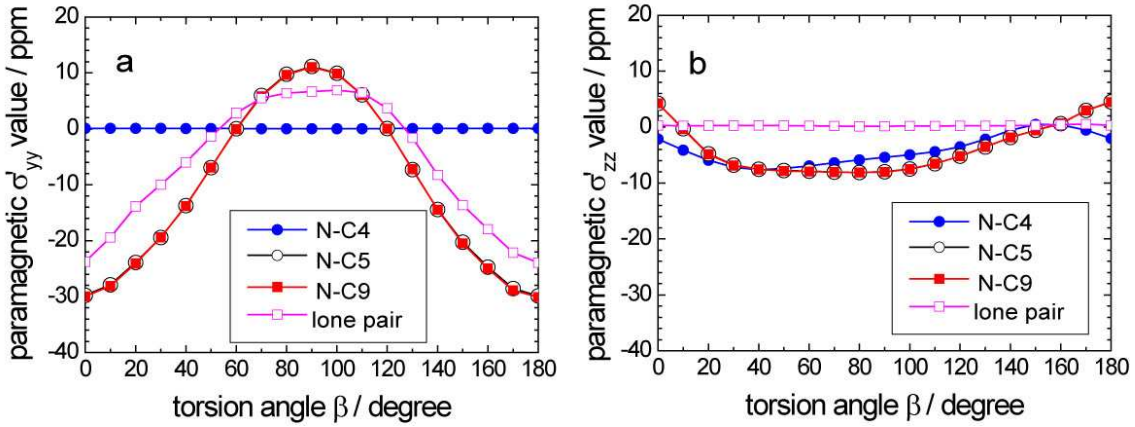

Fig. 3.14. Torsion angle β dependence of the ^{15}N paramagnetic shielding components, (a) σ'_{yy} and (b) σ'_{zz}, of TPD, divided into the contributions from the lone pair orbital (•) and the σ orbitals of the three N-C bonds around the nitrogen, N-C4 (○), N-C5 (■), and N-C9(□). The calculations were performed at HF/STO-3G level.

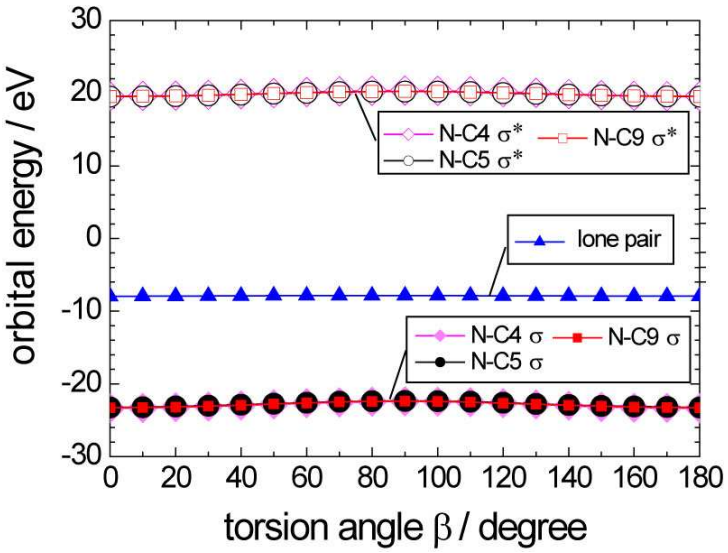

Fig. 3.15. Torsion angle β dependence of the orbital energies of the nitrogen-related NBOs (σ orbitals of the N-C4 (♦), N-C5 (•), N-C9 (■) bonds and lone pair orbital (▲)) and virtual NBOs (σ^* orbitals of the N-C4 (◊), N-C5 (○), and N-C9 (□) bonds). The calculations were performed at HF/STO-3G level.

Table 3.2. Orbital coefficients of the nitrogen-related NBOs (σ and σ^* orbital of the N-C4, N-C5, and N-C9 bonds and lone pair orbitals) for the conformer with β = 0, 40, 90, 140 and 180°. The other structural parameters are fixed to the optimized values, assuming that β = γ. The calculations were carried out at HF/STO-3G level.

β / degree	N-C4 σ orbital			N-C5 σ orbital			N-C9 σ orbital			lone pair orbital		
	p_x	p_y	p_z	p_x	p_y	p_z	p_x	p_y	p_z	p_x	p_y	p_z
0	0.00	-0.62	0.00	0.54	0.31	0.00	-0.54	0.31	0.00	0.00	0.00	-1.00
40	0.00	-0.62	0.00	0.54	0.31	0.00	-0.54	0.31	0.00	0.00	0.00	-1.00
90	0.00	-0.62	0.00	0.54	0.31	0.00	-0.54	0.31	0.00	0.00	0.00	-1.00
140	0.00	-0.62	0.00	0.54	0.31	0.00	-0.54	0.31	0.00	-0.01	0.00	-1.00
180	0.00	-0.63	0.00	0.54	0.31	0.00	-0.54	0.31	0.00	0.00	0.00	-1.00

β / degree	N-C4 σ^* orbital			N-C5 σ^* orbital			N-C9 σ^* orbital		
	p_x	p_y	p_z	p_x	p_y	p_z	p_x	p_y	p_z
0	0.00	0.53	0.00	-0.45	-0.26	0.00	0.45	-0.26	0.00
40	0.00	0.53	0.00	-0.46	-0.26	0.00	0.46	-0.26	0.00
90	0.00	0.53	0.00	-0.46	-0.27	0.00	0.46	-0.27	0.00
140	0.00	0.53	0.00	-0.46	-0.26	0.00	0.46	-0.26	0.00
180	0.00	0.53	0.00	-0.45	-0.26	0.00	0.45	-0.26	0.00

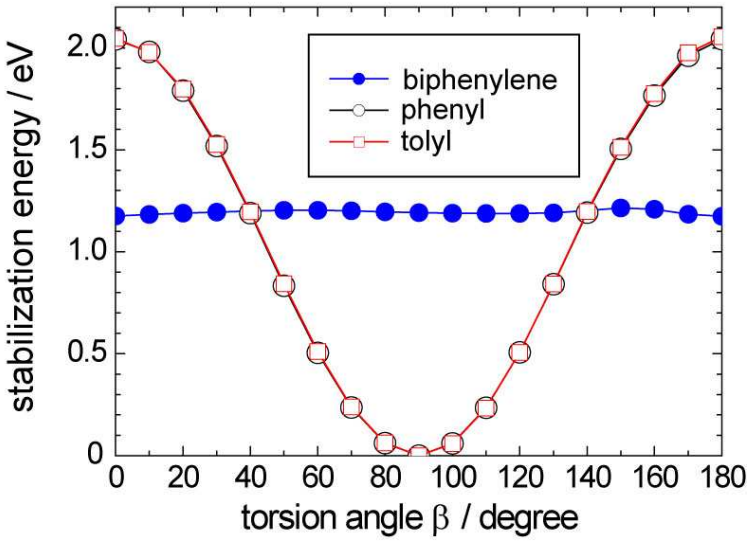

Fig. 3.16. Torsion angle β dependence of the stabilization energy of the lone pair orbital by the interaction with the π orbitals of the biphenylene (•), phenyl (○), and tolyl (□) rings, obtained by HF/STO-3G calculations.

phenyl and tolyl rings are the largest for the conformer with $\beta = 0, 180^{o}$ and the smallest for the conformer of $\beta = 90^{o}$. The tendency is consistent with the torsion angle β dependence of paramagnetic σ'_{yy} value, suggesting that the σ and π^{*} orbitals and the π and σ^{*} orbitals of the N-C5 and N-C9 bonds strongly interact with each other to produce the paramagnetic σ'_{yy} deshielding when the benzene ring of the phenyl and tolyl moieties and the nitrogen-centered plane are parallel to each other.

Fig. 3.13b shows the paramagnetic σ'_{zz} values divided into the contributions from the nitrogen-related NLMOs and the other NLMOs. It is found that the difference between the maximum and minimum values is 30 ppm for the nitrogen-related NLMOs, while that for the other 133 NLMOs is 20 ppm. The contribution from each nitrogen-related NLMO is separately shown in Fig. 3.14b. It is clear that the σ orbitals of the N-C4, N-C5 and N-C9 bonds subject the paramagnetic deshielding, while the lone pair orbital hardly produces the paramagnetic deshielding. It can be considered that the rotated σ orbitals around z-axis overlap with the σ^{*} orbitals to produce the paramagnetic σ'_{zz} value, as discussed in Fig. 3.8. The relatively small deshielding from the σ orbitals are attributed to the large energy difference between the σ and σ^{*} orbitals as shown in Fig. 3. 15. The origins of the torsion angle β dependence of the paramagnetic σ'_{zz} value can be understood by the interaction energy between the σ and σ^{*} orbitals in Fig. 3.17. The large total interaction in Fig .3.17b almost corresponds to the significant σ'_{zz} deshielding in Figs. 3.12f, 3.13b, and 3.14b.

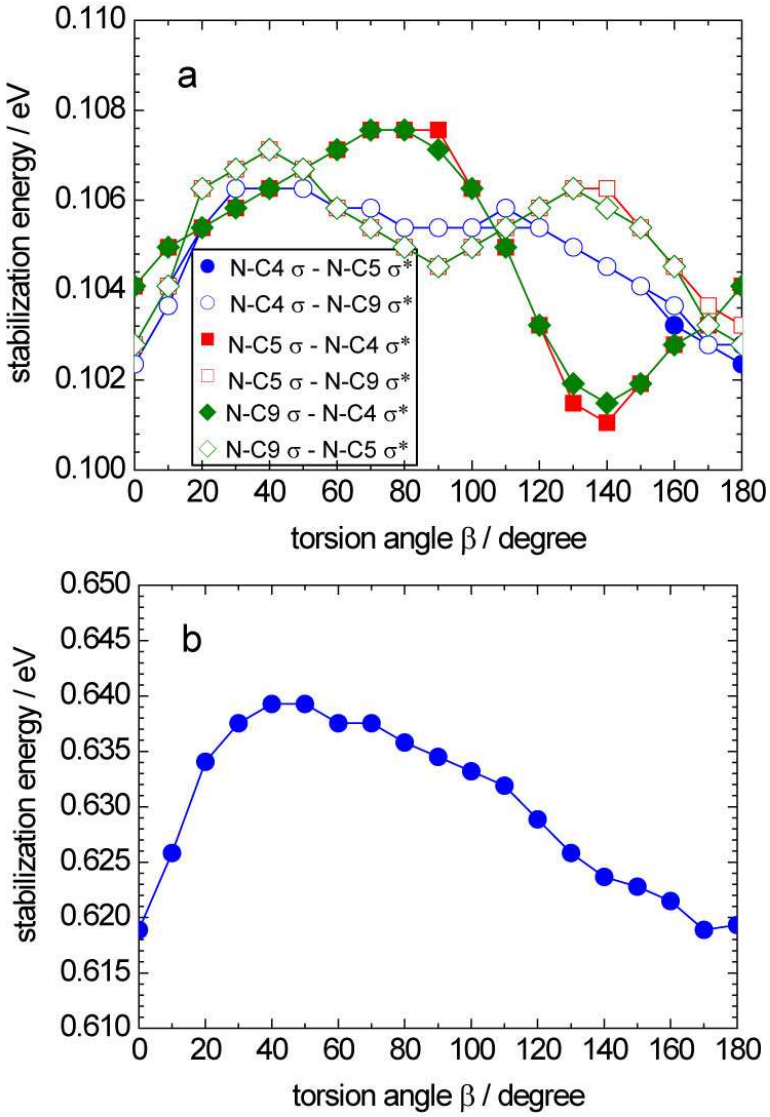

Fig. 3.17. Torsion angle β dependence of the stabilization energy for the σ orbitals of the N-C4 (•, ○), N-C5 (■, □), and N-C9 (♦, ◊) bonds by the interaction with the σ^* orbitals. The stabilization energy for each interaction is shown in (a) and the total stabilization energy is shown in (b). The calculations were performed at the level of HF/STO-3G.

3.3.6. Conformational Dependence of HOMO and LUMO

In Fig. 3.18, HOMO for the DFT-optimized geometry of TPD is shown. It is suggested that the HOMO consists of the nitrogen lone pair orbitals and the π orbitals of the benzene rings. From the above investigations, it was found that interaction between the lone pair orbitals and π orbitals is strongly affected by the torsion angles, α and β. This indicates that the torsion angles would have considerable influence on the HOMO. Fig. 3.19a shows the torsion angle α dependence of the HOMO, expressed by the summation of the squares of the MO coefficients in percentage for respective molecular moieties, nitrogen, biphenylene, phenyl, and tolyl moieties. The calculations were carried out by B3LYP/6-31G(d) method. The HOMOs for the representative conformers are illustrated in Fig. 3.18. From Figs. 3.18 and 3.19a, it is found that the HOMO is almost localized on the biphenylene and nitrogen moieties for the conformers with $\alpha = 0, 180^{o}$, for which the lone pair orbital and the biphenylene π orbitals strongly interact with each other (see Fig. 10). In contrast, the HOMO is localized on the nitrogen, phenyl, and tolyl molieties for the conformer with $\alpha = 90^{o}$, for which the interaction between the lone pair orbital and the biphenylene π orbitals is smaller than that between the lone pair and π orbitals of the phenyl and tolyl rings. Similarly, Fig. 3.19b shows the torsion angle β dependence of the HOMO. The HOMO is mostly delocalized over the molecule for the conformer with $\beta = 0, 180^{o}$. In contrast, for the conformer with $\beta = 90^{o}$, the HOMO is localized on the biphenylene moiety. For the DFT-optimized conformer, for which the α and β values are $\sim 40^{o}$ [2,27,28], the HOMO is relatively delocalized over the molecule; the largest contribution is from the biphenylene moiety, 40%. Because, in Chapter 5, the delocalization of the frontier orbitals is shown to be advantageous for intermolecular charge transports in condensed TPD, the relatively delocalized HOMO of the DFT-optimized geometry should be favorable for hole transports. Consistent results were obtained from the HF/STO-3G calculations as shown in Fig. 3.20,

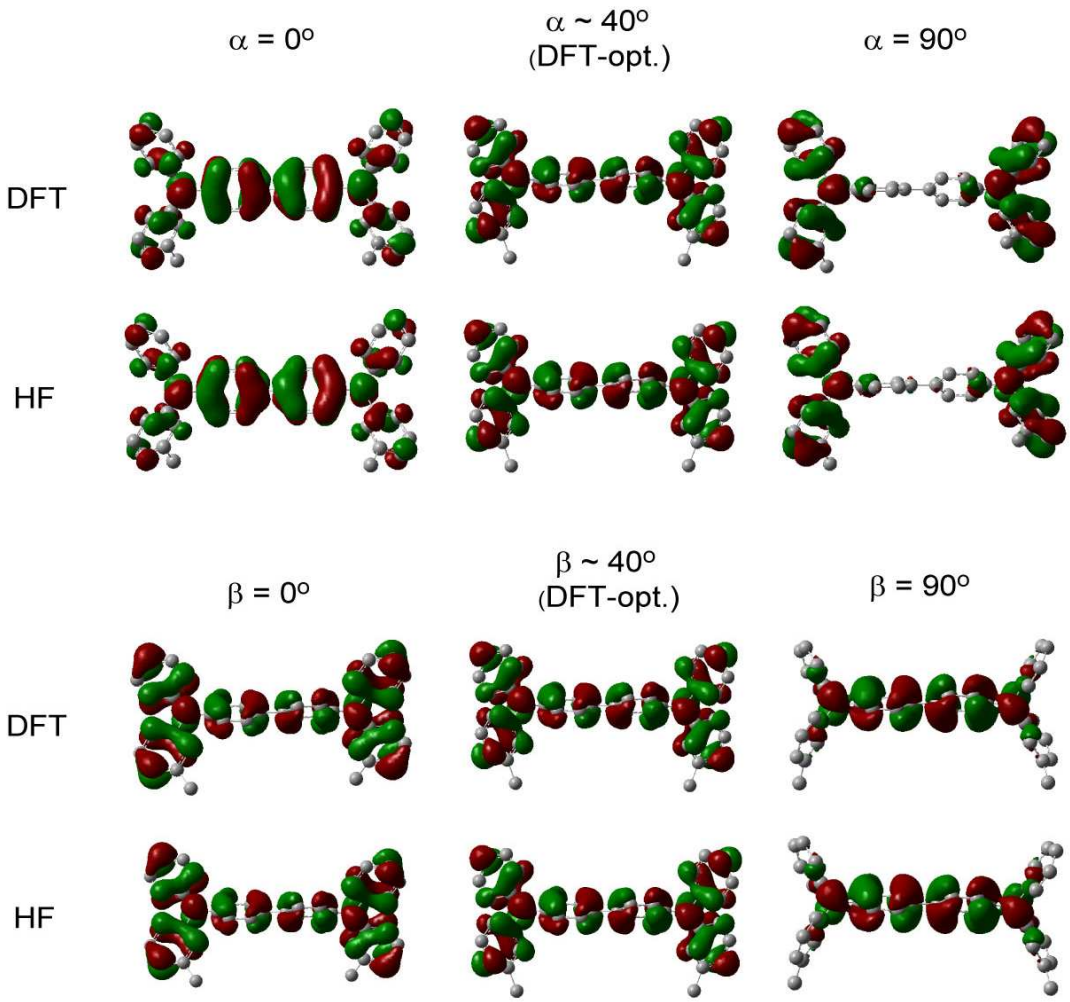

Fig. 3.18. The HOMOs for the DFT-optimized geometry of TPD and the conforms with α, β = 0°, 90°. The calculations were performed at B3LYP/6-31G(d) or HF/STO-3G level. The isosurface value for the visualizations is 0.02 a.u.

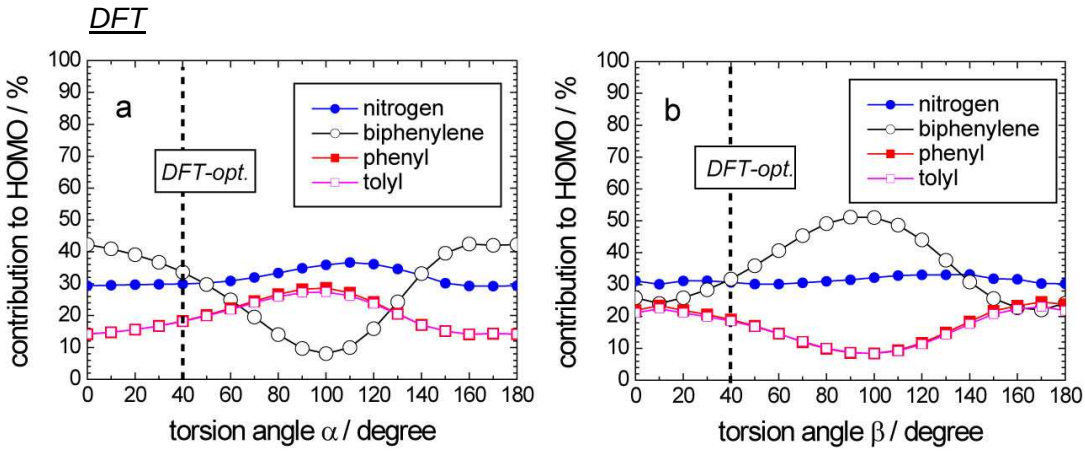

Fig. 3.19. Torsion angles, (a) α and (b) β, dependences of HOMO of TPD, expressed by the summation of the squares of the MO coefficients in percentage for respective molecular moieties, nitrogen (•), biphenylene (○), phenyl (■), and tolyl (□). The β and γ values are assumed to be equal and all the other structural parameters are fixed to the optimized values. The calculations were performed by B3LYP/6-31G(d) method.

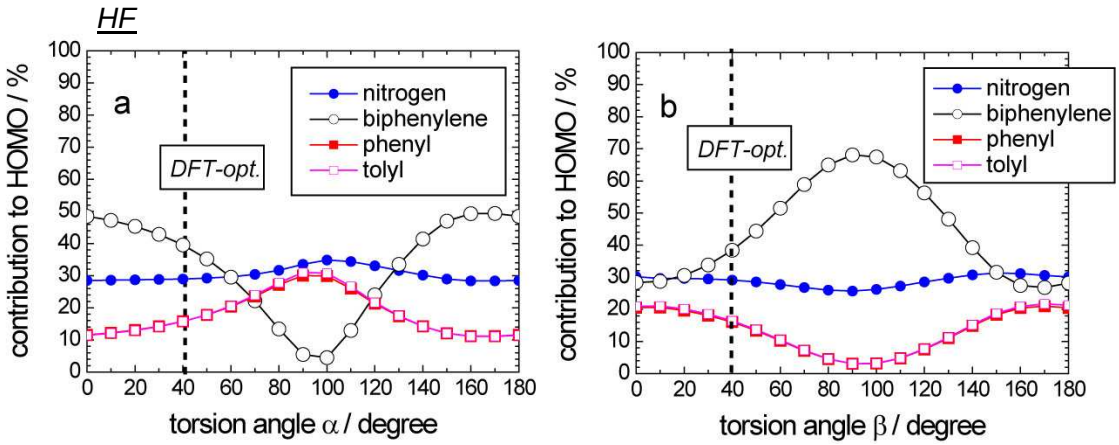

Fig. 3.20. Torsion angles, (a) α and (b) β, dependences of HOMO of TPD, expressed by the summation of the squares of the MO coefficients in percentage for respective molecular moieties, nitrogen (•), biphenylene (○), phenyl (■), and tolyl (□). The β and γ values are assumed to be equal and all the other structural parameters are fixed to the optimized values. The calculations were performed by HF/STO-3G method.

supporting the results obtained by B3LYP/6-31G(d) calculations.

The torsion angles, α and β, dependences of the LUMO, calculated by B3LYP/6-31G(d) method, are shown in Figs. 3.21a and 3.21b, respectively. For comparison, the HF/STO-3G results are shown in Fig. 3.22. The LUMOs for the representative conformers are illustrated in Fig. 3.23. It is found from Figs. 3.21-3.23 that the LUMO is extremely localized on the biphenylene moiety irrespective of α and β values, except the DFT results for the conformer with $\beta \sim 90^{o}$. The inconsistency between the HF and DFT results indicates that the DFT-calculated MOs should be dealt with carefully. Because the physical interpretation of the MOs is controversial [14-17], the detail is not discussed in this study. As discussed in Chapter 5, the localized LUMO on the central biphenylene moiety is unfavorable for intermolecular electron transports, suggesting the inferior electron transport property of TPD, irrespective of α and β values.

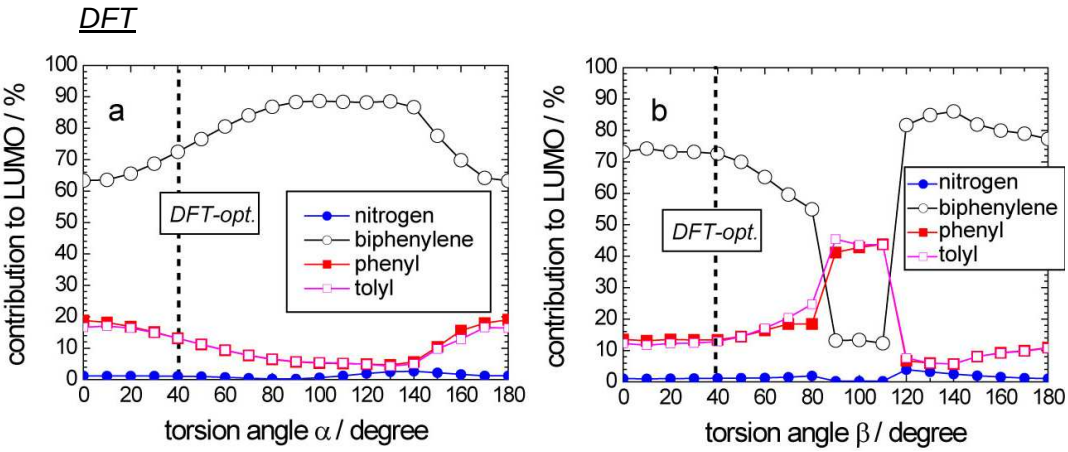

Fig. 3.21. Torsion angles, (a) α and (b) β, dependences of LUMO of TPD, expressed by the summation of the squares of the MO coefficients in percentage for respective molecular moieties, nitrogen (•), biphenylene (○), phenyl (■), and tolyl (□). The β and γ values are assumed to be equal and all the other structural parameters are fixed to the optimized values. The calculations were performed by B3LYP/6-31G(d) method.

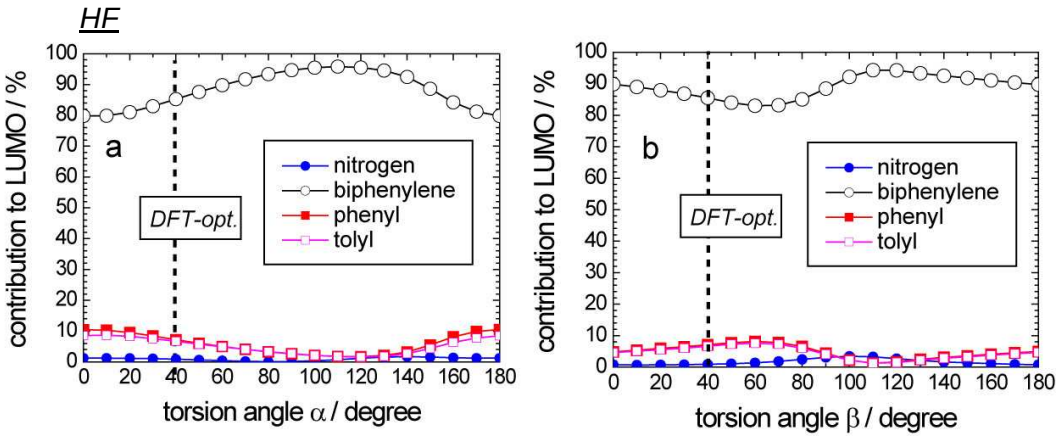

Fig. 3.22. Torsion angles, (a) α and (b) β, dependences of LUMO of TPD, expressed by the summation of the squares of the MO coefficients in percentage for respective molecular moieties, nitrogen (•), biphenylene (○), phenyl (■), and tolyl (□). The β and γ values are assumed to be equal and all the other structural parameters are fixed to the optimized values. The calculations were performed by HF/STO-3G method.

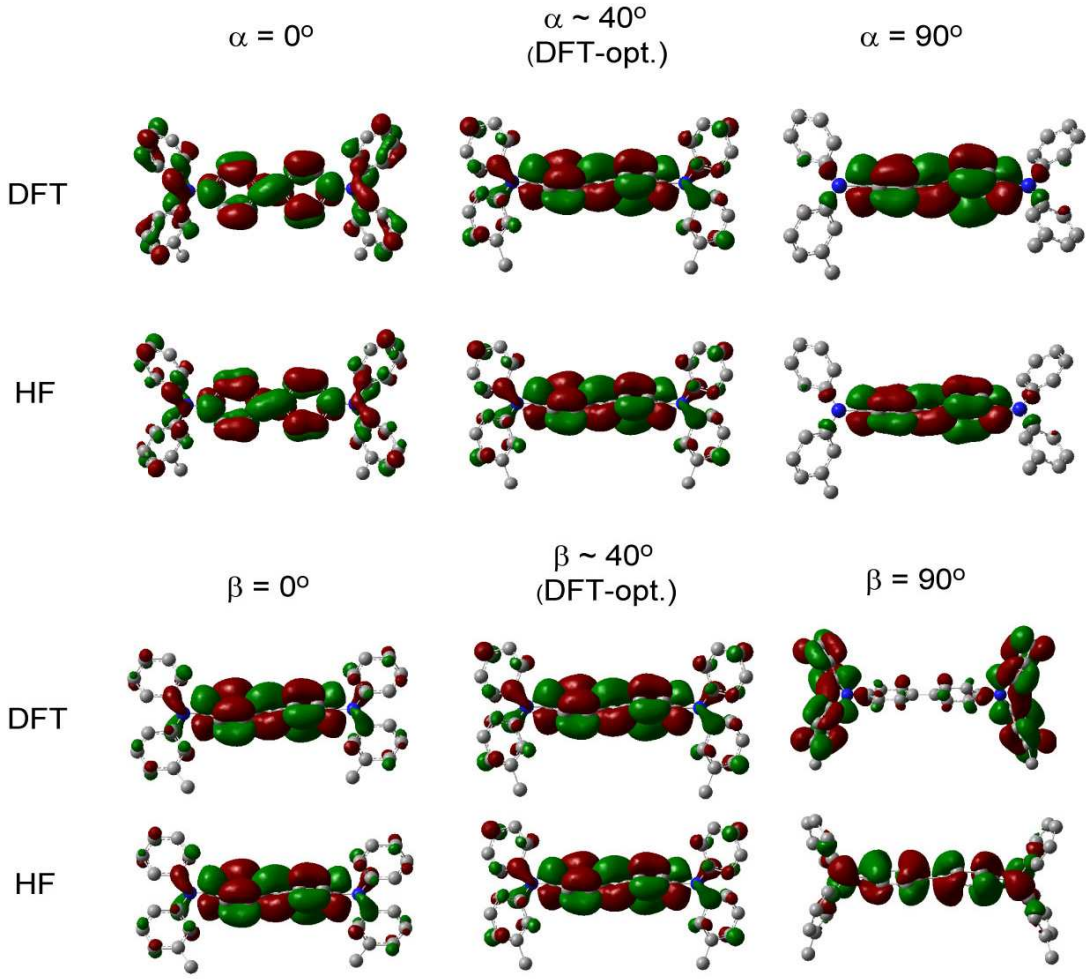

Fig. 3.23. The LUMOs for the DFT-optimized geometry of TPD and the conforms with α, β = 0°, 90°. The calculations were performed at B3LYP/6-31G(d) or HF/STO-3G level. The isosurface value for the visualizations is 0.02 a.u.

3.4. Conclusion

The origins of the torsion angles, α and β, dependences of the ^{15}N CSA span of TPD were analyzed, dividing the NMR shieldings into the diamagnetic shielding and paramagnetic deshielding terms with the help of NCS analysis. It was revealed that the torsion angles dependences are dominated by the paramagnetic deshielding term, rather than the diamagnetic shielding term. For the parallel direction to the nitrogen-centered plane, the paramagnetic deshielding is caused by the nitrogen p_z orbital and the orthogonal component of the N-C σ orbitls to the magnetic field. The deshielding is affected by the interaction between the nitrogen lone pair orbital and the π orbitals. For the vertical direction to the nitrogen-centered plane, the paramagnetic deshielding can be ascribable to the interactions between the σ and σ* orbitals of the N-C bonds, although the contributions are small due to the large energy gaps between the orbitals.

It was also found that the distribution of HOMO is largely changed depending on the conformation. The HOMO is localized on the nitrogen and benzene rings which strongly interact with the nitrogen lone pair orbital. For the DFT-optimized conformation, the HOMO is relatively delocalized over the molecule. The advantageous of the delocalization for hole transports is shown in Chapters 5 and 6. On the other hand, it was suggested that the LUMO is almost delocalized on the biphenylene moiety, indicating the inferior electron-transport property of TPD.

References

[1] K. Sugiyama, D. Yoshimura, T. Miyamae, T. Miyazaki, H. Ishii, Y. Ouchi, K. Seki, J. Appl. Phys. 83 (1998) 4928.

[2] B. Lin, C. Cheng, Z. Lao, J. Phys. Chem. A 107 (2003) 5241.

[3] N.F. Ramsey, Phys. Rev. 91 (1953) 303.

[4] J. Bohmann, T.C. Farrar, J. Phys. Chem. 100 (1996) 2646.

[5] Y. Ruiz-Morales, G. Schreckenbach, T. Ziegler, J. Phys. Chem. 100 (1996) 3359.

[6] J.A. Bohmann, F.Weinhold, T.C. Farrar, J. Chem. Phys. 107 (1997) 1173.

[7] K.W. Feindel, K.J. Ooms, R.E. Wasylishen, Phys. Chem. Chem. Phys. 9 (2007) 1226.

[8] G.G. Briand, A.D. Smith, G. Schatte, A.J. Rossini, R.W. Schurko, Inorg. Chem. 46 (2007) 8625.

[9] J.W.E. Weiss, D.L. Bryce, J. Phys. Chem. A 114 (2010) 5119.

[10] A.D. Becke, Phys. Rev. A 38 (1988) 3098.

[11] A.D. Becke, J. Chem. Phys. 98 (1993) 1372.

[12] A.D. Becke, J. Chem. Phys. 98 (1993) 5648.

[13] C.T. Lee, W.T. Yang, R.G. Parr, Phys. Rev. B 37 (1988) 785.

[14] R.G. Parr, W. Yang, Density Functional Theory of Atoms and Molecules, Oxford University Press, New York, 1989.

[15] P. Politzer, F. Abu-Awwad, Thor. Chem. Acc. 99 (1998) 83.

[16] R. Stowasser, R. Hoffmann, J. Am. Chem. Soc. 121 (1999) 3414.

[17] D.P Chong, O.V. Gritsenko, E.J. Baerends, J. Chem. Phys. 116 (2002) 1760.

[18] J.P. Foster, F. Weinhold, J. Am. Chem. Soc. 102 (1980) 7211.

[19] A.E. Reed, F. Weinhold, J. Chem. Phys. 78 (1983) 4066.

[20] A.E. Reed, R.B. Weinstock, F. Weinhold, J. Chem. Phys. 83 (1985) 735.

[21] A.E. Reed, L.A. Curtiss, F. Weinhold, Chem. Rev. 88 (1988) 899.

[22] A.E. Reed, F. Weinhold, J. Chem. Phys. 83 (1985) 1736.

[23] M.J. Frisch et al., Gaussian 03, Revision E.01, Gaussian, Inc., Wallingford CT, 2004.

[24] E. Kleinpeter, S. Klod, J. Am. Chem. Soc. 126 (2004) 2231.

[25] P.R. Seidl, J.W.M. Carneiro, J.G.R. Tostes, A. Koch, E. Kleinpeter, J. Phys. Chem. A 109 (2005) 802.

[26] Y. Lin, H. Nekvasil, J. Tossell, J. Phys. Chem. A 109 (2005) 3060.

[27] M. Malagoli, J. Bredas, Chem. Phys. Lett. 327 (2000) 13.

[28] H. Kaji, T. Yamada, N. Tsukamoto, F. Horii, Chem. Phys. Lett. 401 (2005) 246.

Chapter 4

Solid-State ^{15}N NMR Study of TPD in the Neutral and Charged States

4.1. Introduction

The molecular and electronic structures of *N*,*N*'-diphenyl-*N*,*N*'-di(*m*-tolyl)benzidine (TPD) (see Fig. 4.1) in the neutral state were analyzed in Chapters 2 and 3. It is considered that, to a good approximation, charges locate on one TPD molecule at a certain instant, and that the charges are transferred among neutral and charged molecules by a hopping mechanism due to weak intermolecular interaction [1-4]. Therefore, analyses of the molecular and electronic structures of a TPD molecule, in charged as well as neutral states, are crucial to understanding charge-transport properties. For the molecular structure, the first X-ray diffraction (XRD) study was carried out in 2002 by Kennedy et al. [5], and since then, XRD studies were pursued by several groups [6-10]. However, even the crystal structure of neutral TPD is still controversial [5-7]. For the charge state, the molecular structure analysis was attempted by Low et al. [8-10]. In their studies, the structures of TPD in the cationic and dicationic states themselves were not analyzed, while those of the TPD analogues were investigated. One of the difficulties of the structural analysis of TPD originates from the existence of many conformers as described in Chapter 2. They induce structural disorders and tend to prohibit crystallization. This feature is favorable for OLEDs, because TPD is used in the amorphous state in the device. Crystallization, which results in device degradation, should be avoided for long life-time devices. However, this favorable feature conversely makes the structural analysis difficult even for the crystal.

For the electronic structure, the ionization potential was studied [11]. More detailed information, including other valence electronic structures, was obtained by UV photoemission

spectroscopy combined with molecular orbital calculations [12,13]. However, experimental results which can access the charge-transport property are scarce.

In this Chapter, solid-state ^{15}N NMR experiments are attempted on TPD in the neutral and charged states, combined with density functional theory (DFT) calculation to analyze the electronic states. Solid-state NMR experiments can provides information on disordered and amorphous materials to a similar extent as crystals [14-21]. If the solid-state NMR method can distinguish the neutral and charged states, it would be powerful tool to investigate the charge states and to observe the charge-transport phenomena in the devices.

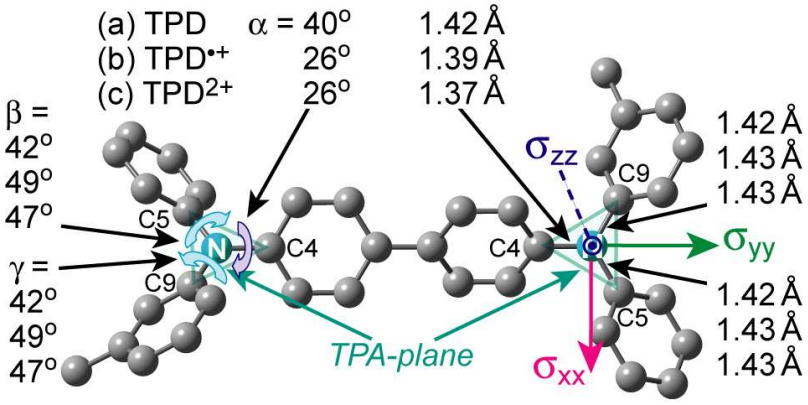

Fig. 4.1. Orientation of the chemical shift tensor of ^{15}N nuclei (σ_{xx}, σ_{yy}, σ_{zz}) in TPD. DFT-optimized bond lengths and torsion angles around ^{15}N are also shown for TPD, TPD$^{\bullet+}$, and TPD^{2+} from top to bottom. Hydrogen atoms are omitted for clarity.

4.2 Experimental and Computational Section

4.2.1. Samples

The ^{15}N-labeled TPD sample in the amorphous state (^{15}N-aTPD) was obtained as shown in Chapter 2. The charged states were produced by chemical doping of ^{15}N-aTPD. The ^{15}N-aTPD sample (99 mg, 0.19 mmol) dissolved in $CHCl_3$ and $SbCl_5$ (115 mg, 0.384 mmol) dissolved in $CHCl_3$ were mixed so as to provide a deep reddish orange solution. By drying the solution under vacuum for one day, a deep reddish orange monoradical cation sample, $TPD^{\bullet+} \cdot SbCl_6^-$, was obtained. Occasionally, the TPD : $SbCl_5$ = 1 : 2 mixture yields a mixture of cationic and dicationic TPD molecules; however, dicationic TPD forms precipitates, which can be easily filtered. It should be noted that the mixture of TPD and $SbCl_5$ with the molar ratio of TPD : $SbCl_5$ = 1 : 1 provides a mixture of neutral and cationic TPD molecules, which are difficult to be separated. In order to make the dication sample, a TPD : $SbCl_5$ = 1 : 3 mixture was prepared by mixing ^{15}N-aTPD (50 mg, 0.096 mmol) in $CHCl_3$ and $SbCl_5$ (87 mg, 0.29 mmol) in $CHCl_3$. This mixture produced metallic, deep red-colored precipitates. The precipitates were dried under vacuum for one day, which resulted in a dication sample, $TPD^{2+} \cdot 2SbCl_6^-$. All of the processes for the $SbCl_5$-doping were carried out under the N_2 atmosphere. The formations of cationic and dicationic states were confirmed by elemental analyses below, ESR and NMR experiments. Anal. Calcd. for $TPD^{\bullet+} \cdot SbCl_6^-$: C, 53.62; H, 3.79; N, 3.29; Cl, 24.99. Found: C, 53.17; H, 3.46; N, 3.22; Cl, 19.65. Anal. Calcd. for $TPD^{2+} \cdot 2SbCl_6^-$: C, 38.49; H, 2.72; N, 2.36; Cl, 35.88. Found: C, 38.85; H, 2.79; N, 2.25; Cl, 34.97.

4.2.2. ESR Experiments

The existence of unpaired electron spins can be confirmed by ESR measurements. The ESR measurements were carried out on a Bruker Biospin ELEXSYS E500 CW-EPR spectrometer. All the experiments were carried out for solid samples at room temperature.

4.2.3. Solid-State ^{15}N NMR Experiments

^{15}N NMR measurements were performed on a Chemagnetics CMX-400 Infinity spectrometer operating at a ^{15}N frequency of 40.4 MHz (under a static magnetic field of 9.4 T). A double resonance probe with a 4 mm magic angle spinning (MAS) probehead was used. The powdered samples were packed into zirconia rotors under an inert atmosphere of nitrogen. The ^{1}H 90˚ pulse length was 2.0 μs and the contact time for the cross polarization (CP) process was 10.0 ms. The ^{15}N does not have directly-bonded ^{1}H, and the ^{1}H-^{15}N dipolar coupling was relatively weak. A ^{1}H dipolar decoupling with a ^{1}H field strength of 40 kHz, which was sufficient for decoupling, was used during the detection of free induction decay (FID).

For CP/MAS ^{15}N NMR measurements, variable-amplitude CP and MAS with a spinning speed of 12 kHz were applied. The numbers of scans was 128 for all of the measurements. The isotropic chemical shifts, σ_{iso}, were obtained from the CP/MAS measurements. For ^{15}N chemical shift anisotropy (CSA) measurements, standard CP and the Hahn echo (τ– π-pulse –τ), with τ = 20 μs, were applied before detection. The number of scans was 2048 for TPD in the neutral and cationic states, and 4096 for TPD in the dicationic state. The spectra were obtained without sample spinning. The chemical shift principal values, σ_{xx}, σ_{yy}, and σ_{zz}, were obtained by CSA measurements. All of the experiments were carried out at room temperature. The ^{15}N chemical shifts were expressed as values relative to liquid ammonia (NH_3) using the solid $^{15}NH_4Cl$ resonance line with 39.1 ppm as an external reference [22,23].

4.2.4. Computations

The geometry optimizations of TPD in the neutral, cationic, and dicationic states were carried out in DFT using the B3LYP functional, wherein Becke's three-parameter hybrid exchange functional [24-26] was combined with the Lee-Yang-Parr correlation functional [27]. The 6-31G(d) split valence plus polarization basis set was used, which is most frequently used for geometry optimizations of TPD molecules [28-32]. The nuclear magnetic shielding calculations for the DFT-optimized TPD, $TPD^{\bullet+}$, and TPD^{2+} single molecules were carried out with the gauge including atomic orbitals (GIAO) method [33-35] using DFT at the B3LYP/6-31G(d) level. All of the calculated chemical shifts were referenced by the experimental isotropic chemical shift of the ^{15}N resonance line of TPD in the neutral state, 100.8 ppm, which was obtained from the CP/MAS ^{15}N NMR experiment. The chemical shift principal values were also obtained from the calculations. There are several ways to describe the chemical shift principal values. One way is to describe these values as σ_{11} (most downfield, or leftmost), σ_{22} (middle), and σ_{33} (most upfield, or rightmost). In this notation, the chemical shift for the z-direction corresponds to σ_{11} for neutral TPD, while to σ_{33} for cationic and dicationic TPD. In this study, we use another convention to avoid the confusion; the chemical shift principal values are described by σ_{xx}, σ_{yy}, and σ_{zz}, which correspond to those for the x-, y-, and z-directions, respectively. This provides easy understanding of the relationship between the principal values and the geometry. All of the calculations were performed with the Gaussian 03 program [36].

4.3. Results and Discussion

4.3.1. ESR Results

Fig. 4.2 shows the experimental ESR spectra of TPD in the neutral, cationic, and dicationic states. No resonance lines are observed for TPD in either the neutral or dicationic samples. In contrast, a relatively broad but clear ESR signal is observed for a monocationic sample. This indicates that only the monocationic TPD sample is radical and that the neutral and dicationic TPD samples are not radical species. The result agrees with that obtained by Low et al. [8].

Chemically reversible redox systems of TPD between TPD and TPD^{2+} were found by cyclic voltammetry and UV/Vis-NIR spectroelectrochemistry in the solution state, while TPD in higher charged states were not obtained [8]. This also confirms the formation of TPD^{2+} from the mixture consisting of a molar ratio of TPD : $SbCl_5$ = 1 : 3 without the formation of TPD^{3+} (see section 4.2.1) Combined with the solid-state NMR results, these samples were found to be $TPD^{\bullet+} \cdot SbCl_6^-$ and $TPD^{2+} \cdot 2SbCl_6^-$, respectively (see also the results of elemental analyses in section 4.2.1).

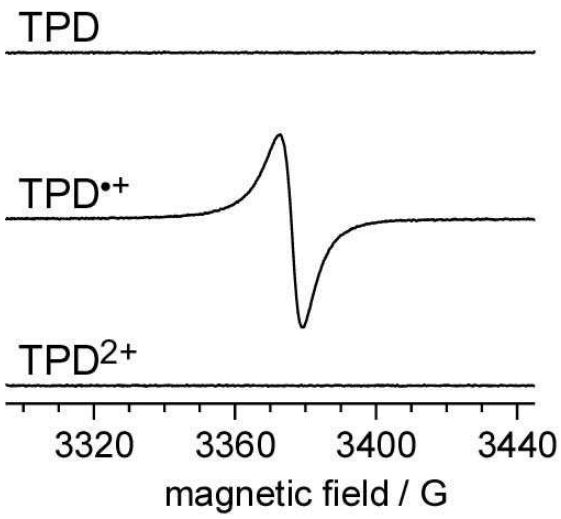

Fig. 4.2. Experimental ESR spectra of TPD in the neutral, cationic, and dicationic states.

4.3.2. Solid-State NMR and Computational Results

Fig. 4.3a shows the experimental CP/MAS ^{15}N NMR spectra of ^{15}N-labeled TPD in the neutral and charged states. The neutral sample provides a single resonance line at 100.8 ppm. For the cationic sample, no ^{15}N resonance lines are observed, even though this sample is 100% ^{15}N-enriched. The disappearance of the resonance line is due to the unpaired (radical) electron spin on the ^{15}N nuclei. The strong dipolar interaction between unpaired electrons and ^{15}N nuclei significantly broadens the ^{15}N resonance lines. In addition, the unpaired electrons also produce a large contact shift. The main contribution to the contact shift, that is, the Fermi contact shift, σ_{FC}, is calculated to produce a 4300-4400 ppm downfield shift based on Eqs. 4.1 and 4.2 [37].

$$\sigma_{FC} = m\frac{S+1}{T}\rho_{\alpha\beta} \tag{4.1}$$

$$m = \frac{\mu_0 \mu_B^2 g_e^2}{9k_B} = 23.5\times10^6 \ [\mathrm{ppm}\cdot\mathrm{K}\cdot\mathrm{a.u.}^{-1}] \tag{4.2}$$

Here, S is the total spin, T is the absolute temperature, and $\rho_{\alpha\beta}$ is the Fermi contact spin density. The values of μ_0, μ_B, g_e, and k_B are the vacuum permeability, Bohr magneton, free electron g-factor, and Boltzmann constant, respectively. Since the DFT calculations shows that the $\rho_{\alpha\beta}$ value for cationic TPD is 0.036–0.037 a.u. and S = 1/2, the Fermi contact shift at T = 298 K is obtained as 4300–4400 ppm. Both of the broadening and contact shift effects result in the disappearance of resonance lines in the observed chemical shift range. Because no resonance lines were observed for cationic TPD, both the two nitrogen nuclei in a TPD molecule strongly interact with the unpaired electron. This means that the two nitrogen atoms are electronically-

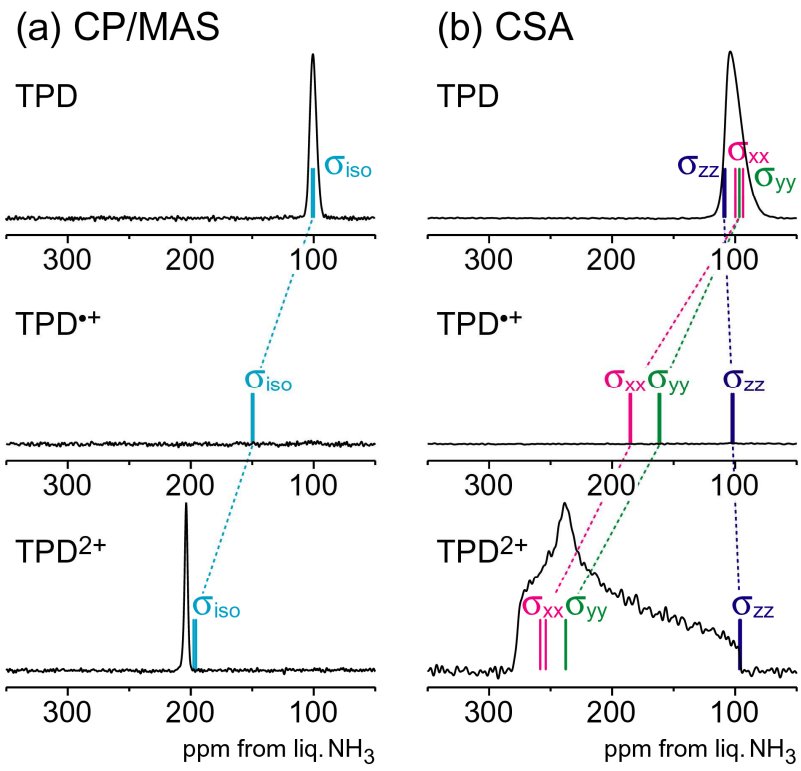

Fig. 4.3. Experimental (a) CP/MAS and (b) CSA ^{15}N spectra of ^{15}N-labeled TPD in the neutral, cationic, and dicationic states. DFT-calculated isotropic chemical shifts (σ_{iso}) and chemical shift principal values (σ_{xx}, σ_{yy}, σ_{zz}) are also shown by vertical bars.

coupled in spite of the relatively long intramolecular distance of 10.0 Å and are in same valence state. On the other hand, the dicationic sample shows a clear resonance line at 203.8 ppm, which is 103.0 ppm downfield-shifted from the neutral state. The appearance of the resonance line indicates that this sample is not in the biradical state, otherwise the ^{15}N resonance line disappears similarly with $TPD^{\bullet+}$. This observation is consistent with the above ESR results. In addition, the appearance of only one resonance line for TPD^{2+} in Fig. 4.3a indicates that the two ^{15}N nuclei in TPD^{2+} are not in different valence states, but principally in the same state.

The DFT-calculated ^{15}N isotropic chemical shifts of TPD in the neutral, cationic, and dicationic states are also shown in Fig. 4.3a as vertical bars. The cationic and dicationic TPD samples show downfield shifts of 47.5 and 94.5 ppm from the neutral TPD, respectively. Note that the Fermi contact shifts for $TPD^{\bullet+}$ are not included in this calculation. The calculated chemical shift for TPD^{2+} agrees well with the experimental chemical shift for chemically-doped dicationic TPD, confirming that the TPD molecules in this sample are in the dicationic state.

Fig. 4.3b shows the experimental ^{15}N CSA NMR spectra of TPD in the neutral and charged states. The ^{15}N CSA of the neutral TPD sample is unexpectedly narrow [38,39]; the CSA span, that is, the difference between the maximum and minimum chemical shift principal values is ~15 ppm (see Chapter 2). In contrast, a significantly wider ^{15}N CSA pattern is observed for the dicationic TPD, which has a CSA span of 181 ppm.

The DFT-calculated ^{15}N chemical shift principal values of TPD, σ_{xx}, σ_{yy}, and σ_{zz}, are shown in Fig. 4.3b as vertical bars. The orientations of the ^{15}N chemical shift tensors determined by DFT calculations are shown in Fig. 4.1. The N atom and the three directly-bonded carbons, C4, C5, and C9, are in the same plane not only in the neutral state [38,39] but also in the charged states [29,32]. This plane is referred to as the "TPA-plane" hereafter. The σ_{zz} direction corresponds to the normal vector direction of the TPA-plane. The σ_{yy} direction is along the

N-C4 bond vector. The σ_{xx} direction is perpendicular to both the σ_{zz} and σ_{yy} directions. For the neutral TPD, DFT calculations result in a narrow CSA [38,39], which agrees with the experimentally derived CSA pattern. The calculated CSA spans become wider with increasing the charge; 82.9 and 161.8 ppm for $TPD^{\bullet+}$ and TPD^{2+}, respectively. The experimental CSA span of a dicationic TPD sample, 181 ppm, agrees with the result of the DFT calculation for TPD^{2+}. Although the value of σ_{xx} differs by ~20 ppm, the agreement of both σ_{yy} and σ_{zz} is excellent.

The dominant origin of the 103 ppm-downfield shift for TPD^{2+} observed in Fig. 4.3a is the deficiency of electrons in the dicationic states. The lack of electrons reduces shielding of the ^{15}N nuclei. Another possible origin is the change of the geometric structure from neutral to dicationic states. DFT calculations show that the C4-N bonds gain a double-bond character with increasing positive charges, as shown in Fig. 4.1. Generally, in solid-state NMR, nuclei, such as ^{13}C and ^{15}N, with a double-bond character show a downfield shift and wider CSA compared to those with only single-bonds [22]. This feature is close to that observed in Fig. 4.3; however, this possibility is denied by the DFT calculations for the vertical transition states shown in Fig. 4.4. It is found from Fig. 4.4, TPD in the neutral, cationic, and dicationic charged states provide the isotropic chemical shifts of 100 - 107 ppm, 147 - 151 ppm, and 190 - 200 ppm, respectively, irrespective of the structures. Similarly, from Fig. 4.5, TPD in the neutral, cationic, and dicationic charged states provide (σ_{xx}, σ_{yy}, σ_{zz},) = (94-106, 93-100, 108-116), (170-187, 161-167, 99-107), (232-260, 236-240, 95-104), respectively, irrespective of the structures. It is concluded from the calculations that the above downfield shift reflects the charged states of TPD. Therefore, the CP/MAS and CSA experiments can be used to distinguish the charged states of molecules in organic devices.

The CSA measurements provide information on the direction from which electrons are

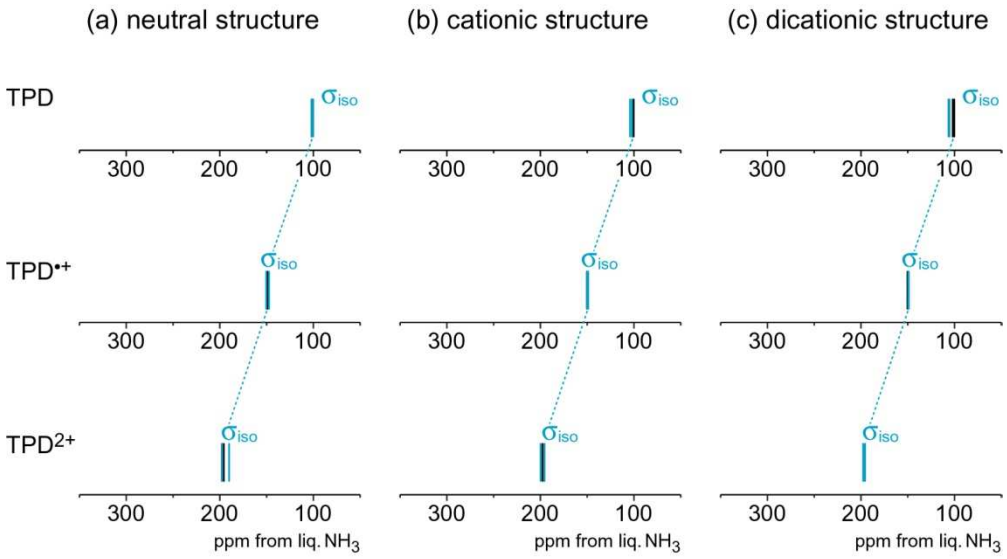

Fig. 4.4. Isotropic chemical shifts of TPD for vertical transition states obtained by DFT calculations. (a) TPD in the neutral (top), cationic (middle), and dicationic (bottom) charged states with the neutral structure. (b) TPD in the neutral (top), cationic (middle), and dicationic (bottom) charged states with the cationic structure. (c) TPD in the neutral (top), cationic (middle), and dicationic (bottom) charged states with the dicationic structure. In all of the spectra, the isotropic chemical shifts of TPD with the relaxed structures are also shown for comparison. Note that TPD in the neutral, cationic, and dicationic charged states provide the isotropic chemical shifts of 100–107 ppm, 147–151 ppm, and 190–200 ppm, respectively, irrespective of the structures.

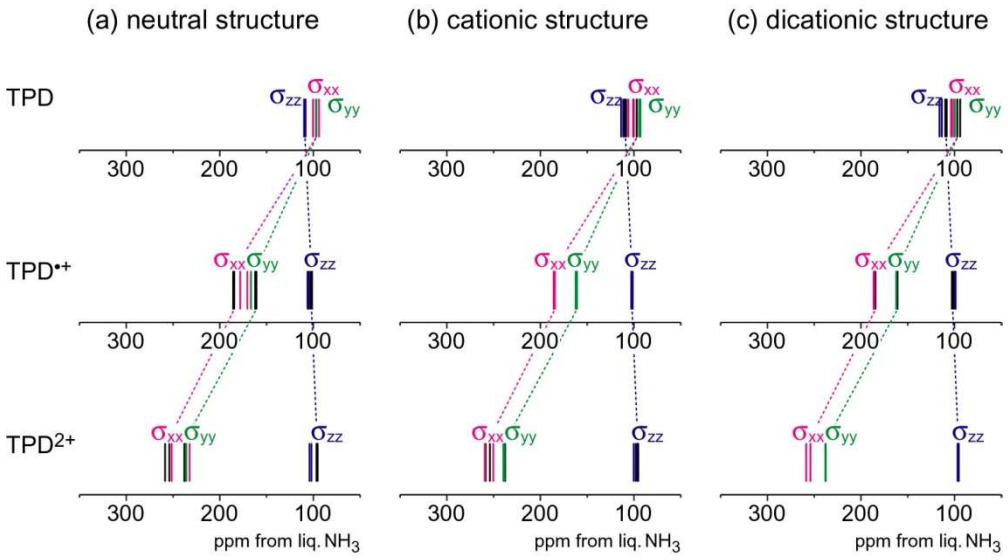

Fig. 4.5. Chemical shift principal values of TPD, σ_{xx}, σ_{yy}, and σ_{zz}, for vertical transition states. (a) TPD in the neutral (top), cationic (middle), and dicationic (bottom) charged states with the neutral structure. (b) TPD in the neutral (top), cationic (middle), and dicationic (bottom) charged states with the cationic structure. (c) TPD in the neutral (top), cationic (middle), and dicationic (bottom) charged states with the dicationic structure. In all of the spectra, the chemical shift principal values of TPD with the relaxed structures are also shown for comparison. TPD in the neutral, cationic, and dicationic charged states provide (σ_{xx}, σ_{yy}, σ_{zz},) = (94–106, 93–100, 108–116), (170–187, 161–167, 99–107), (232–260, 236–240, 95–104), respectively, irrespective of the structures.

extracted. For the TPD in the neutral, cationic, and dicationic states, σ_{xx} and σ_{yy} significantly change with increasing charges; however, the changes of the σ_{zz} values are negligible, as shown in Fig. 4.3b. This indicates that the electrons are extracted predominantly from the z-direction (normal direction of TPA-plane). The electrons in the xy-plane determine the shielding along the z-direction. The almost unchanged σ_{zz} values from TPD to TPD^{2+} indicate the electrons in the xy-plane are unchanged. The significant downfield shifts of σ_{xx} and σ_{yy}, that is, the large reduction in shielding along the x- and y-directions indicates that the electron populations along the z-direction decrease. The ^{15}N CSA NMR experiments in Fig. 4.3b therefore clearly indicate that the electron is extracted from the nitrogen lone pair ($2p_z$) orbitals, and that the resultant "holes" are on the nitrogen lone pair orbitals. It is shown that the solid-state NMR methods are useful to detect and analyze the charged states.

4.4. Conclusion

The solid-state ^{15}N NMR study of TPD in the neutral and charged states was presented. The charged states, cationic and dicationic states, were successfully prepared by the chemical doping. It was found that the two nitrogen atoms of a TPD molecule are in the same state in each sample, indicating that the two nitrogen atoms are electronically-coupled in spite of the relatively long intramolecular distance. It was also found from CP/MAS experiments that the charged states can be monitored by the change of the isotropic chemical shift. This means that the solid-state NMR approach would have the potential to observe charge transports in the devices, which is expected for the better understanding of charge transports phenomena. However, for the cationic state, ^{15}N NMR signals could not be observed due to the interaction between the ^{15}N nucleus and the unpaired electron. The NMR detection of the cationic sample by advanced NMR methods such as dynamic nuclear polarization (DNP) [40,41] is expected in

future.

It was also found from the CSA measurements that solid-state NMR can offer information on the orbitals from which the electrons are extracted. For TPD, electrons were found to be extracted from nitrogen $2p_z$ orbitals, which spread along the vertical direction of the TPA-plane, indicating that the orbitals contribute to the HOMO which are essential for hole transports.

References

[1] R.A. Marcus, J. Chem. Phys. 24 (1956) 966.

[2] R.A. Marcus, N. Sutin, Biochim. Biophys. Acta 811 (1985) 265.

[3] H. Bässler, Phys. Stat. Sol. B 175 (1993) 15.

[4] J. Cornil, D. Beljonne, J.P. Calbert, J.L. Brédas, Adv. Mater. 13 (2001) 1053.

[5] A. Kennedy, W. Smith, D. Tackley, W. David, K. Shankland, B. Brown, S. Teat, J. Mater. Chem. 12 (2002) 168.

[6] Z. Zhang, E. Burkholder, J. Zubieta, Acta Cryst. C60 (2004) o452.

[7] K. Shankland, A.R. Kennedy, W.I.F. David, J. Mater. Chem. 15 (2005) 4838.

[8] P.J. Low, M.A.J. Paterson, H. Puschmann, A.E. Goeta, J.A.K. Howard, C. Lambert, J.C. Cherryman, D.R. Tackley, S. Leeming, B. Brown, Chem. Eur. J. 10 (2004) 83.

[9] P.J. Low, M.A.J. Paterson, A.E. Goeta, D.S. Yufit, J.A.K. Howard, J.C. Cherryman, D.R. Tackley, B. Brown, J. Mater. Chem. 14 (2004) 2516.

[10] P.J.Low, M.A.J. Paterson, D.S. Yufit, J.A.K. Howard, J.C. Cherryman, D.R. Tackley, R. Brook, B. Brown, J. Mater. Chem. 15 (2005) 2304.

[11] C. Adachi, T. Tsutsui, S. Saito, Appl. Phys. Lett. 55 (1989) 1489.

[12] K. Sugiyama, D. Yoshimura, T. Miyamae, T. Miyazaki, H. Ishii, Y. Ouchi, K. Seki, J. Appl. Phys. 83 (1998) 4928.

[13] H. Ishii, K. Sugiyama, E. Ito, K. Seki, Adv. Mater. 11 (1999) 605.

[14] A. Lesage, M. Bardet, L. Emsley, J. Am. Chem. Soc. 121 (1999) 10987.

[15] H. Kaji, K. Schmidt-Rohr, Macromolecules 34 (2001) 7368.

[16] H. Kaji, K. Schmidt-Rohr, Macromolecules 35 (2002) 7993.

[17] D. Sakellariou, S. P. Brown, A. Lesage, S. Hediger, M. Bardet, C.A. Meriles, A. Pines, L. Emsley, J. Am. Chem. Soc. 125 (2003) 4376.

[18] H.Kaji, Y. Kusaka, G. Onoyama, F. Horii, Jpn. J. Appl. Phys. 44 (2005) 3706.

[19] S. Cadars, A. Lesage, L. Emsley, J. Am. Chem. Soc. 127 (2005) 4466.

[20] H. Kaji, Y. Kusaka, G. Onoyama, F. Horii, J. Am. Chem. Soc. 128 (2006) 4292.

[21] C.Y. Yang, J.G. Hu, A. J. Heeger, J. Am. Chem. Soc. 128 (2006) 12007.

[22] G.C. Levy, R.L. Lichter, ^{15}N Nuclear Magnetic Spectroscopy, John Wiley & Sons, New York, 1979.

[23] E.Y. Chekmenev, Q.W. Zhang, K.W. Waddell, M.S. Mashuta, R.J. Wittebort, J. Am. Chem. Soc. 126 (2004) 379.

[24] A. D. Becke, Phys. Rev. A 38 (1988) 3098.

[25] A. D. Becke, J. Chem. Phys. 98 (1993) 5648.

[26] A. D. Becke, J. Chem. Phys. 98 (1993) 1372.

[27] C.T. Lee, W.T. Yang, R.G. Parr, Phys. Rev. B 37 (1988) 785.

[28] K. Sakanoue, M. Motoda, M. Sugimoto, S. Sakaki, J. Phys. Chem. A 103 (1999) 5551.

[29] M. Malagoli, J.L. Brédas, Chem. Phys. Lett. 327 (2000) 13.

[30] J. Cornil, N.E. Gruhn, D.A. dos Santos, M. Malagoli, P.A. Lee, S. Barlow, S. Thayumanavan, S.R. Marder, N.R. Armstrong, J.L. Brédas, J. Phys. Chem. A 105 (2001) 5206.

[31] M. Malagoli, M. Manoharan, B. Kippelen, J. L. Brédas, Chem. Phys. Lett. 354 (2002) 283.

[32] B.C. Lin, C.P. Cheng, Z.P.M. Lao, J. Phys. Chem. A 107 (2003) 5241.

[33] R. Ditchfield, Mol. Phys. 27 (1974) 789.

[34] K. Wolinski, J.F. Hinton, P. Pulay, J. Am. Chem. Soc. 112 (1990) 8251.

[35] G. Rauhut, S. Puyear, K. Wolinski, P. Pulay, J. Phys. Chem. 100 (1996) 6310.

[36] M.J. Frisch et al., GAUSSIAN 98 (Revision A.11), Gaussian, Pittsburgh, PA, 2001.

[37] Y. Zhang, H. Sun, E. Oldfield, J. Am. Chem. Soc.127 (2005) 3652.

[38] H. Kaji, T. Yamada, N, Tsukamoto, F. Horii, Chem. Phys. Lett. 401 (2005) 246.

[39] T. Yamada, H. Kaji, J. Mol. Struct. 927 (2009) 82.

[40] L.R. Becerra, G.J. Gerfen, R.J. Temkin, D.J. Singel, R.G. Griffin, Phys. Rev. Lett. 71 (1993) 3561.

[41] T. Maly1, G.T. Debelouchina, V.S. Bajaj, K.N. Hu1, C.G. Joo, M.L. Mak-Jurkauskas, J.R. Sirigiri, P.C.A. van der Wel, J. Herzfeld, R.J. Temkin, R.G. Griffin, J. Chem. Phys. 128 (2008) 052211.

Chapter 5

Percolation Paths for Charge Transports in TPD Studied by Quantum Chemical Calculations

5.1. Introduction

Charge transports in organic materials are of immense interest for device applications such as organic light-emitting diodes (OLEDs) [1,2], organic field effect transistors [3,4], and organic solar cells [5,6], and intensive studies were carried out to understand the charge-transport properties [7-47]. Charge transports in several organic crystals with particularly strong intermolecular interactions were reported to be described by band theory at low temperatures [7,8]. In contrast, organic materials with weak intermolecular interactions, including materials for OLEDs, are known to transport charges by hopping mechanism [9-13]. As described in Chapter 1, the rate constant, k_{CT}, for Marcus-type charge transfer is given by Marcus theory [9,10] as

$$k_{CT} = \frac{4\pi^2}{h} H_{AB}^2 \frac{1}{\sqrt{4\pi\lambda k_B T}} \exp(-\frac{\lambda}{4k_B T}) \qquad (5.1)$$

where, λ is the reorganization energy, H_{AB} is the charge transfer integral (or the electronic coupling matrix element) between the relevant two molecules, and T is the temperature. The h and k_B are the Planck and Boltzmann constants, respectively. The parameters of key importance for charge-transfer processes are λ and H_{AB}. The value of λ is the sum of internal and external reorganization energies. The former was quantified by quantum chemical calculations for an isolated molecule [14-17], as the summation of λ_1 and λ_2, both of which are represented by the energy differences as follows.

λ_1 = E (charged state in neutral geometry) – E (charged state in charged geometry) (5.2)

λ_2 = E (neutral state in charged geometry) – E (neutral state in neutral geometry) (5.3)

The external reorganization energy is related to intermolecular interaction and the contribution to the total reorganization energy was considered to be small [18,19].

To quantify H_{AB} values, geometrically symmetric neutral dimers were often considered [20-25]. Halves of the splittings of HOMO and LUMO caused by intermolecular interactions in the dimer system correspond to H_{AB} values for the hole transfer, H_{AB}^{+}, and electron transfer, H_{AB}^{-}, respectively. However, this method is ineffective when the geometry of the dimer is asymmetric and the HOMO or LUMO is unequally distributed between the two molecules. In contrast, the following equations provide the H_{AB}^{+} value, irrespective of the symmetry.

$$\begin{vmatrix} \alpha_A - E & \beta - ES \\ \beta - ES & \alpha_B - E \end{vmatrix} = 0 \tag{5.4}$$

Here, α_A = $<\Phi^A_{HOMO}|\mathbf{H}|\Phi^A_{HOMO}>$, α_B = $<\Phi^B_{HOMO}|\mathbf{H}|\Phi^B_{HOMO}>$, β = $<\Phi^A_{HOMO}|\mathbf{H}|\Phi^B_{HOMO}>$, S = $<\Phi^A_{HOMO}|\Phi^B_{HOMO}>$, and E is the energy. **H** is the electronic Hamiltonian. Φ^A_{HOMO} and Φ^B_{HOMO} are HOMOs of isolated molecules, A and B, respectively. Noting that Φ^A and Φ^B are a non-orthogonal basis set, an effective electronic coupling value, H_{AB}^{+}, is given by Eq. 5.5 through Löwdin's transformation [26,48].

$$H_{AB}^{+} = \frac{\beta - \frac{\alpha_A + \alpha_B}{2} S}{1 - S^2} \tag{5.5}$$

For the calculations of H_{AB}^{-} values, LUMOs of isolated molecules, Φ^{A}_{LUMO} and Φ^{B}_{LUMO}, are used instead of Φ^{A}_{HOMO} and Φ^{B}_{HOMO}.

Until now, the evaluations of H_{AB} values were performed for several asymmetric organic molecular pairs [27-30]. However, the evaluations of H_{AB} values for OLEDs materials were not carried out, except for tris(8-hydroxyqunoline) aluminum(III) (Alq_3) [30]. To estimate H_{AB} values for materials in OLEDs, investigations of the amorphous structures are desired; however, they are difficult to access so far. Therefore, in Ref. 30, the β-Alq_3 crystalline structure was used for the calculations of H_{AB}, assuming that the relative geometries of molecular pairs in the amorphous state are similar to those in the β-crystalline state.

In this Chapter, charge transports in *N*,*N*'-diphenyl-*N*,*N*'-di(*m*-tolyl)benzidine (TPD) (Fig. 5.1) are focused on, considering "percolation paths" for charge transports. TPD is a well-known hole-transport material for OLEDs [2,31-45]. Its reorganization energies for hole-transfer, λ^{+}, and electron-transfer, λ^{-}, were evaluated by density functional theory (DFT) calculations, revealing that the value of λ^{+} (0.28 or 0.29 eV) is smaller than that of λ^{-} (0.56 eV) [15,16]. The calculations result in the ratio of the hole-transfer rate constant and electron-transfer rate constant, k_{CT}^{+} / k_{CT}^{-}, of 21 when we assume $H_{AB}^{+} = H_{AB}^{-}$ in Eq. 5.1 [16]. The value was used to qualitatively explain the results of time-of-flight experiments [37,45] that TPD is superior for hole transports. However, the experimental results, that the electron mobility of TPD is a few or several orders of magnitude smaller than the hole mobility [37,45], cannot be explained by the ratio, $k_{CT}^{+} / k_{CT}^{-} = 21$. To quantify the k_{CT} values and to understand its charge-transport property in more detail, the estimation of H_{AB} values is inevitable. In this Chapter, the H_{AB} values are evaluated using relative intermolecular geometries in TPD crystals as in the above case of Alq_3, because there are also no data concerning the amorphous structure of TPD, except for the intramolecular structural parameters [44]. For TPD crystals, two different polymorphs, orthorhombic [41] and monoclinic [42], were reported. The H_{AB} values

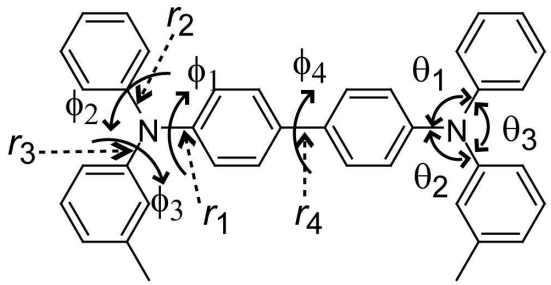

Fig. 5.1. The chemical structure of TPD. The θ, ϕ, and *r* represent respective bond angles, torsion angles, and bond lengths, respectively.

Table 5.1. Optimized parameters of TPD in its neutral, cationic, and anionic states. The parameters are defined in Fig. 5.1.

	θ_1 / °	θ_2 / °	θ_3 / °	ϕ_1 / °	ϕ_2 / °	ϕ_3 / °	ϕ_4 / °	r_1 / Å	r_2 / Å	r_3 / Å	r_4 / Å
neutral	120	120	120	41.0	41.3	42.5	35.8	1.42	1.42	1.42	1.48
cation	121	121	118	26.1	48.8	49.2	20.6	1.39	1.43	1.43	1.46
anion	119	119	122	61.4	31.3	31.7	8.7	1.44	1.41	1.41	1.44

Table 5.2. Reorganization energies of TPD for hole and electron transfers calculated by DFT B3LYP/6-31G(d) and extended Hückel levels.

		λ_1 / eV	λ_2 / eV	λ (= $\lambda_1 + \lambda_2$) / eV	k_{CT}^{+} / k_{CT}^{-} [a]
DFT	hole	0.131	0.141	0.272	27
	electron	0.305	0.269	0.574	
	hole[b]	0.13	0.15	0.28	21
	electron[b]	0.27	0.29	0.56	
extended Hückel	hole	0.031	0.117	0.148	20
	electron	0.280	0.124	0.404	

[a] Based on Eq. 5.1 at T = 300 K, neglecting the difference of the values of H_{AB}^{+} and H_{AB}^{-}.

[b] The values are taken from Ref. 16.

for both the polymorphs are calculated. To understand the charge transports in devices, percolated charge-transport paths between the electrodes should be considered. Therefore, the percolation paths for charge transports, which consist of consecutive molecular pairs with large k_{CT} values, are also investigated. Only when percolation paths do exist, charges can be transported from one electrode to the counter electrode by hopping mechanism.

5.2. Computational Section

The molecular structures of TPD in its neutral, cationic and anionic states were optimized by DFT method using the B3LYP functional, which employs the gradient correction of the exchange functional with three parameters by Becke [49,50] and the correlation functional by Lee, Yang, and Parr [51]. The 6-31G(d) basis set was used. The values of λ^+ and λ^- were calculated for the DFT-optimized structures by both B3LYP/6-31G(d) and extended Hückel levels. As described above, the contribution of the external reorganization energy to the total reorganization energy was considered to be small [18,19], and neglected [14-16,19]. According to these preceding studies, only the internal reorganization energy is considered in the calculations of the reorganization energy.

For the calculations of H_{AB} values, the packing structures in the orthorhombic and monoclinic polymorphs of TPD described in Refs. 41 and 42, respectively, were used. All the pairs of neighboring two molecules were taken from respective polymorphs, and the values of H_{AB} were calculated for the pairs from Eq. 5.5, using the values of α, β, and S. The calculations of H_{AB}^+ and H_{AB}^- values by *ab intio* methods were sometimes failed [25] and semi-empirical calculations were often performed [21-26]. Following these preceding studies, we used extended Hückel method to calculate H_{AB} values. Note that if the S values are ignored as in the Marcus-approximation, the H_{AB} values equal to β values. In contrast, extended Hückel method dose not ignore the S values. Here, the H_{AB} values were calculated, considering all of the α, β, and S values. All the calculations were carried out with Gaussian 03 program [52].

5.3. Results and Discussion

5.3.1. Reorganization Energies

For the reorganization energy calculations, TPD in the neutral, cationic, and anionic states were optimized by DFT method. Important optimized parameters, the bond angles, θ_1, θ_2, and θ_3, the torsion angles, ϕ_1, ϕ_2, ϕ_3, and ϕ_4, and the bond lengths, r_1, r_2, r_3, and r_4 (see Fig. 5.1), are listed in Table 5.1. The magnitude of geometrical change by anionization is larger than that by cationization, especially concerning the torsion angles. Table 5.2 shows the calculated λ values. Reflecting the geometrical change between the neutral and charged states, the λ^- value was calculated to be larger than λ^+ value for both the DFT and extended Hückel calculations. The DFT-calculated λ values in this study are almost consistent with a previous report [16] as shown in Table 5.2. Although the extended Hückel calculations provide smaller λ values for both the hole and electron transports, the values of k_{CT}^+ / k_{CT}^- at 300 K under the assumption of $H_{AB}^+ = H_{AB}^-$, are almost consistent between the DFT and the extended Hückel results; hole-transfer rate constants are 20-30 times larger than the electron-transfer rate constants.

5.3.2. Frontier Orbitals

Fig. 5.2 illustrates the HOMO and LUMO of TPD in the neutral state calculated at DFT B3LYP/6-31G(d) and extended Hückel levels for the above DFT-optimized geometry. Table 5.3 shows the square of the MO coefficients of respective segments in percentage. In Table 5.3, the respective segments, the nitrogen, biphenylene, phenyl, and tolyl moieties, are represented as "N," "BP," "Ph," and "To," respectively. The subscript of "$_L$" or "$_R$" means left or right part of the molecule in Fig. 5.2. For example, "N_L" indicates the left nitrogen of the molecule. For the HOMO, the DFT and extended Hückel results are almost equivalent. The contributions from one nitrogen, N_X, ($_X$ = $_L$ or $_R$) and one benzene-ring in biphenylene parts,

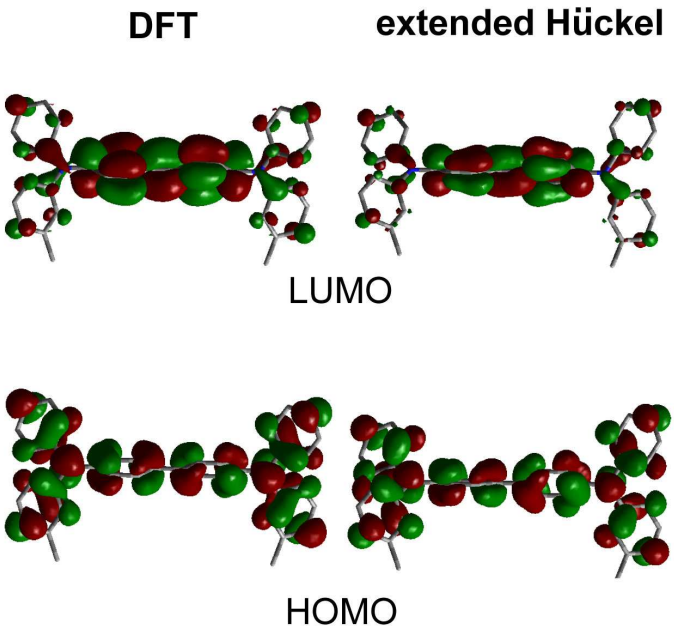

Fig. 5.2. The HOMO and LUMO of TPD calculated by DFT B3LYP/6-31G(d) and extended Hückel methods for the DFT-optimized geometry. The value for the surfaces is 0.02 a.u.

Table 5.3. Contributions of the nitrogen (N), biphenylene (BP), phenyl (Ph), and tolyl (To) moieties of TPD to the HOMO and LUMO calculated by DFT B3LYP/6-31G(d) and extended Hückel calculations. The subscript of "$_L$" or "$_R$" indicates the left or right side of the molecule in Fig. 5.2.

		N_L	N_R	BP_L	BP_R	Ph_L	Ph_R	To_L	To_R
DFT	HOMO	15.0	15.0	17.4	16.1	9.0	8.9	9.3	9.3
	LUMO	0.6	0.5	36.8	35.9	6.6	6.2	6.7	6.7
extended Hückel	HOMO	14.7	14.7	17.8	17.8	8.7	8.7	8.7	8.7
	LUMO	0.5	0.5	42.6	42.6	3.7	3.7	3.1	3.1

BP_X, are 15 and 16-18%, respectively. The contributions from one benzene-ring in phenyl, Ph_X, and tolyl, To_X, are 9% for both the moieties. On the other hand, the LUMO is more localized on the biphenylene part and contributions from the other parts are notably small, although some difference is found between the DFT and extended Hückel results for the LUMO. For the extended Hückel calculations, the contribution from BP_X is 42.6%, whereas those from N_X, Ph_X, and To_X, are 0.5, 3.7, and 3.1%, respectively.

5.3.3. Molecular Pairs in TPD Crystals

Figs. 5.3a and 5.3b show the unit cell of TPD in the orthorhombic and monoclinic polymorphs reported by Kennedy et al. [41] and Zhang et al. [42], respectively. Four molecules in respective unit cells are designated as I, II, III, and IV. The cell in Fig. 5.3 are defined as cell (000), and neighboring cells at the +a, -a, +b, -b, +c, and -c directions are represented as (100), (-100), (010), (0-10), (001), and (00-1), respectively. We refer to a molecule X (X = I, II, III, or IV) in the cell (abc) (a, b, c = -1, 0, or 1) as X(abc). For example, I(000) denotes molecule I in the cell (000). In the orthorhombic polymorph, as shown in Table 5.4, I(000) is surrounded by two molecules of I, four molecules of II, two molecules of III, and eight molecules of IV. Except for the above pairs between I and II, II(000) is surrounded by two molecules of II, eight molecules of III, and two molecules of IV. Also except for above pairs between I and III, and II and III, III(000) is surrounded by two molecules of III and four molecules of IV. As the rest, IV(000) is sandwiched by two molecules of IV. In total, thirty-six pairs, numbered from 1 to 36 in Table 5.4, were considered for the calculations of H_{AB} values. Likewise, H_{AB} values were calculated for thirty-six pairs in the monoclinic polymorph, which are numbered from 37 to 72 in Table 5.5.

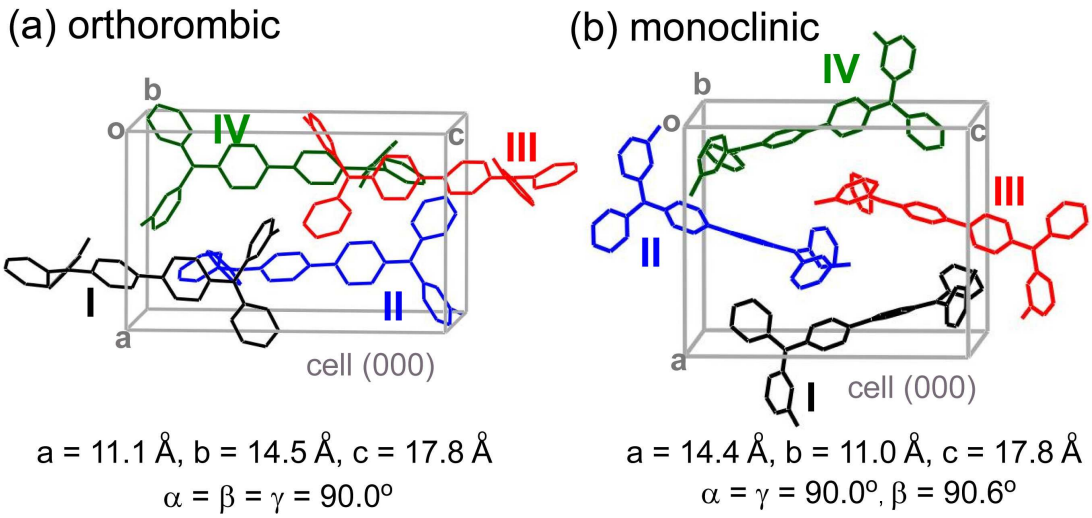

Fig. 5.3. Four molecules classified into the unit cell (000) in (a) orthorhombic and (b) monoclinic polymorphs of TPD. For each polymorph, the molecules are designated as I, II, III, and IV.

Table 5.4. Molecular pairs in the ***orthorhombic*** polymorph of TPD.

Pairs with I(000)

I	II	III	IV	
1. I(001)	3. II(000)	7. III(00-1)	9. IV(000)	13. IV(1-10)
2. I(00-1)	4. II(0-10)	8. III(10-1)	10. IV(100)	14. IV(10-1)
	5. II(00-1)		11. IV(0-10)	15. IV(0-1-1)
	6. II(0-1-1)		12. IV(00-1)	16. IV(1-1-1)

Pairs with II(000)

I	II	III		IV
-	17. II(001)	19. III(000)	23. III(110)	27. IV(000)
	18. II(00-1)	20. III(100)	24. III(10-1)	28. IV(100)
		21. III(010)	25. III(01-1)	
		22. III(00-1)	26. III(11-1)	

Pairs with III(000)

I	II	III	IV	
-	-	29. III(001)	31. IV(000)	33. IV(001)
		30. III(00-1)	32. IV(0-10)	34. IV(0-11)

Pairs with IV(000)

I	II	III	IV
-	-	-	35. IV(001)
			36. IV(00-1)

Table 5.5. Molecular pairs in the ***monoclinic*** polymorph of TPD.

Pairs with I(000)

I	II	III		IV
37. I(001)	39. II(000)	43. III(000)	47. III(110)	51. IV(100)
38. I(00-1)	40. II(100)	44. III(100)	48. III(10-1)	52. IV(110)
	41. II(001)	45. III(010)	49. III(01-1)	
	42. II(101)	46. III(00-1)	50. III(11-1)	

Pairs with II(000)

I	II	III	IV	
-	53. II(001)	55. III(00-1)	57. IV(000)	61. IV(110)
	54. II(00-1)	56. III(01-1)	58. IV(100)	62. IV(10-1)
			59. IV(010)	63. IV(01-1)
			60. IV(00-1)	64. IV(11-1)

Pairs with III(000)

I	II	III	IV	
-	-	65. III(001)	67. IV(000)	69. IV(001)
		66. III(00-1)	68. IV(100)	70. IV(101)

Pairs with IV(000)

I	II	III	IV
-	-	-	71. IV(001)
			72. IV(00-1)

5.3.4. *"Hole"* Transports in Orthorhombic TPD

The H_{AB}^{+} values for the orthorhombic polymorph are represented in Fig. 5.4a as filled squares. The H_{AB}^{+} values are notably large for the pairs of 7 (I(000)-III(00-1)), 8 (I(000)-III(10-1)), 27 (II(000)-IV(000)), and 28 (II(000)-IV(100)). Since all these pairs are geometrically equivalent, their H_{AB}^{+} values are the same, 6.4 meV. The pairs are illustrated in Fig. 5.5a. The second largest H_{AB}^{+} values are for the pairs of 4 (I(000)-II(0-10)), 6 (I(000)-II(0-1-1)), 31 (III(000)-IV(000)), and 33 (III(000)-IV(001)). They are also geometrically equivalent with each other, and all the H_{AB}^{+} value are 4.5 meV. Fig. 5.5b shows the pairs. For the remaining pairs, the values are $6.4 \times 10^{-2} - 1.8$ meV.

By using the H_{AB}^{+} values, the k_{CT}^{+} values were calculated at T = 300 K, according to Eq. 5.1. Here, the above-mentioned λ^{+} value of 0.148 eV were used. The results are shown in Fig. 5.4b as filled squares. The k_{CT}^{+} values are $4.2 \times 10^{7} - 4.3 \times 10^{11}$ s^{-1}. The maximum value is for the pairs of 7, 8, 27, and 28, reflecting their large H_{AB}^{+} values. It can be expected that holes are favorably transported along the a-axis through the periodic pairs of 7 and 8, or 27 and 28, as shown in Fig. 5.5a. The k_{CT}^{+} values in the pairs of 4, 6, 31, and 33 are also in the same order, 10^{11} s^{-1}. Using the periodic pairs of 4 and 6, or 31 and 33, holes can transfer macroscopically along the c-axis (see Fig. 5.5b). Combinations of the pairs in Figs. 5.5a and 5.5b can be also used for effective hole-transport paths in the a-c plane. For hole transports in the b-direction, the pairs of 3, 4, 5, and 6, or 31, 32, 33, and 34 can be used as shown in Fig. 5.6. The k_{CT}^{+} values for the pairs of 3, 5, 32, and 34 are smaller than those for the pairs of 7 and 4 by about one order of magnitude. Therefore, the hole transports along the b-axis are expected to be ineffective compared with those along the a- and c-axes.

From the calculations, the values of S in Eq. 5.5 were found to be small, which results in $1 >> S^2$. Therefore, Eq. 5.5 can be reduced to $H_{AB}^{+} = |\beta - \alpha S|$. Moreover, H_{AB}^{+} is found to be almost proportional to β, due to the well-known relation, $\beta \cong K\alpha S$, where K (= 1.75) is a Wolfsberg-Helmholz constant [53,54]. Therefore, the contribution of respective segments, the

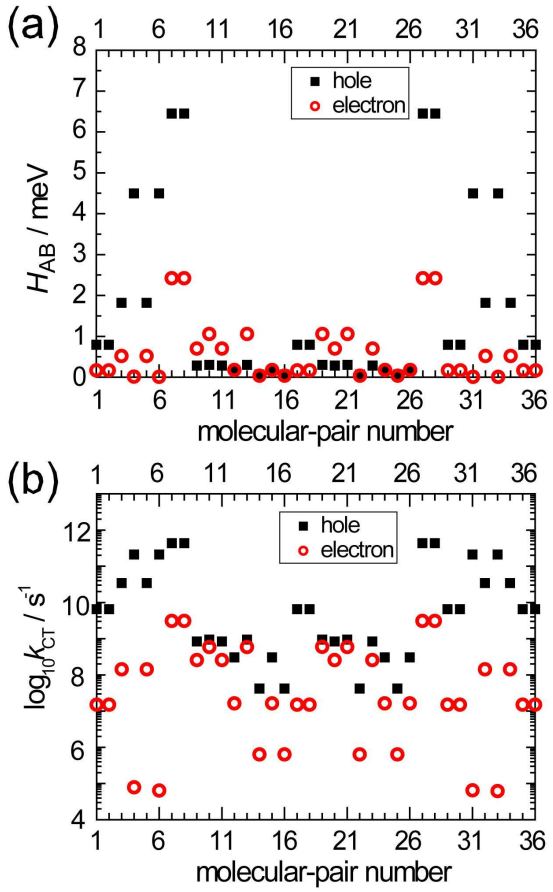

Fig. 5.4. (a) The values of hole transfer integrals, H_{AB}^{+} (■), and electron transfer integrals, H_{AB}^{-} (○), calculated by extended Hückel method for the thirty-six molecular pairs in the orthorhombic polymorph of TPD. (b) The values of hole-transfer rate constants, k_{CT}^{+} (■), and electron-transfer rate constants, k_{CT}^{-} (○), at 300 K calculated using the H_{AB} values in (a). For the calculations, the reorganization energies of λ^{+} = 0.148 and λ^{-} = 0.404 eV were used, which were also calculated by extended Hückel method.

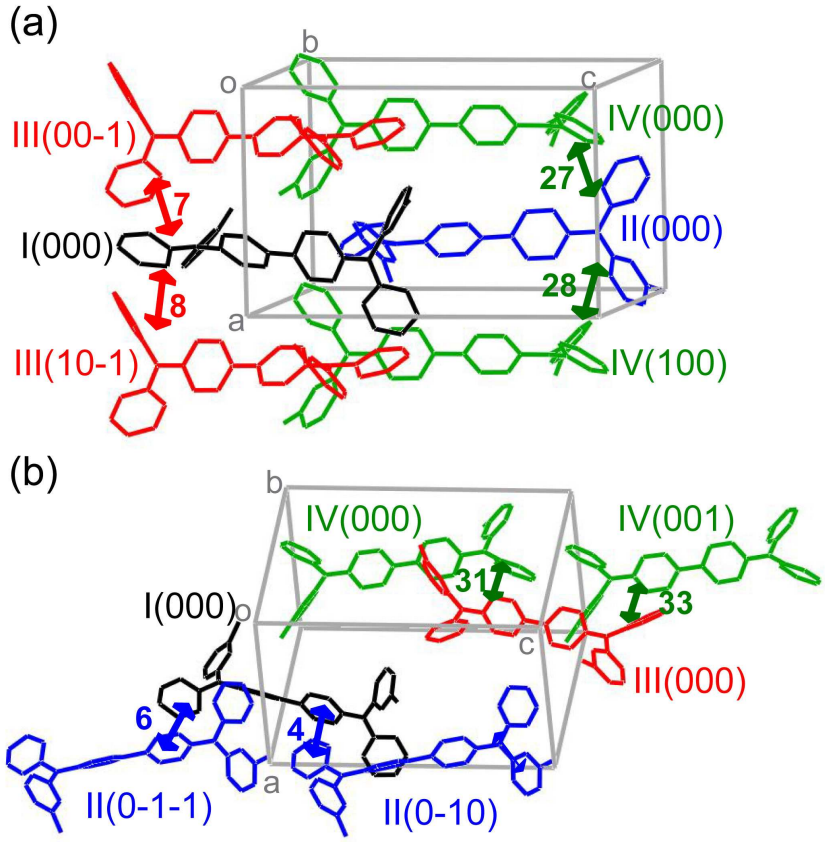

Fig. 5.5. (a) Representations of the molecular pairs with the largest hole-transfer rate constant in the orthorhombic polymorph, 7 (I(000)-III(00-1)), 8 (I(000)-III(10-1)), 27 (II(000)-IV(000)), and 28 (II(000)-IV(100)). Percolation paths for hole transports along the a-axis can be formed by the periodic pairs of 7 and 8, or 27 and 28. (b) The pairs with relatively large hole-transfer rate constants, 4 (I(000)-II(0-10)), 6 (I(000)-II(0-1-1)), 31 (III(000)-IV(000)), and 33 (III(000)-IV(001)). The periodic pairs of 4 and 6, or 31 and 33 can be percolation paths for hole transports along the c-axis.

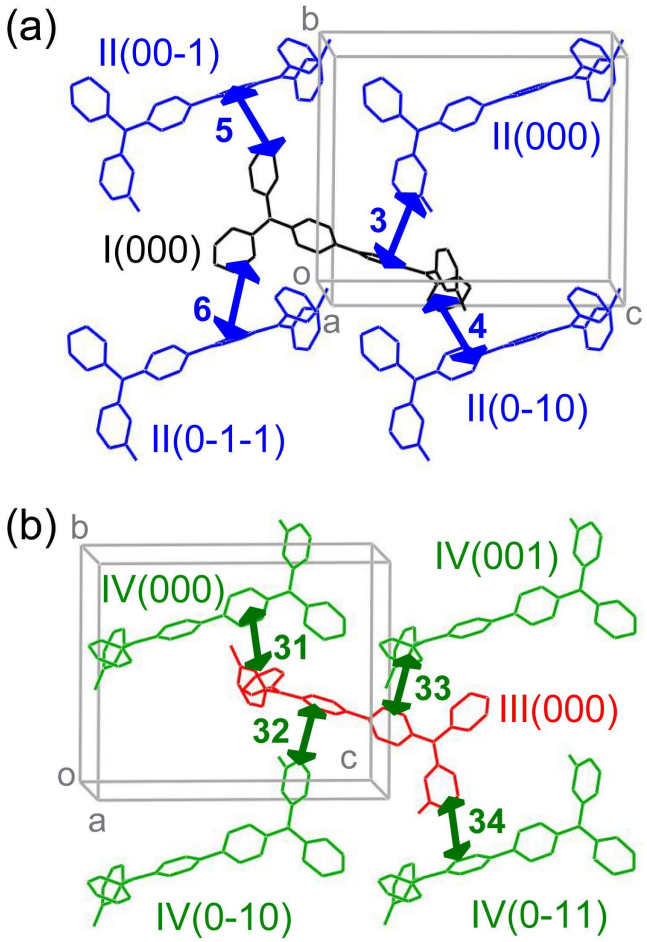

Fig. 5.6. Molecular pairs of (a) 3 (I(000)-II(000)), 4 (I(000)-II(0-10)), 5 (I(000)-II(00-1)), and 6 (I(000)-II(0-1-1)) and (b) 31 (III(000)-IV(000)), 32 (III(000)-IV(0-10)), 33 (III(000)-IV(001)), and 34 (III(000)-IV(0-11)) in the orthorhombic polymorph of TPD. These molecular pairs can convey holes in the direction of the b-axis.

nitrogen, biphenylene, phenyl, and tolyl, for the H_{AB}^{+} values can be investigated. We call it "*segmental β values*", which can be calculated by $<\Phi^{segA}_{HOMO}|\mathbf{H}|\Phi^{segB}_{HOMO}>$. Here, Φ^{segA}_{HOMO} and Φ^{segB}_{HOMO} are linear combinations of atomic orbitals in the respective segments of the molecules A and B. Tables 5.6 and 5.7 summarize the segmental β values for hole transfer, β^{+}, for respective segmental pairs in the pair of 7 and 4, respectively. Both the positive and negative values appear in the tables, but the signs are not important and the absolute values are compared in the following discussion.

It is found from Table 5.6 that the following segmental pairs provide large segmental $|\beta^{+}|$ values for the pair 7; i) the pair of Ph_L of I(000) and Ph_L of III(00-1), ii) that of To_L of I(000) and Ph_L of III(00-1), and iii) that of To_R of I(000) and To_R of III(00-1). For the pair 4, as shown in Table 5.7, followings are notable; the pair of BP_R of I(000) and Ph_L of II(0-10), ii) that of Ph_R of I(000) and BP_L of II(0-10), iii) that of To_R of I(000) and BP_L of II(0-10), and iv) that of To_R of I(000) and BP_R of II(0-10). Tables 5.6 and 5.7 also show the inter-segment distances. Some shortest distances in the pairs of 7 and 4 are shown in Figs. 5.7a and 5.7b, respectively. It is found that segment pairs with short inter-segment distances generally provide large segmental $|\beta^{+}|$ values. Note that the inter-segment distances in Tables 5.6 and 5.7 are the shortest internuclei distances (here, the hydrogen nuclei are neglected). When the centers of gravity of each segment are used as the inter-segment distance instead, distinct relationship between the segmental $|\beta^{+}|$ value and the inter-segment distance was not found. The details are described in Chapter 6. Although the inter-segment distance is one of the most crucial factors to provide large segmental $|\beta^{+}|$ values, they are also affected by other factors. For example, relatively large segmental $|\beta^{+}|$ value of 1.6 meV is found for To_L of I(000) and BP_L of III(00-1) in the pair 7 (the inter-segment distance is 4.1 Å). In contrast, the pair of To_R of I(000) and Ph_R of III(00-1) provides only 0.3 meV, although the inter-segment distance is as

Table 5.6. The segmental β values for charge transfer and shortest inter-segment C-C, C-N, or N-N distances in the molecular pair **7**, I(000)-III(00-1). The respective contributions from the nitrogen (N), biphenylene (BP), phenyl (Ph), and tolyl (To) moieties in the left ($_L$) and right ($_R$) sides of TPD molecules in Fig. 5.7a are shown.

		III(00-1)							
		N_L	N_R	BP_L	BP_R	Ph_L	To_L	Ph_R	To_R
Segmental β^+ / meV									
I(000)	N_L	0.0	0.0	-1.2	0.0	0.3	0.0	0.0	0.0
	N_R	0.0	0.0	0.0	0.0	0.0	0.0	0.0	0.0
	BP_L	0.0	0.0	-0.8	-0.4	0.0	0.0	0.0	0.0
	BP_R	0.0	-0.2	0.0	-0.9	0.0	0.0	0.2	0.6
	Ph_L	0.0	0.0	0.3	0.0	-3.8	0.0	0.0	0.0
	To_L	0.0	0.0	1.6	0.0	-5.7	0.0	0.0	0.0
	Ph_R	0.0	0.0	0.0	0.0	0.0	0.0	0.0	0.0
	To_R	0.0	0.1	0.0	0.0	0.0	0.0	0.3	-3.6
Segmental β^- / meV									
I(000)	N_L	0.0	0.0	-0.2	0.0	-0.1	0.0	0.0	0.0
	N_R	0.0	0.0	0.0	0.0	0.0	0.0	0.0	0.0
	BP_L	0.0	0.0	1.3	-5.0	0.0	0.0	0.0	0.0
	BP_R	0.0	-0.1	0.0	-0.5	0.0	0.0	0.1	0.4
	Ph_L	0.0	0.0	0.0	0.0	0.2	0.0	0.0	0.0
	To_L	0.0	0.0	-0.4	0.0	0.0	0.0	0.0	0.0
	Ph_R	0.0	0.0	0.0	0.0	0.0	0.0	0.0	0.0
	To_R	0.0	0.0	0.0	0.0	0.0	0.0	0.3	0.4
Inter-segment C-C, C-N, or N-N distances / Å									
I(000)	N_L	5.8	9.3	4.1	6.1	4.6	7.2	9.4	9.8
	N_R	13.7	6.4	10.0	6.8	13.5	14.8	6.1	5.0
	BP_L	6.6	6.4	3.8	4.0	5.7	7.9	6.6	6.6
	BP_R	9.9	4.7	6.4	3.9	9.5	11.2	4.9	3.8
	Ph_L	4.8	10.0	4.0	6.6	3.7	6.1	10.5	10.4
	To_L	5.5	9.4	4.1	6.2	3.6	6.9	9.0	10.2
	Ph_R	14.8	7.8	11.2	8.2	14.5	16.0	7.5	6.2
	To_R	13.5	4.7	9.5	5.9	13.5	14.5	3.8	3.6

Table 5.7. The segmental β Values for charge transfer and shortest inter-segment C-C, C-N, or N-N distances in the molecular pair **4**, I(000)-II(0-10). The respective contributions from the nitrogen (N), biphenylene (BP), phenyl (Ph), and tolyl (To) moieties in the left ($_L$) and right ($_R$) sides of TPD molecules in Fig. 5.7b are shown.

		II(0-10)							
		N_L	N_R	BP_L	BP_R	Ph_L	To_L	Ph_R	To_R
Segmental β^+ / meV									
I(000)	N_L	0.0	0.0	0.0	0.0	0.0	0.0	0.0	0.0
	N_R	0.0	0.0	0.1	0.0	-0.1	0.0	0.0	0.0
	BP_L	0.0	0.0	0.0	0.0	0.0	0.0	0.0	0.0
	BP_R	0.0	0.0	0.0	0.0	-6.1	0.0	0.0	0.0
	Ph_L	0.0	0.0	0.0	0.0	0.0	0.0	0.0	0.0
	To_L	0.0	0.0	0.0	0.0	0.0	0.0	0.0	0.0
	Ph_R	0.0	0.0	-2.9	0.0	0.8	0.0	0.0	0.0
	To_R	0.0	0.0	-4.3	2.7	0.3	0.0	0.0	0.0
Segmental β^- / meV									
I(000)	N_L	0.0	0.0	0.0	0.0	0.0	0.0	0.0	0.0
	N_R	0.0	0.0	0.1	0.0	0.0	0.0	0.0	0.0
	BP_L	0.0	0.0	0.0	0.0	0.0	0.0	0.0	0.0
	BP_R	0.0	0.0	0.0	0.0	0.9	0.0	0.0	0.0
	Ph_L	0.0	0.0	0.0	0.0	0.0	0.0	0.0	0.0
	To_L	0.0	0.0	0.0	0.0	0.0	0.0	0.0	0.0
	Ph_R	0.0	0.0	-1.0	-0.1	-0.2	0.0	0.0	0.0
	To_R	0.0	0.0	0.8	-0.2	-0.2	0.0	0.0	0.0
Inter-segment C-C, C-N, or N-N distances / Å									
I(000)	N_L	12.9	19.4	13.2	16.1	8.7	13.6	19.1	20.1
	N_R	6.2	9.4	4.8	6.45	4.2	7.6	9.3	10.2
	BP_L	9.3	15.2	9.2	11.9	5.4	10.3	14.9	15.9
	BP_R	6.6	10.9	5.7	7.8	3.6	8.0	10.7	11.6
	Ph_L	12.3	19.8	12.9	16.2	8.0	12.7	19.7	20.5
	To_L	14.1	19.8	14.2	16.9	9.9	14.9	19.3	20.6
	Ph_R	5.2	7.5	3.7	4.8	4.1	6.6	8.2	7.8
	To_R	5.6	6.8	3.8	3.8	4.2	6.8	6.3	8.1

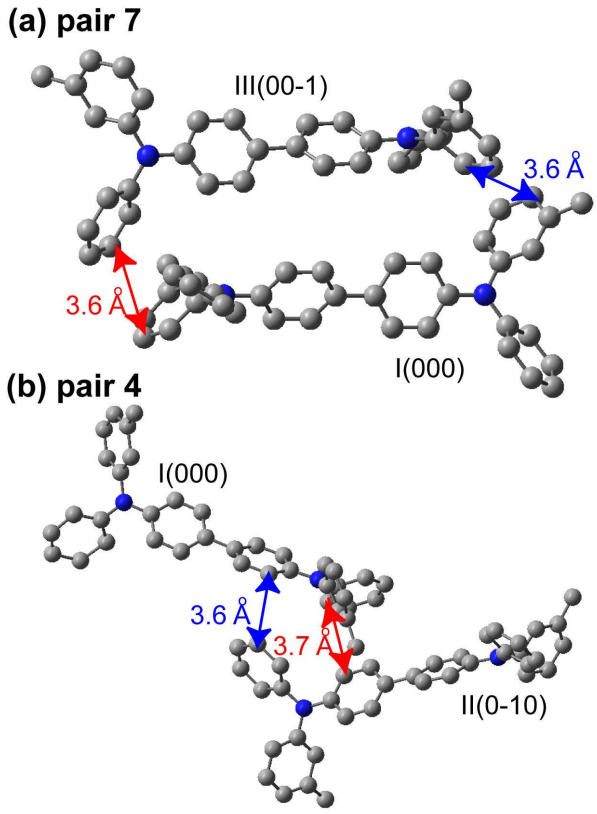

Fig. 5.7. Representations of some shortest inter-segment C-C distances for the molecular pairs of (a) 7 (I(000)-III(00-1)) and (b) 4 (I(000)-II(0-10)).

short as 3.8 Å. One of the other factors, which affect segmental $|\beta^+|$ values, will be relative orientations between the segments. Another factor is the localization of frontier orbitals. The above results suggest that the phenyl and tolyl rings have great significances to the H_{AB}^+ in both the pairs of 7 and 4, originating from the relatively large contributions to the HOMO and the short inter-segment distances. The situation is substantially different for electron transport in spite of the same intermolecular geometry. This is due to the localization of LUMO as shown later.

5.3.5. *"Electron"* Transports in Orthorhombic TPD

Fig. 5.4a also shows the H_{AB}^- values for the orthorhombic polymorph as open circles. It is found that the values are smaller than those for HOMOs; all the values are smaller than 2.4 meV. From the H_{AB}^- values, the k_{CT}^- values in Eq. 5.1 were calculated at T = 300 K, using the λ^- value of 0.404 eV. The results are shown in Fig. 5.4b as open circles. It is clearly shown that the maximum k_{CT}^- value, 3.1×10^9 s^{-1} is two orders of magnitude less than the maximum k_{CT}^+ value. The minimum k_{CT}^- value, 6.2×10^4 s^{-1} is two to three orders smaller compared to the minimum k_{CT}^+ value. The smaller k_{CT}^- values explain the poor electron-transport property of TPD, which is found in this study to originate from the small H_{AB}^- values as well as the large λ^- value.

The segmental β values for the electron transfer, β^-, in the pairs of 7 and 4 are also shown in Tables 5.6 and 5.7, respectively. For the segment pairs with large segmental $|\beta^+|$ values, such as the pair of Ph_L of I(000) and Ph_L of III(00-1), the segmental $|\beta^-|$ values are found to be small, although the relative geometry of the molecular pairs are the same. The difference originates from the difference of HOMO and LUMO; LUMO is localized on the biphenylene part and the contributions of the other segments are small as shown above (see Fig. 5.2 and Table 5.3). Instead, the pair of BP_L of I(000) and BP_R of III(00-1) provides the segmental $|\beta^-|$ value of 5.0

meV, which is larger than that of the corresponding segmental $|\beta^+|$ value, 0.4 meV. This is also due to the localization of LUMO on the biphenylene part.

5.3.6. *"Hole"* Transports in Monoclinic TPD

Filled squares in Fig. 5.8a represent the H_{AB}^+ values for the monoclinic polymorph of TPD. It is found that the values in the pairs of 51 (I(000)-IV(100)), 52 (I(000)-IV(110)), 55 (II(000)-III(00-1)), and 56 (II(000)-III(01-1)) are remarkable. These pairs are shown in Fig. 5.9a. The geometries of the former two pairs, 51 and 52, are equivalent with each other. Also, those of the later two pairs, 55 and 56, are equivalent. The difference between the former two pairs and latter two pairs is slight, which originates from the lower symmetry of the monoclinic polymorph compared with the orthorhombic polymorph. It is also found from Fig. 5.8a that the H_{AB}^+ values for the pairs of 39 (I(000)-II(000)), 41 (I(000)-II(001)), 67 (III(000)-IV(000)), and 69 (III(000)-IV(001)) are relatively large. These pairs are illustrated in Fig. 5.9b. The geometries of the pairs, 39 and 67, are equivalent and those of the pairs, 41 and 69, are also equivalent.

Fig. 5.10 shows the above-mentioned molecular pairs of 51, 55, 39, and 41. It should be noted that the pairs of 51 and 55 (and 52, 56) are similar to the pair 7 (and 8, 27, 28) in the orthorhombic polymorph, as shown in Figs. 5.6 and 5.10. Therefore, large segmental $|\beta^+|$ values are obtained for the same segmental pairs between spatially close Ph_x and/or To_x rings in the pairs of 51, 52, 55, and 56, as in the case of the pair 7 (see Tables 5.8 and 5.9). The pairs of 39 and 41 (and 67, 69) are similar to the pair 4 (and 6, 31, 33) in the orthorhombic polymorph, also as shown in Figs. 5.6 and 5.10. Therefore, as in the case of the pair 4, the dominant contribution for the intermolecular HOMO coupling is provided for the segmental pairs between spatially close BP_x and Ph_x, or BP_x and To_x (see segmental $|\beta^+|$ values in Tables 5.10 and 5.11. The k_{CT}^+ values at T = 300 K are shown in Fig. 5.8b as filled squares. Large k_{CT}^+ values in the

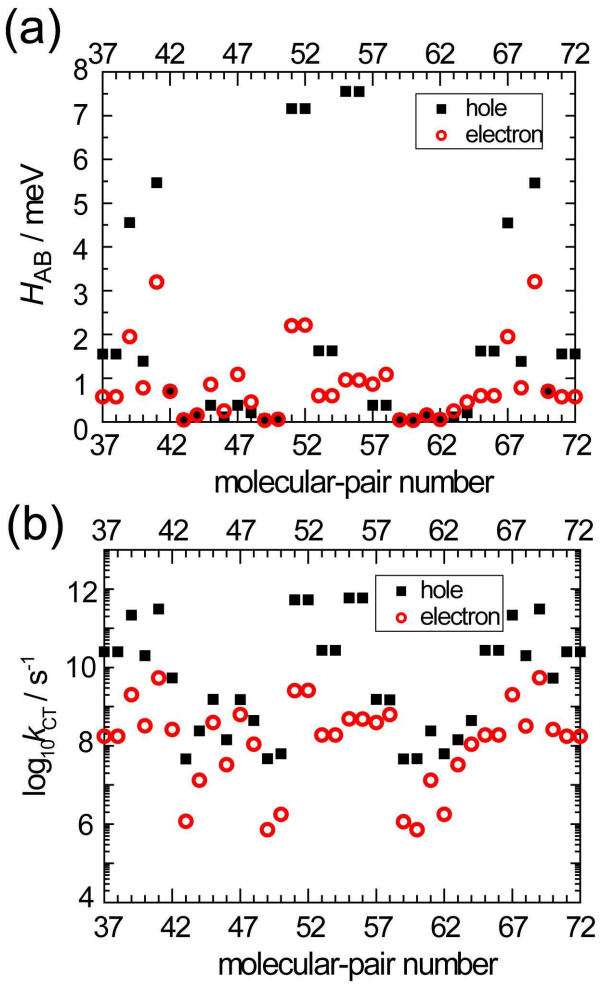

Fig. 5.8. (a) The values of hole transfer integrals, H_{AB}^{+} (■), and electron transfer integrals, H_{AB}^{-} (○), calculated by extended Hückel method for the thirty-six molecular pairs in the monoclinic polymorph of TPD. (b) The values of hole-transfer rate constants, k_{CT}^{+} (■), and electron-transfer rate constants, k_{CT}^{-} (○), at 300 K calculated using the H_{AB} values in (a). For the calculations, the reorganization energies of λ^{+} = 0.148 and λ^{-} = 0.404 eV were used, which were also calculated by extended Hückel method.

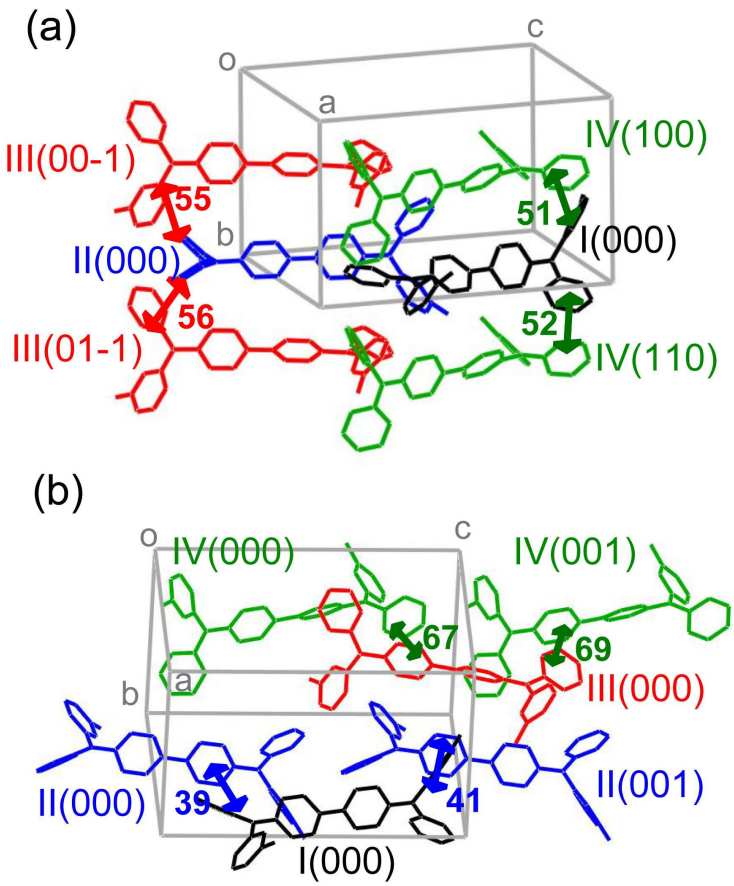

Fig. 5.9. (a) Representations of the molecular pairs with large hole-transfer rate constants in the monoclinic polymorph, 51 (I(000)-IV(100)), 52 (I(000)-IV(110)), 55 (II(000)-III(00-1)), and 56 (II(000)-III(01-1)). Percolation paths for hole transports along the b-axis can be formed by the periodic pairs of 51 and 52, or 55 and 56. (b) The pairs with relatively large hole-transfer rate constants, 39 (I(000)-II(000)), 41 (I(000)-II(001)), 67 (III(000)-IV(000)), and 69 (III(000)-IV(001)). The periodic pairs of 39 and 41, or 67 and 69 can be percolation paths for hole transports along the c-axis.

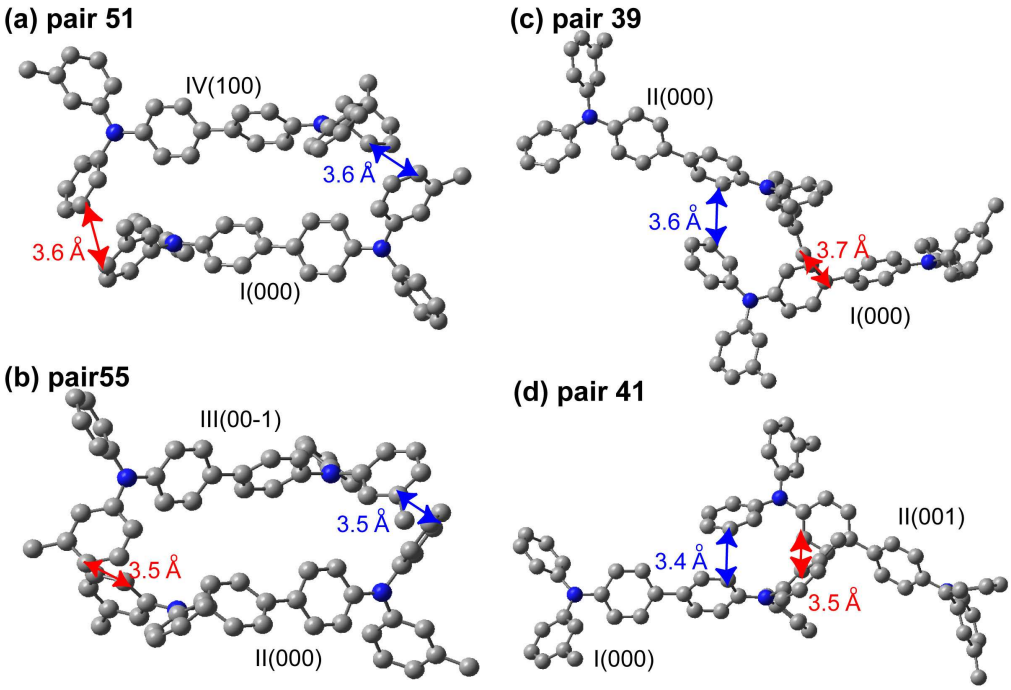

Fig. 5.10. Representations of some shortest inter-segment C-C distance for the molecular pairs of (a) 51 (I(000)-IV(100)), (b) 55 (II(000)-III(00-1)), (c) 39 (I(000)-II(000)), and (d) 41 (I(000)-II(001)).

Table 5.8. The segmental β values for charge transfer and shortest inter-segment C-C, C-N, or N-N distances in the molecular pair **51**, I(000)-IV(100). The respective contributions from the nitrogen (N), biphenylene (BP), phenyl (Ph), and tolyl (To) moieties in the left ($_L$) and right ($_R$) sides of TPD molecules in Fig. 10a are shown.

		IV(100)							
		N_L	N_R	BP_L	BP_R	Ph_L	To_L	Ph_R	To_R
Segmental β^+ / meV									
I(000)	N_L	0.0	0.0	1.3	0.0	-0.3	0.0	0.0	0.0
	N_R	0.0	0.0	0.0	0.0	0.0	0.0	0.0	0.0
	BP_L	0.0	0.0	0.5	0.5	0.0	0.0	0.0	0.0
	BP_R	0.0	0.2	0.0	0.9	0.0	0.0	-0.2	-0.5
	Ph_L	0.0	0.0	0.0	0.0	3.2	0.0	0.0	0.0
	To_L	0.0	0.0	-1.8	0.0	6.0	0.0	0.0	0.0
	Ph_R	0.0	0.0	0.0	0.0	0.0	0.0	0.0	0.0
	To_R	0.0	-0.1	0.0	0.0	0.0	0.0	1.3	3.9
Segmental β^- / meV									
I(000)	N_L	0.0	0.0	-0.2	0.0	0.0	0.0	0.0	0.0
	N_R	0.0	0.0	0.0	0.0	0.0	0.0	0.0	0.0
	BP_L	0.0	0.0	1.5	-5.1	0.0	0.0	0.0	0.0
	BP_R	0.0	0.0	0.0	-0.9	0.0	0.0	0.0	0.2
	Ph_L	0.0	0.0	0.1	0.0	0.6	0.0	0.0	0.0
	To_L	0.0	0.0	-0.3	0.0	0.3	0.0	0.0	0.0
	Ph_R	0.0	0.0	0.0	0.0	0.0	0.0	0.0	0.0
	To_R	0.0	0.0	0.0	0.0	0.0	0.0	0.3	0.4
inter-segment C-C, C-N, or N-N distances / Å									
I(000)	N_L	5.7	9.3	4.1	6.1	4.6	7.1	9.5	9.8
	N_R	13.6	6.3	9.9	6.7	13.4	14.8	6.1	4.9
	BP_L	6.5	6.4	3.7	4.0	5.7	7.8	6.7	6.6
	BP_R	9.8	4.7	6.3	3.8	9.4	11.1	4.9	3.9
	Ph_L	4.8	10.1	4.0	6.7	3.7	6.0	10.6	10.4
	To_L	5.4	9.4	4.0	6.2	3.6	6.8	9.1	10.2
	Ph_R	14.8	7.7	11.1	8.1	14.5	16.0	7.5	6.2
	To_R	13.4	4.6	9.4	5.8	13.4	14.4	3.7	3.6

Table 5.9. The segmental β values for charge transfer and shortest inter-segment C-C, C-N, or N-N distances in the molecular pair **55**, II(000)-III(00-1). The respective contributions from the nitrogen (N), biphenylene (BP), phenyl (Ph), and tolyl (To) moieties in the left ($_L$) and right ($_R$) sides of TPD molecules in Fig. 10b are shown.

		III(00-1)							
		N_L	N_R	BP_L	BP_R	Ph_L	To_L	Ph_R	To_R
Segmental β^+ / meV									
II(000)	N_L	0.0	0.0	-0.2	0.0	0.0	0.1	0.0	0.0
	N_R	0.0	0.0	0.0	0.0	0.0	0.0	0.0	0.0
	BP_L	0.0	0.0	-0.8	-0.5	0.0	0.0	0.0	0.0
	BP_R	0.0	-1.2	0.0	-0.5	0.0	0.0	0.1	1.8
	Ph_L	0.0	0.0	0.2	0.0	0.0	-0.2	0.0	0.0
	To_L	0.0	0.0	0.8	0.0	0.0	-5.3	0.0	0.0
	Ph_R	0.0	0.3	0.0	0.0	0.0	0.0	-2.7	-7.6
	To_R	0.0	0.0	0.0	0.0	0.0	0.0	0.0	0.0
Segmental β^- / meV									
II(000)	N_L	0.0	0.0	0.0	0.0	0.0	0.0	0.0	0.0
	N_R	0.0	0.0	0.0	0.0	0.0	0.0	0.0	0.0
	BP_L	0.0	0.0	-0.7	-4.2	0.0	0.0	0.0	0.0
	BP_R	0.0	-0.1	0.0	1.7	0.0	0.0	0.1	0.0
	Ph_L	0.0	0.0	-0.1	0.0	0.0	0.0	0.0	0.0
	To_L	0.0	0.0	0.3	0.0	0.0	0.6	0.0	0.0
	Ph_R	0.0	0.0	0.0	0.0	0.0	0.0	0.5	0.7
	To_R	0.0	0.0	0.0	0.0	0.0	0.0	0.0	0.0
inter-segment C-C, C-N, or N-N distances / Å									
II(000)	N_L	6.3	9.4	4.7	6.5	7.7	4.6	10.1	9.4
	N_R	13.6	5.8	9.8	6.6	14.8	13.4	4.9	5.4
	BP_L	6.7	6.1	3.8	4.0	8.1	5.7	6.7	6.2
	BP_R	9.9	4.1	6.3	3.8	11.1	9.4	4.1	4.0
	Ph_L	6.2	9.6	5.0	6.8	7.5	3.7	10.6	9.1
	To_L	4.9	9.8	3.8	6.6	6.1	3.5	10.4	10.2
	Ph_R	13.4	4.6	9.4	5.7	14.5	13.4	3.8	3.5
	To_R	14.8	7.2	11.1	7.9	16.0	14.4	6.1	6.8

Table 5.10. The segmental β values for charge transfer and shortest inter-segment C-C, C-N, or N-N distances in the molecular pair **39**, I(000)-II(000). The respective contributions from the nitrogen (N), biphenylene (BP), phenyl (Ph), and tolyl (To) moieties in the left ($_L$) and right ($_R$) sides of TPD molecules in Fig. 10c are shown.

		II(000)							
		N_L	N_R	BP_L	BP_R	Ph_L	To_L	Ph_R	To_R
Segmental β^+ / meV									
I(000)	N_L	0.0	0.0	0.0	0.0	0.0	0.0	0.0	0.0
	N_R	0.0	0.0	0.0	0.0	0.0	0.0	0.0	0.0
	BP_L	0.0	0.2	0.0	0.0	0.0	0.0	-3.5	-5.1
	BP_R	0.0	0.0	0.0	0.0	0.0	0.0	0.0	3.1
	Ph_L	0.0	-0.3	0.0	-5.1	0.0	0.0	0.9	0.3
	To_L	0.0	0.0	0.0	0.0	0.0	0.0	0.0	0.0
	Ph_R	0.0	0.0	0.0	0.0	0.0	0.0	0.0	0.0
	To_R	0.0	0.0	0.0	0.0	0.0	0.0	0.0	0.0
Segmental β^- / meV									
I(000)	N_L	0.0	0.0	0.0	0.0	0.0	0.0	0.0	0.0
	N_R	0.0	0.0	0.0	0.0	0.0	0.0	0.0	0.0
	BP_L	0.0	0.1	0.0	0.0	0.0	0.0	-1.2	0.9
	BP_R	0.0	0.0	0.0	0.0	0.0	0.0	-0.1	-0.4
	Ph_L	0.0	0.2	0.0	-2.0	0.0	0.0	-0.1	-0.1
	To_L	0.0	0.0	0.0	0.0	0.0	0.0	0.0	0.0
	Ph_R	0.0	0.0	0.0	0.0	0.0	0.0	0.0	0.0
	To_R	0.0	0.0	0.0	0.0	0.0	0.0	0.0	0.0
inter-segment C-C, C-N, or N-N distances / Å									
I(000)	N_L	12.8	6.2	9.2	6.6	12.1	13.9	5.3	5.6
	N_R	19.3	9.4	15.1	10.8	19.8	19.8	7.5	6.8
	BP_L	13.1	4.8	9.1	5.6	12.8	14.1	3.7	3.7
	BP_R	16.0	6.4	11.8	7.7	16.1	16.8	4.7	3.7
	Ph_L	8.6	4.3	5.2	3.6	7.9	9.8	4.2	4.3
	To_L	13.5	7.6	10.2	8.0	12.6	14.8	6.6	6.9
	Ph_R	19.1	9.3	14.9	10.7	19.7	19.3	8.2	6.3
	To_R	20.1	10.1	15.8	11.5	20.5	20.5	7.7	8.0

Table 5.11. The segmental β values for charge transfer and shortest inter-segment C-C, C-N, or N-N distances in the molecular pair 41, I(000)-II(001). The respective contributions from the nitrogen (N), biphenylene (BP), phenyl (Ph), and tolyl (To) moieties in the left ($_L$) and right ($_R$) sides of TPD molecules in Fig. 10d are shown.

		II(001)							
		N_L	N_R	BP_L	BP_R	Ph_L	To_L	Ph_R	To_R
Segmental β^+ / meV									
I(000)	N_L	0.0	0.0	0.0	0.0	0.0	0.0	0.0	0.0
	N_R	0.0	0.0	0.3	0.0	-0.5	0.0	0.0	0.0
	BP_L	0.0	0.0	0.0	0.0	0.0	0.0	0.0	0.0
	BP_R	0.0	0.0	0.0	0.0	-6.9	0.0	0.0	0.0
	Ph_L	0.0	0.0	0.0	0.0	0.0	0.0	0.0	0.0
	To_L	0.0	0.0	0.0	0.0	0.0	0.0	0.0	0.0
	Ph_R	0.0	0.0	-3.8	0.0	1.0	0.0	0.0	0.0
	To_R	0.0	0.0	-5.1	3.2	0.5	0.0	0.0	0.0
Segmental β^- / meV									
I(000)	N_L	0.0	0.0	0.0	0.0	0.0	0.0	0.0	0.0
	N_R	0.0	0.0	0.1	0.0	0.3	0.0	0.0	0.0
	BP_L	0.0	0.0	0.0	0.0	0.0	0.0	0.0	0.0
	BP_R	0.0	0.0	-0.1	0.0	-4.5	0.0	0.0	0.0
	Ph_L	0.0	0.0	0.0	0.0	0.0	0.0	0.0	0.0
	To_L	0.0	0.0	0.0	0.0	0.0	0.0	0.0	0.0
	Ph_R	0.0	0.0	-1.3	-0.1	0.0	0.0	0.0	0.0
	To_R	0.0	0.0	1.0	-0.1	-0.1	0.0	0.0	0.0
inter-segment C-C, C-N, or N-N distances / Å									
I(000)	N_L	12.7	19.4	13.0	16.0	8.5	13.4	19.0	20.1
	N_R	6.1	9.4	4.6	6.4	4.1	7.5	9.3	10.1
	BP_L	9.1	15.1	9.0	11.8	5.1	10.1	14.9	15.8
	BP_R	6.4	10.8	5.5	7.7	3.4	7.8	10.7	11.5
	Ph_L	12.1	19.8	12.8	16.1	7.9	12.5	19.7	20.5
	To_L	13.9	19.8	14.0	16.8	9.7	14.7	19.2	20.5
	Ph_R	5.1	7.4	3.5	4.7	4.1	6.5	8.1	7.7
	To_R	5.5	6.7	3.6	3.6	4.2	6.8	6.1	7.9

order of 10^{12} s^{-1} are obtained for the pairs of 51, 52, 55, and 56, reflecting the H_{AB}^{+} values. Therefore, holes can be conveyed along the b-axis through the periodic pairs of 51 and 52 or 55 and 56, as illustrated in Fig. 5.9a. Also, the periodic pairs of 39 and 41, or 67 and 69, which provide the k_{CT}^{+} values larger than 10^{11} s^{-1}, can transport holes macroscopically along the c-axis, as illustrated in Fig. 5.9b. Combinations of these pairs can also convey holes effectively in the b-c plane. For hole transports in the a-direction, the pairs of 39, 40, 41, and 42, or 67, 68, 69, and 70 can be used as illustrated in Fig. 5.11. However, the transports are expected to be inferior to those along the b- and c-axes due to the smaller k_{CT}^{+} values for these pairs.

5.3.7. *"Electron"* Transports in Monoclinic TPD

The H_{AB}^{-} values for the monoclinic polymorph of TPD are also shown in Fig. 5.8a as open circles. All the H_{AB}^{-} values are less than 3.2 meV, meaning the small intermolecular electronic couplings of LUMOs. The segmental β^{-} values for the pairs of 51, 55, 39, and 41 are shown in Tables 5.8–5.11. As in the case of the orthorhombic polymorph, the intermolecular LUMO couplings between the Ph_x and/or To_x rings are small due to the localization of LUMO on the biphenylene moiety, which results in the small H_{AB}^{-} values.

The k_{CT}^{-} values at T = 300 K are represented in Fig. 5.8b as open circles. The values, which results in 10^{5} – 10^{10} s^{-1}, are found to two to three orders smaller than the k_{CT}^{+} values, as in the case of orthorhombic polymorph. Therefore, the electron-transport property of TPD is poor also for the monoclinic polymorph due to the small H_{AB}^{-} values as well as the large λ^{-} value, which is the same conclusion for the orthorhombic polymorph.

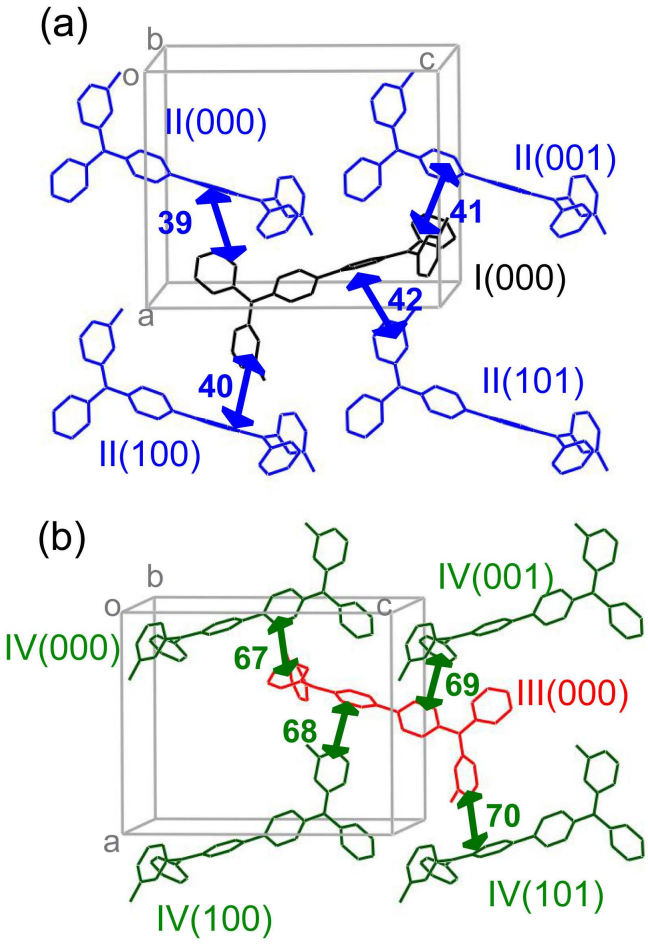

Fig. 5.11. Molecular pairs of (a) 39 (I(000)-II(000)), 40 (I(000)-II(100)), 41 (I(000)-II(001)), and 42 (I(000)-II(101)) and (b) 67 (III(000)-IV(000)), 68 (III(000)-IV(100)), 69 (III(000)-IV(001)), and 70 (III(000)-IV(101)) in the monoclinic polymorph of TPD. These molecular pairs can convey holes in the direction of the a-axis.

5.4. Conclusion

The rate constants for Marcus–type charge transfers and percolation paths for charge transports in both the orthorhombic and monoclinic polymorphs of TPD were investigated. For hole transports, it was found that effective percolation paths exist along specific directions in both the polymorphs. HOMO of TPD delocalizes over the whole molecule, and the outer phenyl and tolyl rings of TPD were found to play an important role for the intermolecular hole transfer due to the inter-segmental close contact between the molecular pairs. In contrast to hole-transfers, the electron-transfer rate constants are much smaller in both the polymorphs. The smaller electron-transfer rate constants originate not only from the larger reorganization energy but also from smaller electron transfer integrals. LUMO of TPD localizes on the central biphenylene segments, which results in small inter-segmental charge transfers between outer phenyl and tolyl rings in the molecular pairs, in spite of the close segmental contacts.

It was shown that the distributions of HOMO and LUMO and intermolecular packings are crucial for charge transfer integrals. In OLEDs, TPD is used in the amorphous state. This study on the segmental contribution to charge transfer integrals shows that the intermolecular packing is crucial for charge transports. Electron transport properties would be better, if paths consisting of consecutive molecular pairs with close contact at the biphenylene segments are percolated. To be exact, information on intermolecular packing in the amorphous state is necessary to quantify the charge transfer integrals. Analysis of charge transports in the amorphous state is one of the subjects in the future.

References

[1] C. W. Tang, S.A. VanSlyke, Appl. Phys. Lett. 51 (1987) 913.

[2] C. Adachi, S. Tokito, T. Tsutsui, S. Saito, Jpn. J. Appl. Phys. 27 (1988) L269.

[3] F. Garnier, R. Hajlaoui, A. Yassar, P. Srivastava, Science 265 (1994) 1684.

[4] Z. Bao, A. Dodabalapur, A. Lovinger, J. Appl. Phys.. Lett. 69 (1996) 4108.

[5] N. Sariciftci, L. Smilowitz, A.J. Heeger, F. Wudl, Science 258 (1992) 1474.

[6] P. Peumans, A. Yakimov, S.R. Forrest, J. Appl. Phys. 2003, 93, 3693.

[7] L.B. Schein, C.B. Duke, A.R. McGhie, Phys. Rev. Lett. 40 (1978) 197.

[8] Y.C. Cheng, R.J. Silbey, D.A. da Silva Filho, J.P. Calbert, J. Cornil, J.L. Brédas, J. Chem. Phys. 118 (2003) 3764.

[9] R.A. Marcus, J. Chem. Phys. 24 (1956) 966.

[10] R.A. Marcus, N. Sutin, Biochim. Biophys. Acta 811 (1985) 265.

[11] H. Bässler, Phys. Stat. Sol. B 175 (1993) 15.

[12] P.F. Barbara, T.J. Meyer, M.A. Ratner, J. Phys. Chem. 100 (1996) 13148.

[13] H. Sirringhaus, P.J. Brown, R.H. Friend, M.M. Nielsen, K. Bechgaard, B.M. Langeveld-Voss, A.J.H. Spiering, R.A.J. Janssen, E.W. Meijer, P. Herwig, D.M. de Leeuw, Nature 410 (1999) 685.

[14] K. Sakanoue, M. Motoda, M. Sugimoto, S. Sakaki, J. Phys. Chem. A 103 (1999) 5551.

[15] M. Malagoli, J.L. Brédas, Chem. Phys. Lett. 327 (2000) 13.

[16] B.C. Lin, C.P. Cheng, Z.P.M. Lao, J. Phys. Chem. A 107 (2003) 5241.

[17] T. Sato, K. Shizu, T. Kuga, K. Tanaka, H. Kaji, Chem. Phys. Lett. 458 (2008) 152.

[18] I. Vilfan, Phys. Status Solidi B 59 (1973) 351.

[19] J.J. Kwiatkowski, J. Nelson, H. Li, J. L. Brédas, W. Wenzel, C. Lennartz, Phys. Chem. Chem. Phys. 10 (2008) 1852.

[20] L. Rodriguez-Monge, S. Larsson, J. Phys. Chem. 100 (1996) 6298.

[21] J. Cornil, D. Beljonne, J.P. Calbert, J.L. Brédas, Adv. Mater. 13 (2001) 1053.

[22] J.L. Brédas, J.P. Calbert, J. Cornil, Proc. Natl. Acad. Sci. USA 99 (2002) 5804.

[23] G.R. Hutchison, M.A. Ratner, T.J. Marks, J. Am. Chem. Soc. 127 (2005) 16866.

[24] J. Kirkpatrick, J. Nelson, J. Chem. Phys. 123 (2005) 084703.

[25] A. Datta, S. Mohakud, S.K. Pati, J. Chem. Phys. 126 (2007) 144710.

[26] V. Coropceanu, J. Cornil, D.A. da Silva Filo, Y. Olivier, R. Silbey, J.L. Brédas, Chem. Rev. 107 (2007) 926.

[27] K. Tanaka, Y. Asai, T. Sato, T. Kuga, T. Yamabe, M. Tokumoto, Chem. Phys. Lett. 259 (1996) 574.

[28] A. Farazdel, M. Dupuis, E. Clementi, A. Aviram, J. Am. Chem. Soc. 112 (1990) 4206.

[29] L. Rodriguez-Monge, S. Larsson, Int. J. Quantum Chem. 61 (1997) 847.

[30] B.C. Lin, C.P. Cheng, Z.Q. You, C.P. Hsu, J. Am. Chem. Soc. 127 (2005) 66.

[31] M. Stolka, J.F. Yanus, D.M. Pai, J. Phys. Chem. 88 (1984) 4707.

[32] J. Kido, M. Kimura, K. Nagai, Science 267 (1995) 1332.

[33] V. Bulović, G. Gu, P.E. Burrows, S.R. Forrest, M.E. Thompson, Nature 380 (1996) 29.

[34] H. Ishii, K. Seki, IEEE Trans. Electron Devices 44 (1997) 1295.

[35] D.F. O'Brien, P.E. Burrows, S.R. Forrest, B.E. Koene, D.E. Loy, M.E. Thompson, Adv. Mater. 10 (1998) 1108.

[36] H. Murata, C.D. Merritt, Z.H. Kafafi, IEEE J. Sel. Top. Quantum Electron. 4 (1998) 119.

[37] H. Mattoussi, H. Murata, C.D. Merritt, Y. Iizumi, J. Kido, Z.H. Kafafi, J. Appl. Phys. 86 (1999) 2642.

[38] K. Seki, N. Hayashi, H. Oji, E. Ito, Y. Ouchi, H. Ishii, Thin Solid Films 393 (2001) 298.

[39] J. Cornil, N.E. Gruhn, D.A. dos Santos, M. Malagoli, P.A. Lee, S. Barlow, S. Thayumanavan, S.R. Marder, N.R. Armstrong, J.L. Brédas, J. Phys. Chem. A 105 (2001) 5206.

[40] M. Malagoli, M. Manoharan, B. Kippelen, J.L. Brédas, Chem. Phys. Lett. 354 (2002) 283.

[41] A.R. Kennedy, W.E. Smith, D.R. Tackley, W.I.F. David, K. Shankland, B. Brown, S.J. Teat, J. Mater. Chem. 12 (2002) 168.

[42] Z. Zhang, E. Burkholder, J. Zubieta, Acta Cryst. C60 (2004) o452.

[43] K. Shankland, A.R. Kennedy, W.I.F. David, J. Mater. Chem. 15 (2005) 4838.

[44] H. Kaji, T. Yamada, N. Tsukamoto, F. Horii, Chem. Phys. Lett. 401 (2005) 246.

[45] P. Cusumano, S. Gambino, J. Electron. Mater. 37 (2008) 231.

[46] P. Poolmee, M. Ehara, S. Hannongbua, H. Nakatsuji, Polymer 46 (2005) 6474.

[47] B. Saha, M. Ehara, H. Nakatsuji, J. Phys. Chem. A 111 (2007) 5473.

[48] P.O. Löwdin, J. Chem. Phys. 18 (1950) 365.

[49] A.D. Becke, Phys. Rev. A 38 (1988) 3098.

[50] A.D. Becke, J. Chem. Phys. 98 (1993) 5648.

[51] C.T. Lee, W.T. Yang, R.G. Parr, Phys. Rev. B 37 (1988) 785.

[52] M.J. Frisch et al., Gaussian 03, Revision E.01, Gaussian, Inc., Wallingford CT, 2004.

[53] M. Wolfsberg, L. Helmholz, J. Chem. Phys. 20 (1952) 837.

[54] R. Hoffmann, J. Chem. Phys. 39 (1963) 1397.

Chapter 6

Revealing Bipolar Charge-Transport Property of 4,4'-*N*,*N*'-dicarbazolylbiphenyl (CBP) by Quantum Chemical Calculations

6.1 Introduction

Organic light-emitting diodes (OLEDs) are promising devices for flat or flexible displays, and lighting equipments [1,2]. Fig. 6.1 shows widely known charge-transport materials for OLEDs, 4,4'-*N*,*N*'-dicarbazolylbiphenyl (CBP) [3-10] and *N*,*N*'-diphenyl-*N*,*N*'-di(*m*-tolyl) benzidine (TPD) [2,11-16]. The chemical structures of CBP and TPD are similar to each other, while the charge-transport properties are not. For CBP, both the hole and electron mobilities are on the order of 10^{-3} cm^2/Vs [7,8]. According to preceding studies [5,7-10], CBP is called as a '*bipolar*' material on the basis of the comparable hole and electron mobilities. The latter, TPD, shows a similar hole-transport property with the mobility of ~10^{-3} cm^2/Vs; however, the electron mobility is inferior, <10^{-7} cm^2/Vs [14-16]. Understanding the origins of the different charge-transport properties between CBP and TPD is of importance not only for fundamental science but also for designing molecules with excellent performance.

In Chapter 5, charge-transport property of TPD was investigated, based on Marcus theory [17,18]. Again, the charge-transfer rate constant, k_{CT}, is described by the theory as

$$k_{CT} = \frac{4\pi^2}{h} H_{AB}^2 \frac{1}{\sqrt{4\pi\lambda k_B T}} \exp(-\frac{\lambda}{4k_B T}) \qquad (6.1)$$

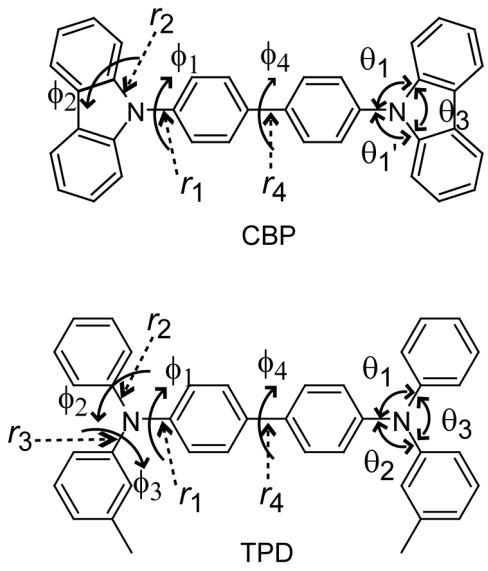

Fig. 6.1. The chemical structures of CBP and TPD. The θ, ϕ, and *r* represent bond angles, torsion angles, and bond lengths, respectively.

where, λ is the reorganization energy, and H_{AB} is the charge transfer integral between the relevant two molecules. The temperature, *T*, is fixed at 300 K throughout this Chapter. The *h* and k_B are the Planck and Boltzmann constants, respectively. It was found in Chapter 5 that the hole transfer integrals in TPD crystals are several times larger than the electron transfer integrals [19]. The HOMO of TPD spreads over the molecule. Large intermolecular overlaps can be formed between the phenyl and/or tolyl rings, which have close intermolecular contacts in the crystals. In contrast, the LUMO of TPD is localized on the central biphenylene moiety, which results in small intermolecular overlaps (that is, small electron transfer integrals). Owing to both the small reorganization energies and the large charge transfer integrals for the hole transfers, the hole-transfer rate constants were calculated to be more than two orders of magnitude larger than the electron-transfer rate constants. In addition, there are effective hole-transport paths consisting of consecutive molecular pairs with large hole-transfer rate constants [19]. The results show the favorable hole-transport property of TPD.

On the other hand, the origins of the bipolar charge-transport property of CBP were unclear, despite the practical importance as a host material of emitting layers in OLEDs. In this Chapter, the charge-transport property of CBP in the crystal is investigated as in the case of TPD. The reorganization energies and the charge transfer integrals are compared with those for TPD. The results explain the difference of charge-transport properties between CBP and TPD.

6.2 Computational Section

The structural optimizations were performed for neutral, cationic, and anionic CBP molecules by DFT method using the B3LYP functional [20-22] and the 6-31G(d) basis set. The molecular structure in Ref. 23 was adopted as an initial structure for the optimizations. Using the DFT-optimized structures, the reorganization energies were calculated, according to Chapter

5. The packing structure of the CBP crystal was also taken from Ref. 23. Fig. 6.2 shows the unit cell. For all the pairs of two molecules in the identical and the neighboring cells, the charge transfer integrals were calculated by extended Hückel method from Eq. 6.2 [19,24,25].

$$H_{AB} = \frac{\beta - \frac{\alpha_A + \alpha_B}{2} S}{1 - S^2} \tag{6.2}$$

Here, α_A = $<\Phi_A|\mathbf{H}|\Phi_A>$, α_B = $<\Phi_B|\mathbf{H}|\Phi_B>$, β = $<\Phi_A|\mathbf{H}|\Phi_B>$ = $<\Phi_B|\mathbf{H}|\Phi_A>$, S = $<\Phi_A|\Phi_B>$ = $<\Phi_B|\Phi_A>$, and **H** is the electronic Hamiltonian. Φ_A and Φ_B are the HOMOs of isolated molecules, A and B, respectively, for the evaluations of hole transfer integrals. Also, for the evaluations of electron transfer integrals, they are the LUMOs of isolated molecules, A and B, respectively. All of the quantum chemical calculations were performed by Gaussian 03 program [26]. The symmetry was neglected in the calculations.

6.3. Results and Discussion

6.3.1. Molecular Structures and Reorganization Energies

The structural parameters of the crystalline CBP (Fig. 6.2) are shown in Table 6.1. Note that the parameters for the two molecules in Fig. 6.2 are equivalent with each other. The features are as follows. 1) The summation of the three ∠CNC bond angles around the nitrogen atom, $2\theta_1 + \theta_3$ (see Fig. 6.1), is almost 360^o, meaning that the nitrogen atom and the three carbon atoms bonded to the nitrogen atom are in the same plane. This is similar to those for other triphenylamine compounds, including TPD. 2) The torsion angle of the central C-C bond in

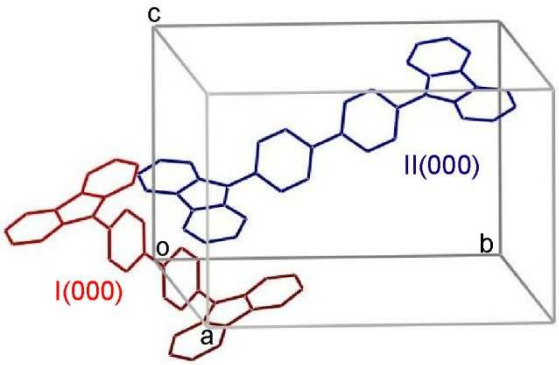

Fig. 6.2. The unit cell of CBP crystal and representations of molecules I and II. The cell parameters are as follows; a = 8.01 Å, b = 16.01 Å, c = 10.24 Å, $\alpha = \gamma = 90.0^{o}$, and $\beta = 110.2^{o}$.

Table 6.1. Structural parameters of a CBP molecule in the crystal, and those optimized by DFT method for the neutral, cationic, and anionic states. The parameters are defined in Fig. 6.1. As an initial structure for the optimizations, the crystalline structure was adopted. The parameters for the optimized TPD are also shown for comparison.

		bond angle / ^{o}			torsion angle / ^{o}				bond length / Å			
		θ_1	θ_2	θ_3	ϕ_1	ϕ_2	ϕ_3	ϕ_4	r_1	r_2	r_3	r_4
CBP												
crystal[a]		125±1	-	108	49±3	9±2	-	0	1.42	1.39±0.01	-	1.49
	neutral	126	-	108	53	2	-	0	1.42	1.4	-	1.49
optimized	cation	126	-	108	45	4	-	0	1.4	1.41	-	1.47
	anion	126	-	108	70	1	-	0	1.43	1.39	-	1.44
TPD												
	neutral	120	120	120	41	41	43	36	1.42	1.42	1.42	1.48
optimized	cation	121	121	118	26	49	49	21	1.39	1.43	1.43	1.46
	anion	119	119	122	61	31	32	9	1.44	1.41	1.41	1.44

[a] The values are taken from Ref. 23.

the biphenylene moiety, ϕ_4, is 0^o, indicating that the biphenylene moiety has a planar structure in the CBP crystal. This feature is different from that for the TPD crystal, ϕ_4 = 34–37^o [27,28]. The difference is considered to originate from a molecular packing effect, as discussed below.

Table 6.1 also shows the results of the structure optimizations by DFT method for CBP in the neutral, cationic, and anionic states. It must be noted that all of the CBP structures in Table 6.1 provide imaginary frequencies for a rotational fluctuation around the torsion angle, ϕ_4. Fig. 6.3 shows the torsion angle ϕ_4 dependence of the self-consistent field (SCF) energy for the optimized structure in the neutral state. The energetic minimum corresponds to $\phi_4 = 30^o$, not 0^o. This indicates that the above optimized structure corresponds to a saddle point of the potential. The energetic difference from the potential minimum is about 6 kJ/mol. This result shows that the crystalline structure of CBP is different from the most stable conformation for an isolated molecule, probably due to the intermolecular packing effects in the crystal. In this Chapter, the optimized structures in Table 6.1 are adopted to estimate the reorganization energies for the crystalline structure.

For the cationic and anionic structures, the torsion angles, ϕ_2 and ϕ_4, are almost comparable with those in the neutral structure. In contrast, the torsion angle ϕ_1 and bond length r_4 are different between the neutral and charged states. Based on these DFT-optimized structures, the reorganization energies were calculated by extended Hückel and DFT methods. The reorganization energies obtained by extended Hückel method are 0.10 and 0.19 eV for hole and electron transfers, respectively. The value for electron transfer of CBP is found to be small, compared with the values for the electron transfer of TPD (0.15 and 0.40 eV for hole and electron transfers, respectively [19]).

The ratios of hole- and electron-transfer rate constants are summarized in Table 6.2. Assuming that the hole and electron transfer integrals are equivalent, the ratio of hole- and

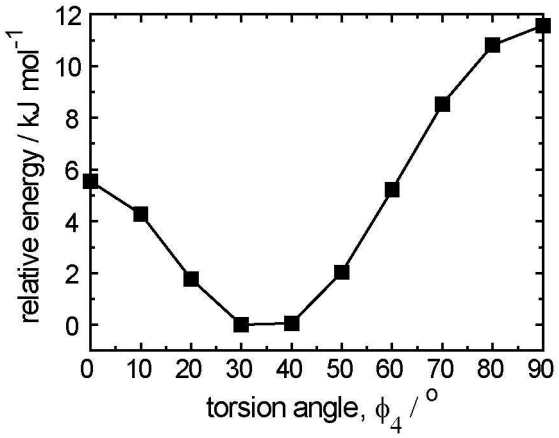

Fig. 6.3. The torsion angle ϕ_4 dependence of the SCF energy of a CBP molecule. The calculations were carried out with the interval of 10^o and the energies are represented as relative values against the minimum energy, -3.93×10^6 kJ mol^{-1} ($\phi_4 = 30^o$). The other structural parameters are fixed to the optimized values shown in Table 6.1. The calculations were performed by B3LYP/6-31G(d) level.

Table 6.2. The ratio of the maximum hole- and electron-transport rate constants, k_{CT}^{+}/k_{CT}^{-}, of CBP and TPD, based on Marcus theory.

	calculation method for reorganization energy	k_{CT}^{+}/k_{CT}^{-} [a]	k_{CT}^{+}/k_{CT}^{-} [b]
CBP	extended Hückel	3.3	1.7
	DFT	1.7×10	9.2
TPD	extended Hückel	2.0×10	1.4×10^2
	DFT	2.7×10	1.9×10^2

[a] The ratios are obtained under the assumption that the hole and electron transfer integrals are equal.

[b] The ratios are obtained by considering both the reorganization energies and transfer integrals.

electron-transfer rate constants for CBP is calculated to be 3.3 from Eq. 6.2. A better electron-transport property is expected for CBP by comparing the ratio of 20 for TPD [19]. For TPD, the reorganization energies calculated by extended Hückel and DFT methods led the comparable values for the ratio of hole- and electron-transfer rate constants, under the assusmption that hole- and electron transfer integrals are the same (see Table 6.2 and Ref. 19). This is not the case for CBP; the ratio of hole- and electron-transfer rate constants calculated by DFT method is larger than that calculated by extended Hückel method. Nevertheless, if both the reorganization energy and charge transfer integral are taken into account, the ratios of hole- and electron-transfer rate constants calculated by extended Hückel and DFT methods are in the same order of magnitude as shown in Table 6.2. For the following calculations, the reorganization energies by extended Hückel method are used, which was accepted in Ref. 19.

6.3.2. Frontier Orbitals

Fig. 6.4 illustrates the HOMO and LUMO calculated by extended Hückel method for CBP. The HOMO and LUMO of TPD are also shown for comparison. Table 6.3 summarizes, in percentage, the squares of the MO coefficients of respective segments of CBP, nitrogen (N), biphenylene (BP), and the two benzene rings in the carbazole moiety (Bz1 and Bz2). The subscripts of “L” and “R” mean left and right sides of the molecule, respectively. For the HOMO, all the contributions are from 9 to 20%, meaning that the MO is relatively delocalized over the molecule. Among them, the contributions from the biphenylene moieties are the largest (20% each for BP_L and BP_R), as in the case of TPD (see also Table 3). For the LUMO, contributions of the biphenylene moieties of CBP (17% each for BP_L and BP_R) are much smaller than those for TPD (43% each for BP_L and BP_R). Instead, contributions of the carbazole

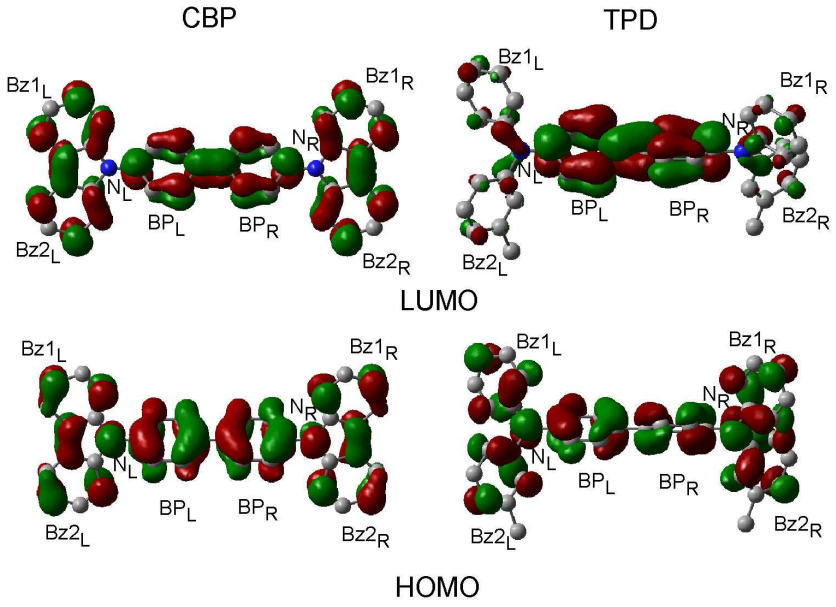

Fig. 6.4. The HOMO and LUMO of CBP calculated by extended Hückel method for the crystalline conformation. Those of TPD are also shown for comparison. The value for the surfaces is 0.02 a.u.

Table 6.3. Contributions of the nitrogen (N), biphenylene (BP), and the benzene rings in the carbazole moieties (Bz1, Bz2) of CBP to the HOMO and LUMO. The subscript of "L" or "R" indicates the left or right side of the molecule in Fig. 6.4. The values for TPD are also shown for comparison.

		N_L	N_R	BP_L	BP_R	$Bz1_L$	$Bz2_L$	$Bz1_R$	$Bz2_R$
CBP	HOMO	11	11	20	20	9	9	9	9
	LUMO	0	0	17	17	17	17	17	17
TPD	HOMO	15	15	18	18	9 [a]	9 [b]	9 [a]	9 [b]
	LUMO	1	1	43	43	4 [a]	3 [b]	4 [a]	3 [b]

[a] The values are for the phenyl group of TPD.

[b] The values are for the tolyl group of TPD.

moieties of CBP (17% each for $Bz1_R$, $Bz1_L$, $Bz2_R$, and $Bz2_L$) are large, compared with the LUMO of TPD (3-4% each for $Bz1_R$, $Bz1_L$, $Bz2_R$, and $Bz2_L$). Fig. 6.4 clearly shows the difference between the LUMO of CBP and that of TPD, which is a critical point for electron transports as discussed later.

6.3.3. Molecular Pairs

As shown in Fig. 6.2, the unit cell of the CBP crystal contains two molecules. These molecules are referred as I and II, respectively. The center of gravity of I locates on the origin of the cell, and that of II does on the center of the b-c plane. Defining that the cell in Fig. 6.2 as cell (000), neighboring cells at the +a, -a, +b, -b, +c, and -c directions are represented as (100), (-100), (010), (0-10), (001), and (00-1), respectively. Hereafter, a molecule X (X = I or II) in the cell (abc) (a, b, c = -1, 0, or 1) is referred to as X(abc) as defined in Chapter 5 [19]. For example, I(000) denotes molecule I in the cell (000).

Charge transfer integrals were investigated for all the molecular pairs between a molecule in the cell (000) and that in a cell (abc) (a, b, c = -1, 0, or 1). The 105 pairs are listed in Table 6.4. Depending on the relative geometries, the pairs can be classified into 25 independent types, as indicated by geometrical types of A–Y in Table 4. For these 25 types of pairs, the charge transfer integrals were calculated, according to Eq. 6.2.

Table 6.4. Molecular pairs in the CBP crystal. Pairs between a molecule in the cell (000) and another molecule in cells (abc) (a, b, c = -1, 0, 1) are considered. They are classified into 25 types of relative geometries, A–Y. The geometrical types of A, B, and C are shown in boldface.

I(000)-I(abc)

a	b	C	geometrical type	a	b	c	geometrical type	a	b	c	geometrical type
	-			1	0	0	G	-1	0	0	G
0	0	1	H	1	0	1	D	-1	0	1	R
0	0	-1	H	1	0	-1	R	-1	0	-1	D
0	1	0	E	1	1	0	M	-1	1	0	F
0	1	1	P	1	1	1	Q	-1	1	1	T
0	1	-1	J	1	1	-1	V	-1	1	-1	**B**
0	-1	0	E	1	-1	0	F	-1	-1	0	M
0	-1	1	J	1	-1	1	**B**	-1	-1	1	V
0	-1	-1	P	1	-1	-1	T	-1	-1	-1	Q

I(000)-II(abc)

a	b	C	geometrical type	a	b	c	geometrical type	a	b	c	geometrical type
0	0	0	**A**	1	0	0	**C**	-1	0	0	K
0	0	1	O	1	0	1	I	-1	0	1	X
0	0	-1	**A**	1	0	-1	K	-1	0	-1	**C**
0	1	0	L	1	1	0	N	-1	1	0	S
0	1	1	W	1	1	1	U	-1	1	1	Y
0	1	-1	L	1	1	-1	S	-1	1	-1	N
0	-1	0	**A**	1	-1	0	**C**	-1	-1	0	K
0	-1	1	O	1	-1	1	I	-1	-1	1	X
0	-1	-1	**A**	1	-1	-1	K	-1	-1	-1	**C**

II(000)-I(abc)

a	b	C	geometrical type	a	b	c	geometrical type	a	b	c	geometrical type
	-			1	0	0	K	-1	0	0	**C**
0	0	1	**A**	1	0	1	**C**	-1	0	1	K
0	0	-1	O	1	0	-1	X	-1	0	-1	I
0	1	0	**A**	1	1	0	K	-1	1	0	**C**
0	1	1	**A**	1	1	1	**C**	-1	1	1	K
0	1	-1	O	1	1	-1	X	-1	1	-1	I
0	-1	0	L	1	-1	0	S	-1	-1	0	N
0	-1	1	L	1	-1	1	N	-1	-1	1	S
0	-1	-1	W	1	-1	-1	Y	-1	-1	-1	U

II(000)-II(abc)

a	b	C	geometrical type	a	b	c	geometrical type	a	b	c	geometrical type
	-			1	0	0	G	-1	0	0	G
0	0	1	H	1	0	1	D	-1	0	1	R
0	0	-1	H	1	0	-1	R	-1	0	-1	D
0	1	0	E	1	1	0	F	-1	1	0	M
0	1	1	J	1	1	1	**B**	-1	1	1	V
0	1	-1	P	1	1	-1	T	-1	1	-1	Q
0	-1	0	E	1	-1	0	M	-1	-1	0	F
0	-1	1	P	1	-1	1	Q	-1	-1	1	T
0	-1	-1	J	1	-1	-1	V	-1	-1	-1	**B**

6.3.4. Hole Transfer Integrals

The hole transfer integrals for the geometrical types of A–Y are shown in Fig. 6.5a. The types of A, B, and C have large values, 3.1, 1.4, and 3.0 meV, respectively. The value for the type of D is 0.6 meV, and the values for the other types are less than 0.1 meV. In Fig. 6.5b, the hole transfer integrals are shown as a function of intermolecular distance between the center of gravity of each molecule. Also, in Fig. 6.5c, they are presented as a function of the shortest inter-segment distance. Here, the shortest internuclear distance between the relevant two molecules are referred to as the shortest inter-segment distance. Only the distances between carbon and/or nitrogen atoms are considered (hydrogen atoms are neglected), because hydrogen atoms hardly contribute to the frontier orbitals. It is found from these figures that the hole transfer integral strongly depends on the shortest inter-segment distance rather than the distance between the center of gravity. This is similar to the case of TPD in Chapter 5.

Since the charge transfer integral in Eq. 6.2 is found to be almost proportional to β (this relation holds because $1 >> S^2$ and $\beta \cong 1.75S(\alpha_A+\alpha_B)/2$ [29, 30], as shown in Chapter 5 [19]), the contribution of respective segments, N, BP, Bz1, and Bz2, to the charge transport integral can be investigated by dividing the β value for the respective segments. The β values divided for the respective segments are called "segmental β values" as defined in Chapter 5 and Ref. 19. The segmental β values are useful to understand which segments dominantly contribute to charge transfer integrals. Tables 6.5, 6.6, and 6.7 show the segmental β values for the representative molecular pairs of the geometrical types of A, B, and C, respectively. The pairs are I(000)-II(000) (type A), I(000)-I(1-11) (type B), and I(000)-II(100) (type C) (see Fig. 6.6). The shortest inter-segment distances are also shown in Tables 6.5–6.7. Regarding I(000)-II(000), the geometrical type of A (Table 6.5), the following interaction are dominant for the total β value, -6.5 meV; $Bz1_R$-$Bz1_L$ (-7.9 meV), BP_R-N_L (-4.9 meV), and BP_R-$Bz2_L$ (-4.4

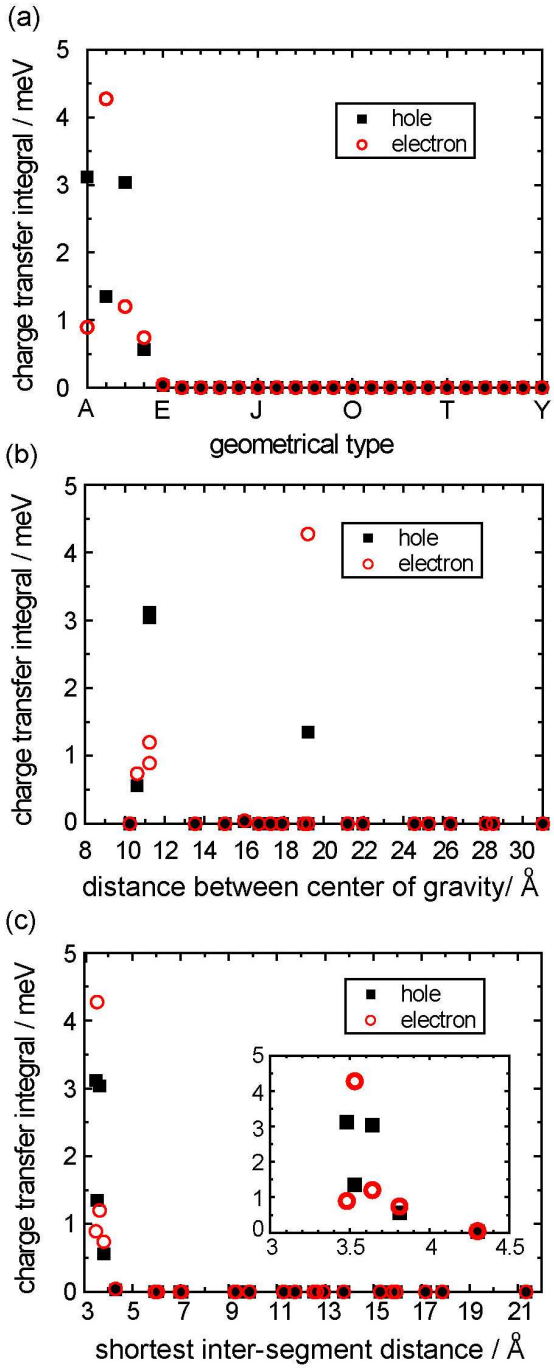

Fig. 6.5. The hole (■) and electron (○) transfer integrals for the geometrical types of A–Y in the CBP crystal. The values are shown (a) in order of A–Y, (b) as a function of intermolecular distance between the center of gravity of relevant two molecules, and (c) as a function of shortest inter-segment distance. The inset in (c) shows a expanded figure in the range of 3–4.5 Å.

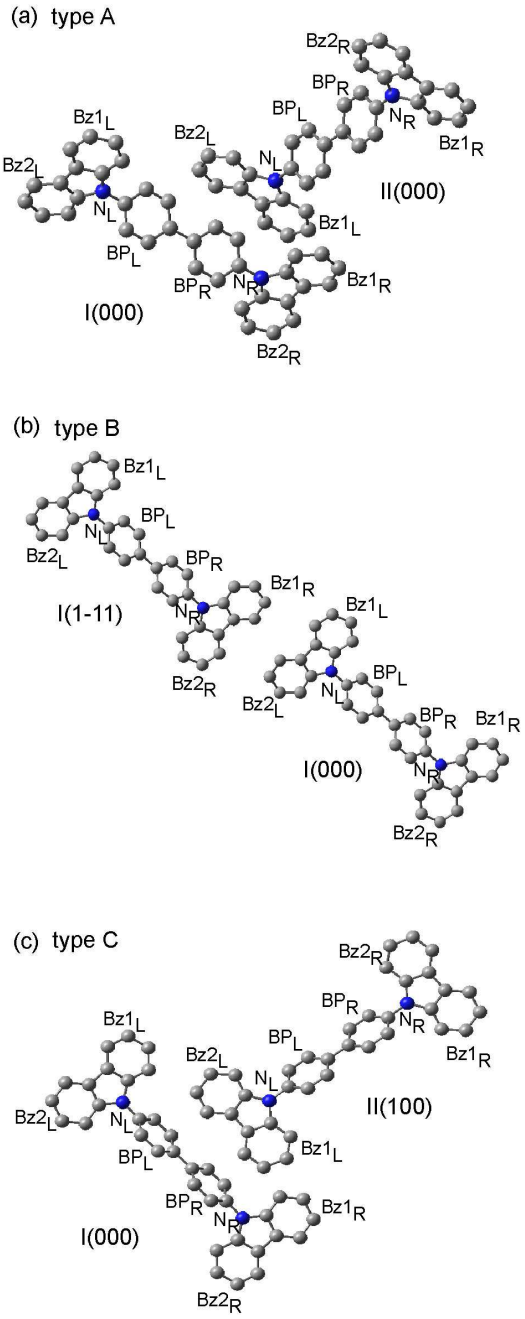

Fig. 6.6. Representations of the molecular pairs, (a) I(000)-II(000), (b) I(000)-I(1-11), and (c) I(000)-II(100). The types of their relative geometries are A, B, and C, respectively.

Table 6.5. The segmental β values for charge transfer and shortest inter-segment C-C, C-N, or N-N distances in the molecular pair I(000)-II(000), which corresponds to the geometrical type of **"A"**. The segments are the nitrogen (N), biphenylene (BP), and benzene rings in the carbazole moieties (Bz1 and Bz2) in the left (L) and right (R) sides of CBP molecules as shown in Fig. 6.6a.

		II(000)							
		N_L	N_R	BP_L	BP_R	$Bz1_L$	$Bz2_L$	$Bz1_R$	$Bz2_R$
segmental β for hole transfer / meV (total β = -6.5 meV)									
I(000)	N_L	0.0	0.0	0.0	0.0	0.0	0.0	0.0	0.0
	N_R	0.0	0.0	0.0	0.0	-0.9	0.0	0.0	0.0
	BP_L	0.0	0.0	0.0	0.0	0.0	1.9	0.0	0.0
	BP_R	**-4.9**	0.0	0.5	0.0	2.2	**-4.4**	0.0	0.0
	$Bz1_L$	0.0	0.0	0.0	0.0	0.0	0.0	0.0	0.0
	$Bz2_L$	0.0	0.0	0.0	0.0	0.0	0.0	0.0	0.0
	$Bz1_R$	0.7	0.0	3.3	0.0	**-7.9**	0.0	0.0	0.0
	$Bz2_R$	0.0	0.0	0.0	0.0	3.1	0.0	0.0	0.0
segmental β for electron transfer / meV (total β = 1.4 meV)									
I(000)	N_L	0.0	0.0	0.0	0.0	0.0	0.0	0.0	0.0
	N_R	0.0	0.0	0.0	0.0	0.0	0.0	0.0	0.0
	BP_L	0.0	0.0	0.0	0.0	0.0	-2.0	0.0	0.0
	BP_R	0.1	0.0	0.1	0.0	-2.8	-1.8	0.0	0.0
	$Bz1_L$	0.0	0.0	0.0	0.0	0.0	0.0	0.0	0.0
	$Bz2_L$	0.0	0.0	0.0	0.0	0.0	0.0	0.0	0.0
	$Bz1_R$	-0.1	0.0	0.9	0.0	**4.2**	0.0	0.0	0.0
	$Bz2_R$	0.0	0.0	0.0	0.0	2.8	0.0	0.0	0.0
shortest C-C, C-N, or N-N distance / Å									
I(000)	N_L	9.7	16.2	10.2	12.9	9.9	6.8	17.4	15.6
	N_R	5.2	13.3	5.7	9.4	4.2	5.1	13.6	14.2
	BP_L	6.1	13.7	6.8	10.0	6.3	3.8	14.8	13.5
	BP_R	**3.7**	12.4	4.6	8.4	3.5	**3.5**	13.1	13.0
	$Bz1_L$	9.6	14.6	9.8	11.7	10.4	6.9	15.8	13.5
	$Bz2_L$	10.8	17.6	11.5	14.3	10.8	7.8	18.8	17.0
	$Bz1_R$	4.4	10.2	3.8	6.6	**3.5**	5.3	10.1	11.3
	$Bz2_R$	6.1	14.2	6.9	10.5	4.0	5.8	14.2	15.3

meV) (the left and right sides correspond to the segments in I(000) and II(000), respectively). All the types of the segments, N, BP, and Bz, contribute to the above interactions. The shortest inter-segment distance is a crucial factor for charge transfers; the distances for the above three segmental pairs are less than 3.8 Å, whereas the segmental β values are 0.0 meV when the distance is longer than 5.1 Å. For I(000)-I(1-11), the geometrical type of B (Table 6.6), the segmental interaction between $Bz1_R$-$Bz2_L$ (-1.9 meV) is dominant for the total β value of -3.1 eV. This segmental interaction is smaller than the significant interactions for the types A and C in spite that the shortest inter-segment distance is as short as 3.5 Å. This suggests that the relative orientation of the relevant two molecules also affects the segmental β value as well as the inter-segment distance. Lastly, the total β value is 7.0 meV for I(000)-II(100), the geometrical type of C (Table 6.7). The most significant interaction is obtained for the segmental pair of BP_R-$Bz1_L$; the segmental β value is 6.4 meV and the shortest inter-segment distance is 3.6 Å. Considering the geometrical types of A–C, holes are favorably transported through any of the segments, N, BP, and Bz.

6.3.5. Electron Transfer Integrals

Fig. 6.5a also shows the electron transfer integrals for the geometrical types of A–Y. The geometrical type of B provides the largest value of the electron transfer integral, 4.3 meV. The values for the types of A, C, and D are 0.9, 1.2, and 0.7 meV, respectively. For the others, the values are less than 0.1 meV. In Figs. 6.5b and 6.5c, the electron transfer integrals are also shown as a function of the intermolecular distance between the center of gravity and the shortest inter-segment distance, respectively. As in the case of the hole transfer integral, the electron transfer integral strongly depends on the shortest inter-segment distance rather than the distance between the center of gravity.

Table 6.6. The segmental β values for charge transfer and shortest inter-segment C-C, C-N, or N-N distances in the molecular pair I(000)-I(1-11), which corresponds to the geometrical type of **"B"** (see Fig. 6.6b).

		I(1-11)							
		N_L	N_R	BP_L	BP_R	$Bz1_L$	$Bz2_L$	$Bz1_R$	$Bz2_R$
segmental β for hole transfer / meV (total β = -3.1 meV)									
I(000)	N_L	0.0	0.0	0.0	0.0	0.0	0.0	0.0	0.0
	N_R	0.0	0.0	0.0	0.0	0.0	0.0	0.0	0.0
	BP_L	0.0	0.0	0.0	0.0	0.0	0.0	0.0	0.0
	BP_R	0.0	0.0	0.0	0.0	0.0	0.0	0.0	0.0
	$Bz1_L$	0.0	0.0	0.0	0.0	0.0	0.0	-0.6	0.0
	$Bz2_L$	0.0	0.0	0.0	0.0	0.0	0.0	**-1.9**	-0.6
	$Bz1_R$	0.0	0.0	0.0	0.0	0.0	0.0	0.0	0.0
	$Bz2_R$	0.0	0.0	0.0	0.0	0.0	0.0	0.0	0.0
segmental β for electron transfer / meV (total β = 6.5 meV)									
I(000)	N_L	0.0	0.0	0.0	0.0	0.0	0.0	0.0	0.0
	N_R	0.0	0.0	0.0	0.0	0.0	0.0	0.0	0.0
	BP_L	0.0	0.0	0.0	0.0	0.0	0.0	0.0	0.0
	BP_R	0.0	0.0	0.0	0.0	0.0	0.0	0.0	0.0
	$Bz1_L$	0.0	0.0	0.0	0.0	0.0	0.0	0.3	0.0
	$Bz2_L$	0.0	0.0	0.0	0.0	0.0	0.0	**5.9**	0.3
	$Bz1_R$	0.0	0.0	0.0	0.0	0.0	0.0	0.0	0.0
	$Bz2_R$	0.0	0.0	0.0	0.0	0.0	0.0	0.0	0.0
shortest C-C, C-N, or N-N distance / Å									
I(000)	N_L	19.2	9.5	15.1	10.9	19.4	20.2	6.2	7.7
	N_R	29.1	19.2	24.9	20.6	29.4	29.9	15.9	16.5
	BP_L	20.6	10.9	16.4	12.2	20.8	21.6	7.5	8.8
	BP_R	24.9	15.1	20.7	16.4	25.1	25.8	11.7	12.6
	$Bz1_L$	16.5	7.7	12.6	8.8	16.5	17.7	4.0	6.7
	$Bz2_L$	15.9	6.2	11.7	7.5	16.3	16.8	**3.5**	4.0
	$Bz1_R$	29.9	20.2	25.8	21.6	30.0	31.0	16.8	17.7
	$Bz2_R$	29.4	19.4	25.1	20.8	29.9	30.0	16.3	16.5

Table 6.7. The segmental β values for charge transfer and shortest inter-segment C-C, C-N, or N-N distances in the molecular pair I(000)-II(100), which corresponds to the geometrical type of **"C"** (see Fig. 6.6c).

		II(100)							
		N_L	N_R	BP_L	BP_R	$Bz1_L$	$Bz2_L$	$Bz1_R$	$Bz2_R$
segmental β for hole transfer / meV (total β = 7.0 meV)									
I(000)	N_L	0.0	0.0	0.0	0.0	0.0	0.1	0.0	0.0
	N_R	0.0	0.0	0.0	0.0	-0.6	0.0	0.0	0.0
	BP_L	0.0	0.0	0.0	0.0	0.0	0.8	0.0	0.0
	BP_R	0.0	0.0	0.0	0.0	**6.4**	-0.2	0.0	0.0
	$Bz1_L$	0.0	0.0	0.0	0.0	0.0	-2.7	0.0	0.0
	$Bz2_L$	0.0	0.0	0.0	0.0	0.0	0.0	0.0	0.0
	$Bz1_R$	0.0	0.0	0.0	0.0	3.2	0.0	0.0	0.0
	$Bz2_R$	0.0	0.0	0.0	0.0	0.0	0.0	0.0	0.0
segmental β for electron transfer / meV (total β = -1.8 meV)									
I(000)	N_L	0.0	0.0	0.0	0.0	0.0	0.0	0.0	0.0
	N_R	0.0	0.0	0.0	0.0	0.0	0.0	0.0	0.0
	BP_L	0.0	0.0	0.0	0.0	-0.2	-0.3	0.0	0.0
	BP_R	0.0	0.0	0.0	0.0	**-0.2**	-0.8	0.0	0.0
	$Bz1_L$	0.0	0.0	0.0	0.0	0.0	0.1	0.0	0.0
	$Bz2_L$	0.0	0.0	0.0	0.0	0.0	0.0	0.0	0.0
	$Bz1_R$	0.0	0.0	0.0	0.0	-0.4	0.0	0.0	0.0
	$Bz2_R$	0.0	0.0	0.0	0.0	0.0	0.0	0.0	0.0
shortest C-C, C-N, or N-N distance / Å									
I(000)	N_L	8.5	17.3	9.6	13.3	7.5	4.5	18.4	17.1
	N_R	7.9	16.4	9.0	12.5	4.3	7.0	16.4	17.6
	BP_L	6.6	15.9	7.9	11.8	4.5	3.7	16.8	16.2
	BP_R	6.4	15.5	7.6	11.5	**3.6**	4.2	15.9	16.3
	$Bz1_L$	7.4	15.0	8.0	11.5	7.1	3.7	16.3	14.4
	$Bz2_L$	9.7	18.6	10.9	14.7	8.7	5.7	19.8	18.4
	$Bz1_R$	6.8	13.8	7.5	10.4	3.8	6.6	13.4	15.0
	$Bz2_R$	9.2	17.7	10.3	13.9	5.5	8.3	17.5	18.9

The segmental β values of the electron transfer integrals for the geometrical types of A–C are also shown in Tables 6.5–6.7, respectively. For the pair of I(000)-II(000), the geometrical type of A (Table 6.5), the β value for $Bz1_R$-$Bz1_L$ with the shortest inter-segment distance of 3.5 Å is dominant, 4.2 meV. This indicates that the LUMO on the carbazole moieties, which have close intermolecular contacts, is advantageous for the large segmental β value. For I(000)-I(1-11), the geometrical type of B (Table 6.6), the interaction between $Bz2_L$-$Bz1_R$ is significant, 5.9 meV, also indicating the importance of the carbazole moieties for electron transfers. For I(000)-II(100), the geometrical type of C (Table 6.7), the magnitudes of all the segmental β values are less than 0.8 meV, although the interaction between $Bz2_L$-BP_R is the largest. Considering the geometrical types of A–C, electrons are favorably transported through the carbazole moieties. The LUMO which spreads over the molecule, including the carbazole segments, would be an origin of the different electron-transport property between CBP and TPD. For TPD, the LUMO is localized on the central biphenylene moiety, which is unfavorable for providing large segmental β values.

Fig. 6.6 shows that only the carbazole moieties are in close intermolecular contact for the geometry of type B. However, this geometry provides the largest electron transfer integral, as shown in Fig. 6.5a. This result indicates that large transfer integrals can be obtained even if not all the segments are in close intermolecular contacts; only a partial contact is often enough.

6.3.6. Rate Constants and Paths for Charge Transfer

Fig. 6.7 shows the hole and electron transfer rate constants for the geometrical types of A–H at 300 K, using the above reorganization energies and charge transfer integrals. For the other geometrical types, I–Y, the values are less than 10^1 s^{-1}. The hole-transfer rate constants for the types of A, B, and C are 2.0×10^{11}, 3.7×10^{10}, and 1.9×10^{11} s^{-1}, respectively. The value for the

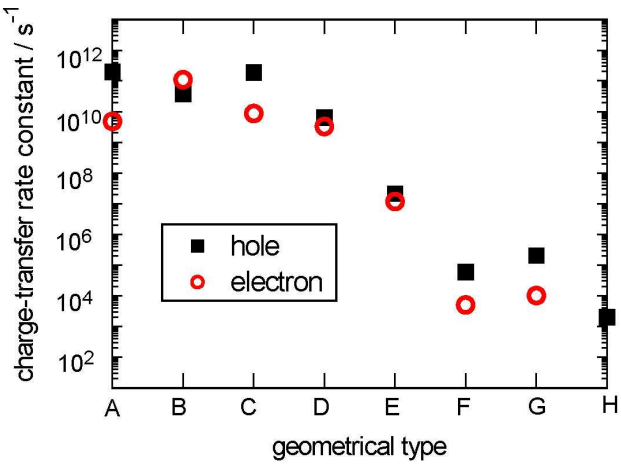

Fig. 6.7. The hole- (■) and electron- (○) transfer rate constants, k_{CT}, at 300 K calculated using the transfer integrals in Fig. 6.5. The rate constants smaller than 10^1 s^{-1} are not shown.

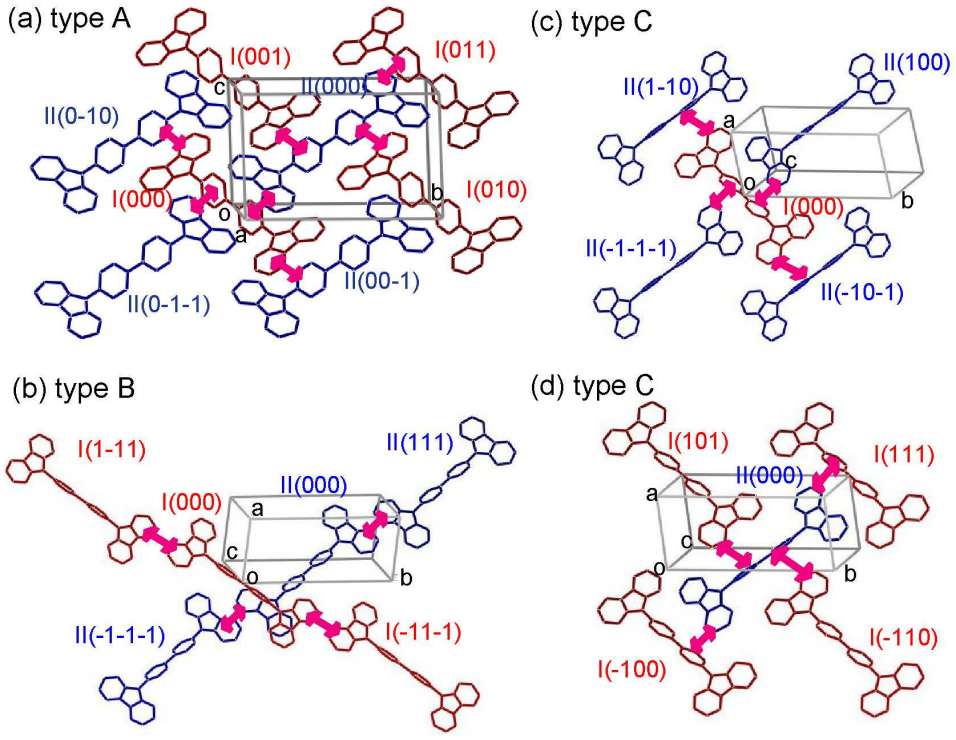

Fig. 6.8. Representations of percolation paths for both the hole and electron transports. The paths consist of the molecular pairs with large carrier-transfer rate constants, geometrical types (a) A, (b) B, and (c, d) C.

type of D is 6.4×10^{9} s^{-1}, and those for the rest types are less than 2.1×10^{7} s^{-1}. On the electron-transfer rate constants, large values are obtained for the types of A, B, and C; 4.8×10^{9}, 1.1×10^{11}, and 8.6×10^{9} s^{-1}, respectively. The value for the type D is 3.3×10^{9} s^{-1}, and those for the rest types are less than 1.2×10^{7} s^{-1}. The ratio of the maximum hole- and electron-transfer rate constants is 1.7. Compared with the orthorhombic crystal of TPD, for which the ratio is 1.4×10^{2}, the bipolar charge-transport property of CBP is clearly presented.

In the TPD crystals, there are effective paths for the hole transport [22]. The paths consist of successive molecular pairs with large hole-transfer rate constants. Here, we investigate paths for the hole and electron transports in the CBP crystal. The molecular pairs of the geometrical types of A, B, and C, which are the most advantageous for both the hole and electron transports, are considered. As shown in Table 4, there are seven molecular pairs for the geometrical type of A. The pairs are illustrated in Fig. 6.8a. Through the pairs, both holes and electrons can be effectively transported in the b-c plane. In other words, effective percolation paths for charge transports are formed in the plane. For the geometrical type of B, four molecular pairs exist (see Table 6.4), which are presented in Fig. 6.8b. Through the periodic pairs of I(000)-I(1-11) and I(000)-I(-11-1), both holes and electrons are favorably transported along the $[1\bar{1}1]$ direction of the crystal. Also, they can be transported along the [111] direction by the periodic pairs of II(000)-II(111) and II(000)-I(-1-1-1). For the geometrical type of C, there are eight molecular pairs (see Table 6.4). The pairs are shown in Figs. 6.8c and 6.8d. The periodic pairs of I(000)-II(100) and I(000)-II(-1-1-1), or II(000)-I(111) and II(000)-I(-100) can transport both holes and electrons along the [122] direction of the crystal. In addition, charges can be effectively transported along the $[1\bar{2}2]$ direction through the periodic pairs of I(000)-II(1-10) and I(000)-II(-10-1), or II(000)-I(101) and II(000)-I(-110). From the above discussion, effective paths exist for both the hole and electron transports in CBP, confirming the

bipolar charge-transport property of CBP.

6.4 Conclusion

The charge-transport property of CBP was investigated, based on Marcus theory. By investigating both the reorganization energies and charge transfer integrals, the hole- and electron-transfer rate constants were calculated to be similar in magnitude. In addition, effective paths for both the hole and electron transports exist in the CBP crystal, showing the bipolar charge-transport property of CBP. Through the delocalized HOMO over the CBP molecule, holes are conveyed *via* all the segments of molecules. In contrast, electrons favorably transfer through the carbazole moieties. This is in sharp contrast with TPD; the LUMO is localized on the central biphenylene moiety, which results in small electron transfer integrals. The results clearly show the difference of the electron-transport property between CBP and TPD.

References

[1] C. W. Tang, S.A. VanSlyke, Appl. Phys. Lett. 51 (1987) 913.

[2] C. Adachi, S. Tokito, T. Tsutsui, S. Saito, Jpn. J. Appl. Phys. 27 (1988) L269.

[3] H. Kanai, S. Ichinosawa , Y. Sato, Synt. Met. 91 (1997) 195.

[4] B.E. Koene, D.E. Loy, M.E. Thompson, Chem. Mater. 10 (1998) 2235.

[5] C. Adachi, M.A. Baldo, S.R. Forrest, J. Appl. Phys. 87 (2000) 8049.

[6] C. Adachi, R. Kwong, S.R. Forrest, Org. Electron. 2 (2001) 37.

[7] N. Matsusue, Y. Suzuki, H. Naito, Jap. J. Appl. Phys. 44 (2005) 3691.

[8] H. Matsushima, S. Naka, H. Okada, H. Onnagawa, Curr. Appl. Phys. 5 (2005) 305.

[9] Y. Wang, Y. Hua, X. Wu, L. Zhang, Q. Hou, F. Guan, N. Zhang, S. Yin, X. Cheng, Org. Electron. 9 (2008) 692.

[10] Y. Tao, Q. Wang, L. Ao, C. Zhong, J. Qin, C. Yang, D. Ma, J. Mater. Chem. 20 (2010) 1759.

[11] M. Stolka, J.F. Yanus, D.M. Pai, J. Phys. Chem. 88 (1984) 4707.

[12] J. Kido, M. Kimura, K. Nagai, Science 267 (1995) 1332.

[13] V. Bulović, G. Gu, P.E. Burrows, S.R. Forrest, M.E. Thompson, Nature 380 (1996) 29.

[14] H. Mattoussi, H. Murata, C.D. Merritt, Y. Iizumi, J. Kido, Z.H. Kafafi, J. Appl. Phys. 86 (1999) 2642.

[15] A. Kuwahara, S. Naka, H. Okada, H. Onnagawa, Appl. Phys. Lett. 89 (2006) 132106.

[16] P. Cusumano, S. Gambino, J. Electron. Mater. 37 (2008) 231.

[17] R.A. Marcus, J. Chem. Phys. 24 (1956) 966.

[18] R.A. Marcus, N. Sutin, Biochim. Biophys. Acta 811 (1985) 265.

[19] T. Yamada, T. Sato, K. Tanaka, H. Kaji, Org. Electron. 11 (2010) 255.

[20] A.D. Becke, Phys. Rev. A 38 (1988) 3098.

[21] A.D. Becke, J. Chem. Phys. 98 (1993) 5648.

[22] C.T. Lee, W.T. Yang, R.G. Parr, Phys. Rev. B 37 (1988) 785.

[23] P.J. Low, M.A.J. Paterson, D.S. Yufit, J.A.K. Howard, J.C. Cherryman, D.R. Tackley, R. Brook, B. Brown, J. Mater. Chem. 15 (2005) 2304.

[24] P.O. Löwdin, J. Chem. Phys. 18 (1950) 365.

[25] V. Coropceanu, J. Cornil, D.A. da Silva Filo, Y. Olivier, R. Silbey, J.L. Brédas, Chem. Rev. 107 (2007) 926.

[26] M.J. Frisch et al., Gaussian 03, Revision E.01, Gaussian, Inc., Wallingford CT, 2004.

[27] A.R. Kennedy, W.E. Smith, D.R. Tackley, W.I.F. David, K. Shankland, B. Brown, S.J. Teat, J. Mater. Chem. 12 (2002) 168.

[28] Z. Zhang, E. Burkholder, J. Zubieta, Acta Cryst. C60 (2004) o452.

[29] M. Wolfsberg, L. Helmholz, J. Chem. Phys. 20 (1952) 837.

[30] R. Hoffmann, J. Chem. Phys. 39 (1963) 1397.

Summary

This thesis described the molecular and electronic structures and charge-transport properties of materials for organic light-emitting diodes (OLEDs), *N,N'*-diphenyl-*N,N'*-di(*m*-tolyl)benzidine (TPD) and 4,4'-*N,N'*-dicarbazolylbiphenyl (CBP). The results and findings in the respective chapters are summarized as follows.

In Chapter 2, the amorphous structure of TPD was analyzed by the combined use of solid-state ^{15}N NMR and quantum chemical calculations. The ^{15}N chemical shift anisotropy (CSA) spectrum of amorphous TPD was obtained, showing that the spectrum is as narrow as ~15 ppm. In addition, density functional theory (DFT) calculations were performed to find that the ^{15}N CSA of TPD strongly depends on the planarity and the torsion angles around the nitrogen atom, which are of particular interest for the structure. Because the experimental ^{15}N CSA is in good agreement with the calculated CSA for the DFT-optimized TPD molecule, the DFT-optimized structure of a single TPD molecule should reflect the structure in the condensed amorphous state; the nitrogen and tree carbons atoms directly bonded to the nitrogen atom are in the same plane (the plane is referred to as "TPA plane"), and the three rings attached to the nitrogen adopt a propeller-shape conformation with the torsion angles of ~40^{o}. Compared with other amine compounds such as aniline, the planarity around the nitrogen atom of TPD is discriminative. The planar structure was suggested to be more favorable for hole transports than the pyramidal structure, because the sp^2 hybridized nitrogen atom and the shorter intermolecular distance for the planar structure are advantageous for the intermolecular overlaps of HOMOs. It was also suggested that the stable conformers as many as 40 exist for amorphous TPD. These structures have inconsistency between the previous XRD results. The inconsistency would originate due to the crystalline packing effect. The validity of the

combined use of solid-state NMR experiments and quantum chemical calculations for the analysis of the amorphous structure was successfully shown.

In Chapter 3, the ^{15}N NMR shieldings of TPD were investigated in detail, considering the relationships with the electronic structure and the charge-transport property. The origins of the conformational dependences of ^{15}N CSA obtained in Chapter 2 were analyzed, dividing the shielding values into the diamagnetic shielding and paramagnetic deshielding terms. It was revealed that the conformational dependence of ^{15}N CSA is dominated by the paramagnetic deshielding term. The natural chemical shielding (NCS) analyses indicated that the lone pair orbital of the nitrogen and the σ orbitals of the N-C bonds largely contribute to the conformational dependence of the paramagnetic deshieldings. According to Ramsey's theory, this originates from the conformational dependence are the n–π interaction between the nitrogen and the directly bonded benzene rings and the σ–σ^* interaction between the three N-C bonds around the nitrogen. The result indicates that the electronic structure around the nitrogen, which has large contribution to HOMO, has a conformational dependence. It was found that the distribution of HOMO is largely changed depending on the conformation; HOMO is localized on the nitrogen and benzene rings which strongly interact with the nitrogen p_z orbital. For the DFT-optimized conformation, the HOMO is relatively delocalized over the molecule. The advantageous of the delocalization for hole transports was shown in Chapters 5 and 6. In contrast, LUMO of TPD is almost localized on the central biphenylene segment irrespective of the conformation, which is unfavorable for electron transports.

In Chapter 4, the charged states of TPD were investigated. The monocationic and dicationic states of TPD were produced by chemical oxidations and analyzed by solid-state ^{15}N NMR experiments. It was found from CP/MAS experiments that the isotropic ^{15}N chemical shifts of TPD in the neutral and dicationic states are significantly different from each other. The

observed spectra for neutral and dicationic TPD are consistent with the results of DFT calculations. The appearance of only one resonance line for the dicationic sample as well as the neutral sample indicates that the two ^{15}N nuclei are principally in the same state. For the monocationic TPD sample, no ^{15}N resonance lines were observed, suggesting the strong interaction between the unpaired (radical) electron spin and the ^{15}N nuclei spin. This also suggests that the two ^{15}N nuclei of the monocationic sample are in the same state, due to the electronic interaction between the nuclei. The existence of unpaired electron was confirmed by an ESR experiment for monocationic TPD, while no signals were obtained for neutral and dicationc TPD. These results show that the charged states can be monitored by solid-state NMR with the help of ESR; they have a potential for direct observations of charge transports phenomena in the devices. In addition, it was found from the CSA measurements that solid-state NMR can offer information on the orbitals from which the electrons are extracted. For TPD, the electrons are extracted from the nitrogen p_z orbital which is perpendicular to the TPA plane, leading to the drastic changes of σ_{xx} and σ_{yy} values while the σ_{zz} value is almost constant. The result experimentally shows that the nitrogen p_z orbital corresponds to the HOMO and are essential for hole transports.

In Chapter 5, both the reorganization energies and charge transfer integrals were investigated for TPD to quantify the charge-transfer rate constants, based on Marcus theory. The reorganization energies were calculated from the optimized geometry. The calculations of charge transfer integrals were carried out by extended Hückel method for all the neighboring pairs of two molecules in the crystals, analyzing all of the Coulomb, resonance, and overlap integrals between the frontier orbitals. The obtained maximum hole- and electron-transfer rate constants were in the order of 10^{12} and 10^{10} s^{-1}, respectively. It was found that not only the small reorganization energy but also the large charge transfer integrals for hole transfers are the

origins of the better hole-transport property of TPD, compared with the electron-transport property. From the detailed analysis, it was revealed that the charge transfers among the outside tolyl and phenyl rings of TPD are dominant for hole transfers. Because the HOMO of TPD are delocalized over the molecule and the tolyl and phenyl rings have close intermolecular contacts in the crystals, large intermolecular overlaps of HOMO can be formed among the rings. On the other hand, the LUMO of TPD is localized on the central biphenylene moiety, resulting in the smaller intermolecular overlaps. In addition, percolated hole-transport paths were found in the condensed state. The paths consisting of consecutive molecular pairs with large values of hole-transfer rate constants, 10^{12} s^{-1}, are formed in the TPD crystals. This can explain the good hole-transport property of TPD, experimentally observed by, for example, time-of-flight experiments.

In Chapter 6, the charge-transfer rate constants for 4,4'-*N*,*N'*-dicarbazolylbiphenyl (CBP), a well-known bipolar charge-transport material for OLEDs, were quantified by extended Hückel method as in the case of TPD in Chapter 5. The hole- and electron-transfer rate constants were calculated to be in the same order, owing to that both the reorganization energy and charge transfer integrals are comparable for hole and electron transfers. Also, percolated charge-transport paths were found for both the hole and electron transports. This is in sharp contrast with the case of a structurally similar but a poor electron-transport material, TPD, for which the electron-transfer rate constants were calculated to be two orders of magnitude smaller than the hole-transfer rate constants. From the detailed analysis of the charge transfer integrals for CBP, it was found that holes transfer through all the segments of the molecules, using the delocalized HOMO over the whole molecule. This picture is similar to the hole transports of TPD. For electron transports, electrons transfer advantageously through the delocalized LUMO on the carbazole moieties of CBP, which have close intermolecular contacts. In

contrast, the LUMO of TPD localizes on the central biphenylene moiety, resulting in small electron transfer integrals. The results clearly show the difference of the electron-transport property between CBP and TPD. It was suggested that not only the reorganization energy but also the delocalization of frontier orbitals and close intermolecular contacts are essential factors for the intermolecular charge transfers, and thus for the charge-transport property of these triphenylamine-related materials. The findings are helpful for designs of molecules with better charge-transport performances.

List of Publications

Chapter 2

"A combined experimental and theoretical study of the conformation of *N,N'*-diphenyl-*N,N'*-di(*m*-tolyl)benzidine using solid-state ^{15}N NMR and DFT calculations"

H. Kaji, T. Yamada, N. Tsukamoto, F. Horii

Chemical Physics Letters 401 (2005) 246-253.

"Planarity of triphenylamine moieties of a typical hole-transport material for OLEDs, *N,N'*-diphenyl-*N,N'*-di(*m*-tolyl)benzidine (TPD), in the amorphous state"

T. Yamada, H. Kaji

Journal of Molecular Structure 927 (2009) 82-87.

Chapter 3

"Conformational dependence of the diamagnetic and paramagnetic ^{15}N NMR shifts and charge-transport property of *N,N'*-diphenyl-*N,N'*-di(*m*-tolyl)benzidine"

T. Yamada, H. Kaji

In preparation.

Chapter 4

"Electronic states of the hole transport material, *N,N'*-diphenyl-*N,N'*-di(*m*-tolyl)benzidine (TPD), and its dicationic state studied by ^{15}N NMR and DFT calculations"

H. Kaji, T. Yamada, N. Tsukamoto, Y. Kusaka

Applied Physics Letters, to be submitted.

Chapter 5

"Percolation paths for charge transports in *N*,*N'*-diphenyl-*N*,*N'*-di(*m*-tolyl)benzidine (TPD)"

T. Yamada, T. Sato, K. Tanaka, H. Kaji

Organic Electronics 11 (2010) 255-265.

Chapter 6

"Revealing bipolar charge-transport property of 4,4'-*N*,*N'*-dicarbazolylbiphenyl (CBP) by quantum chemical calculations"

T. Yamada, F. Suzuki, A. Goto, T. Sato, K. Tanaka, H. Kaji

Organic Electronics 12 (2011) 169-178.

Other Publications

"Geometric and electronic structures of a hole-transport material, TPD, and related materials studied by DFT calculations and solid-state NMR"

H. Kaji, T. Yamada

Proceedings of SPIE 7051 (2008) [705104-1]-[705104-7].

"Local stoichiometry in amorphous supramolecular composites analyzed by solid-state ^{13}C NMR"

H. Kaji, H. Hayashi, T. Yamada, M. Fukuchi, S. Fujimura, M. Ueda, S. Kang, T. Umeyama, Y. Matano, H. Imahori

Applied Physics Letters 98 (2011) [113301-1]-[113301-3].

Acknowledgement

The studies presented in this thesis were carried out under the direction of Professor Hironori Kaji at Institute for Chemical Research, Kyoto University. The author would like to express his gratitude to Professor Hironori Kaji for his invaluable suggestion and kind guidance throughout the study.

The author is sincerely grateful to Professor Emeritus Fumitaka Horii, Associate Professor Atsushi Goto, and Dr. Asako Hirai, Institute for Chemical Research, Kyoto University, for their helpful suggestions during this study.

Sincere appreciation is due to Professor Kazuyoshi Tanaka and Associate Professor Tohru Sato, Department of Molecular Engineering, Graduate School of Engineering, Kyoto University, for their active collaborations in this study.

The author acknowledges to his colleagues, Mr. Yasunari Kusaka, Mr. Naoki Tsukamoto, and Mr. Furitsu Suzuki, for their useful discussion and encouragement.

Thanks are also given to other staffs and students in Institute for Chemical Research, Kyoto University, for their kindness during this study.

Finally, the author heartily wishes to express his thanks to his parents, Noriharu Yamada, Mariko Yamada, and all his relatives.

Tomonori Yamada